JOINT TRANSPORTATION
RESEARCH PROGRAM
INDIANA DEPARTMENT OF TRANSPORTATION
AND PURDUE UNIVERSITY

Investigation of Durability and Performance of High Friction Surface Treatment

Fulu Wei, Ce Wang, Xiangxi Tian,
Shuo Li, Jie Shan

SPR-4300 • Report Number: FHWA/IN/JTRP-2021/02 • DOI: 10.5703/1288284317281

RECOMMENDED CITATION

Wei, F., Wang, C., Tian, X., Li, S., & Shan, J. (2021). *Investigation of durability and performance of high friction surface treatment* (Joint Transportation Research Program Publication No. FHWA/IN/JTRP-2021/02). West Lafayette, IN: Purdue University. https://doi.org/10.5703/1288284317281

AUTHORS

Fulu Wei
Ce Wang
Xiangxi Tian
Graduate Research Assistants
Lyles School of Civil Engineering
Purdue University

Shuo Li, PhD, PE
Research Engineer
Division of Research and Development
Indiana Department of Transportation,
(765) 463-1521 ×247
SLI@indot.IN.gov
Corresponding Author

Jie Shan, PhD
Professor of Civil Engineering and Affiliate of Environmental and Ecological Engineering
Lyles School of Civil Engineering
Purdue University
Principle Investigator

ACKNOWLEDGMENTS

This research project was sponsored by the Indiana Department of Transportation (INDOT) in cooperation with the Federal Highway Administration (FHWA) through the Joint Transportation Research Program (JTRP). The authors would like to thank the study advisory committee (SAC) members, Mike Holowaty, Tim Wells, Prakash Patel, Joe Bruno, Mike Nelson, Laura Slusher, Rick Drumm, and Brent Wendholy for their guidance. Sincere thanks are extended to Ayesha Shah, Mingliang Xing, Bowen Guan, Hua Zhao, Yong Xu, and Oguz Gungor of Purdue University, and Dwayne Harris, Tony Johnson, Mike Moredock, Brent Richter, and Brenda Harrison of INDOT, for their help with laboratory and field tests. The authors recognize the assistance provided by Dan Patacca of E-Chem, LLC, Todd Richard of American Structurepoint, Inc., and Ryan Merchant of RAM Construction Services of Michigan.

JOINT TRANSPORTATION RESEARCH PROGRAM

The Joint Transportation Research Program serves as a vehicle for INDOT collaboration with higher education institutions and industry in Indiana to facilitate innovation that results in continuous improvement in the planning, design, construction, operation, management and economic efficiency of the Indiana transportation infrastructure. https://engineering.purdue.edu/JTRP/index_html

Published reports of the Joint Transportation Research Program are available at http://docs.lib.purdue.edu/jtrp/.

NOTICE

TECHNICAL REPORT DOCUMENTATION PAGE

1. Report No.	2. Government Accession No.	3. Recipient's Catalog No.
FHWA/IN/JTRP-2021/02		

4. Title and Subtitle	5. Report Date
Investigation of Durability and Performance of High Friction Surface Treatment	December 2020
	6. Performing Organization Code

7. Author(s)	8. Performing Organization Report No.
Fulu Wei, Ce Wang, Xiangxi Tian, Shuo Li, and Jie Shan	FHWA/IN/JTRP-2021/02

9. Performing Organization Name and Address	10. Work Unit No.
Joint Transportation Research Program (SPR) Hall for Discovery and Learning Research (DLR), Suite 204 207 S. Martin Jischke Drive West Lafayette, IN 47907	11. Contract or Grant No. SPR-4300

12. Sponsoring Agency Name and Address	13. Type of Report and Period Covered
Indiana Department of Transportation State Office Building 100 North Senate Avenue Indianapolis, IN 46204	Final Report
	14. Sponsoring Agency Code

15. Supplementary Notes

Conducted in cooperation with the U.S. Department of Transportation, Federal Highway Administration.

The Indiana Department of Transportation (INDOT) completed a total of 25 high friction surface treatment (HFST) projects across the state in 2018. This research study attempted to investigate the durability and performance of HFST in terms of its HFST-pavement system integrity and surface friction performance. Laboratory tests were conducted to determine the physical and mechanical properties of epoxy-bauxite mortar. Field inspections were carried out to identify site conditions and common early HFST distresses. Cyclic loading test and finite element method (FEM) analysis were performed to evaluate the bonding strength between HFST and existing pavement, in particular chip seal with different pretreatments such as vacuum sweeping, shotblasting, and scarification milling. Both surface friction and texture tests were undertaken periodically (generally once every 6 months) to evaluate the surface friction performance of HFST. Crash records over a 5-year period, i.e., 3 years before installation and around 16 months after installation, were examined to determine the safety performance of HFST, crash modification factor (CMF) in particular.

It was found that HFST epoxy-bauxite mortar has a coefficient of thermal expansion (CTE) significantly higher than those of hot mix asphalt (HMA) mixtures and Portland cement concrete (PCC), and good cracking resistance. The most common early HFST distresses in Indiana are reflective cracking, surface wrinkling, aggregate loss, and delamination. Vacuum sweeping is the optimal method for pretreating existing pavements, chip seal in particular. Chip seal in good condition is structurally capable of providing a sound base for HFST. On two-lane highway curves, HFST is capable of reducing the total vehicle crash by 30%, injury crash by 50%, and wet weather crash by 44%, and providing a CMF of 0.70 in Indiana. Great variability may arise in the results of friction tests on horizontal curves by the use of locked wheel skid tester (LWST) due both to the nature of vehicle dynamics and to the operation of test vehicle. Texture testing, however, is capable of providing continuous texture measurements that can be used to calculate a texture height parameter, i.e., mean profile depth (MPD), not only for evaluating friction performance but also implementing quality control (QC) and quality assurance (QA) plans for HFST.

17. Key Words	18. Distribution Statement
high friction surface friction, durability, friction number, surface texture, mean profile depth, epoxy-bauxite mortar, surface pretreatment, chip seal, vacuum sweeping, shotblasting, scarification milling, early distress, bonding, reflective cracking, crash modification factor	No restrictions. This document is available through the National Technical Information Service, Springfield, VA 22161.

19. Security Classif. (of this report)	20. Security Classif. (of this page)	21. No. of Pages	22. Price
Unclassified	Unclassified	66 including appendices	

EXECUTIVE SUMMARY

Introduction

High friction surface treatment (HFST) is increasingly being used to reduce vehicle crashes at friction-sensitive locations, such as sharp horizontal curves, intersection approaches, bridge decks, interstate ramps, long and steep grades, and tunnel entrances. Nevertheless, several major issues have remained unsolved.

- First, the epoxy-resin binder for HFST is commonly produced in accordance with the requirements for applications to Portland-cement concrete (PCC). Concerns may arise about its applications to hot-mix asphalt (HMA) that affects not only the reflective distresses in HFST but also the bonding at the HFST-HMA interface.
- Second, the friction performance of HFST relies on its surface characteristics. An efficient method is needed to timely determine catastrophic drop in HFST's surface friction due to immediate and excessive loss of aggregate.
- Third, the Indiana Department of Transportation (INDOT) conducts the locked wheel skid tester (LWST) friction testing using the standard smooth tire. However, the friction requirement in the current unique special provision (USP) for HFST by INDOT was defined in terms of the standard rib tire.
- Lastly, determining the cost-effectiveness or crash modification factor (CMF) of HFST requires field friction and vehicle crash data. Although there are a few CMFs for HFST reported by other states, a state-specific CMF would allow INDOT to address the state's specific features and utilize safety dollars more efficiently.

These concerns led to the creation of Joint Transportation Research Program (JTRP) Project SPR-4300, *Investigation of Durability and Performance of High Friction Surface Treatment*. This project attempted primarily to investigate the durability and performance of HFST in terms of its system integrity and surface friction. The other objectives included (1) determining the physical and mechanical properties of HFST epoxy-bauxite mortar; (2) investigating the mechanical behaviors of interaction between HFST and the underlying pavement (in particular chip seal); (3) examining the variation of surface friction characteristics of HFST over time; and (4) quantifying the cost-effectiveness and CMF for HFST initiative projects.

This project performed a comprehensive investigation of the above-mentioned issues based on a total of 25 HFST projects completed in 2018. The projects included 21 projects in an HFST initiative program to address vehicle crash issues on horizontal curves across the state and 4 projects in a pavement resurfacing program. The main tasks completed by the research team included (1) extensive laboratory tests for determining the physical and mechanical properties of HFST epoxy-bauxite mortar; (2) field inspections for identifying early HFST distresses and their mechanisms; (3) laboratory cyclic loading tests and finite element method (FEM) analysis for evaluating the interface bonding and pretreatment for the existing pavement; (4) field friction and texture tests for determining the friction metrics; and (5) analysis of crash data for identifying HFST's safety effectiveness, especially CMF. In addition, this project also investigated the use of image processing technologies for measuring HFST surface texture efficiently and cost-effectively from multi-view images collected by smartphones.

Findings

Key findings are summarized as follows:

- *HFST epoxy-bauxite mortar properties.* An epoxy binder content of approximately 15.9% may be appropriate for making specimens for determining the physical and mechanical properties of the HFST epoxy-bauxite mortar. HFST epoxy-bauxite mortar has a bulk specific gravity of 2.31, a Poisson's ratio of 0.29, and a coefficient of thermal expansion (CTE) of 21.3 $\times$ 10^{-6}/°F (37.72 $\times$ 10^{-6}/°C). The CTE of HFST is significantly higher than those of HMA and PCC, which implies that thermal incompatibilities will arise between HFST and the underlying HMA or PCC pavement.
- *Most common early distresses in HFST.* The most common early HFST's distresses in Indiana are reflective cracking, aggregate loss, delamination at the interface of chip seal-HMA pavement beneath HFST, and surface wrinkling (slippage). Any discontinuities in the existing pavement surface, including cracks, pothole patches, and alligator repair patches, will reflect through HFST. The above may be extended to imply that there are tangible benefits to placing HFST on new pavements. Aggregate loss is likely to occur in an HFST when the existing pavement is pretreated by scarification milling due to insufficient epoxy binder, when the HFST is installed at low temperatures, or both. Delamination at the chip seal-HMA interface tends to occur when the chip seal surface is pretreated by scarification milling. Surface wrinkling tends to occur due to the combined effect of large traffic loads, low temperature installation, and steep superelevation.
- *Existing pavement surface preparation and effects.* The MPD of HFST is independent of the methods for pretreating the existing pavement. Scarification milling and shotblasting do not necessarily increase the MPD of HFST surface. Scarification milling produces large valleys and peaks in the treated surface, which will result in a large region of stress concentration and will dramatically raise interlaminar stresses. The bonding strength with scarification milling can be 18.6% lower than that with shotblasting in the tire-pavement contact area. The impact of traffic loading on the bonding strength can be more severe with scarification milling than with shotblasting. The results of finite element method (FEM) analysis show that shotblasting tends to increase the possibilities of higher interlaminar stresses than vacuum sweeping. No conclusive evidence exists to show that vacuum sweeping, shotblasting, or scarification milling can outperform any of the others in terms of the mitigation of reflective cracking.
- *Determination of crash modification factor (CMF) for HFST.* The CMF of HFST (i.e., 0.701) calculated from before-and-after crash data is very close to the CMF (i.e., 0.696) derived from the crash prediction model that was developed in terms of curve geometrics, pavement friction, and AADT. The zero-inflated negative binomial model developed for vehicle crashes on curves is explanatory for horizontal curve safety performance and can be used to estimate the effects of pavement friction, curve radius, or both on safety performance. Most importantly, this model can be used to identify highly risky curves and facilitate safety engineers to implement countermeasures efficiently.
- *HFST friction metrics and field testing.* Great variability may arise in the results of friction tests on horizontal curves measured by the use of the LWST method—due both to the

nature of vehicle dynamics and to the operation of test vehicle on sharp horizontal curves. Texture testing, however, is capable of providing continuous texture measurements that can be used to calculate a texture height parameter, i.e., mean profile depth (MPD), not only for evaluating friction performance but also for implementing quality control (QC) and quality assurance (QA) plans for HFST.

Implementation

The test results and research findings can be implemented as follows to enhance the durability and safety effectiveness of HFST in terms of the appropriate preparation of existing pavement, data-driven material application, improved specifications, and effective candidate project selection.

- *Installation temperature.* The epoxy-bauxite mortar of HFST is a viscoelastic material at a temperature of 70°F or higher. Curing epoxy binders at low temperatures will not only increase the cost for traffic control but also the variation in the property of the epoxy binder system, thereby affecting the durability of HFST. It is recommended to install HFST at the higher end of the temperature range recommended by suppliers.
- *HFST epoxy-bauxite mortar specimen.* The empirical relationship below can be utilized to estimate the binder content for fabricating epoxy-bauxite mortar specimens:

$$R = R_0 + (1.755 + 0.090MPD)$$

where R is the approximated content of epoxy binder, percent by mass; R0 is the supplier's recommended binder application rate, percent by mass; and MPD is the mean profile depth of HFST.

- *Existing pavement surface preparation.* The cracks in the existing pavement should be filled prior to the installation of HFST rather than by the epoxy binder spread on the existing pavement during application. Cracks reflected through the HFST should be sealed timely to slow the deterioration of cracks. Chip seal in good condition will not affect the durability of HFST in terms of interface bonding strength. Scarification milling does not necessarily provide better interface bonding between HFST and the underlying chip seal. Vacuum sweeping and shotblasting, respectively, are recommended as an effective method for preparing the surface of chip seal and the new HMA pavement.
- *Friction performance and testing.* To ensure the durability of HFST, either friction or texture testing should be performed 3 months after installation. In addition, field testing right after installation may identify potential problems when corrective actions can still be taken. The following requirements for HFST QC and QA can be defined in terms of surface friction, texture, or both.

Time	Friction Number (FN)	Mean Profile Depth (MPD) (mm)
New	83	1.9
3 Months	83	1.2

The above requirements are also recommended to revise INDOT's current USP for HFST.

- *CMF determination.* A CMF of 0.70 is recommended for use in estimating the safety effectiveness of HFST by INDOT.
- *After-installation crash analysis.* Further analysis will be performed when more after-installation crash data is available. However, caution should be given to the 2020 crash data due to the impact of COVID-19 on traffic. In addition, the following model can be used to identify high risk curves and facilitate traffic safety engineers to implement countermeasures efficiently.

$$N = \left(1 - \frac{e^{-8.83} rad^{0.29} AADT^{2.10}}{1 + e^{-8.83} rad^{0.29} AADT^{2.10}}\right) e^{-0.46} rad^{-0.22} L^{0.45} FN^{-0.46} AADT^{0.62}$$

where N is the annual crash number at a specific curve; *rad* and L, respectively, are the radius and length of the curve, ft.; FN is the friction number at 40 miles per hour (mph); and $AADT$ is the Annual Average Daily Traffic.

CONTENTS

LIST OF TABLES

LIST OF FIGURES

1. INTRODUCTION

1.1 Background

High friction surface treatment (HFST) has been proactively promoted by Federal Highway Administration (FHWA) as a cost-effective solution to pavement friction related vehicle crashes, including run-off-road, tailgating, and head-on crashes, particularly on two-lane roads or at intersections and under wet pavement conditions. To further improve traffic safety, the Indiana Department of Transportation (INDOT) launched an initiative to carry out HFST projects with a total value of more than $1 million statewide in 2018. Prior to the above HFST initiative, a Joint Transportation Research Program (JTRP) research study, SPR-3882, had been completed to provide original data for INDOT engineers to better understand HFST and develop or revise specifications relevant to HFST (Li et al., 2017). Through this effort, comprehensive laboratory tests were conducted to evaluate the properties of HFST calcined bauxite aggregate and alternative aggregate (i.e., steel slag). Laboratory accelerating polishing was carried out to identify promising HFST systems. Test strips were installed in an actual pavement to further evaluate the friction performance and durability of the identified promising HFST systems under the polishing by real traffic and the effect of winter and snowplows over a time period of 9 months.

Nevertheless, several major issues have remained unsolved. First, while test strips were polished by real traffic for a time period of 9 months, the results might not fully reveal all subtle aspects of HFST, simply due to the small size of test strips (i.e., 15″ wide × 40″ long) and the short time duration of traffic polishing. Therefore, the results could lead to immature specifications for the construction of HFST. Second, the epoxy-resin binder currently used for HFST is widely produced in accordance with ASTM C881 that defines epoxy-resin binders for application to Portland-cement concrete (ASTM, 2015a). Concerns have always been raised about its compatibility with hot-mix asphalt (HMA) pavement, which affects not only the reflective distresses in HFST, but also the bonding at the interface between HFST and HMA pavement. The compatibility plays an important role in ensuring the durability of HFST.

Third, the friction performance of HFST relies on its surface frictional characteristics, including macro-texture and micro-texture. The former provides drainage channels and varies with aggregate geometrics (size and shape), gradation, and mix volumetric properties, while the latter is of critical importance for long-term friction performance and depends primarily on the mechanical properties and surface characteristics of the aggregate. In addition, catastrophic drop in HFST surface friction may occur due to immediate and excessive loss of aggregate. Fourth, the friction requirement in the INDOT's current unique special provision (USP) for HFST was developed in terms of the standard rib tire. Nevertheless, the INDOT's friction test program utilizes the standard smooth tire in field friction testing and field friction data is needed to revise the current friction requirement for HFST. Lastly, determining the cost-effectiveness or crash modification factor (CMF) of HFST requires field friction and actual vehicle crash data. Although there are currently a few CMFs for HFST reported by other states (Atkinson et al., 2016; FHWA, n.d.; de León Izeppi, 2010; Merritt et al., 2015), a state-specific CMF would allow INDOT to address the state's specific features and utilize safety dollars more efficiently.

1.2 Research Objectives

The primary objective of this study was to investigate the durability and performance of HFST in terms of the structural integrity and surface friction. The four sub-objectives were (1) to determine the physical and mechanical properties of HFST epoxy-bauxite mortar; (2) to investigate the mechanical behaviors of interaction between HFST and the underlying pavement; (3) to determine the variation of surface friction characteristics of HFST over time; and (4) to quantify the cost-effectiveness and CMF for HFST initiative projects. It was anticipated that the results and findings would be used to revise the INDOT's current USP for HFST and harmonize the specifications for epoxy binders used in HFST and polymeric thin bridge deck overlay.

1.3 Research Approach and Tasks

An integrated approach was utilized to combine the mechanistic analysis, laboratory and field tests, and field inspection to accomplish the research tasks defined to fulfill the research objectives. In addition to literature review, the main research tasks completed are summarized as follows:

1. *Roadway assessment.* This task included field inspection to identify the existing roadway geometric and pavement conditions and field tests to measure the surface frictional and structural properties. Field inspection focused on surface distresses, including cracking and patching, and drainage and moisture condition. Field tests consisted of surface friction test, surface texture test, falling weight deflectometer test, and ground penetration radar (GPR) test that was defined to provide inputs for mechanistic analysis.
2. *HFST durability*. The durability of HFST was investigated in terms of the integrity and friction performance of HFST, depending on aggregate loss, reflective defect, debonding, and effect of snowplow. Both friction and texture tests were conducted to estimate the amount and progression of aggregate loss. Visual inspections were carried out before and after construction to assess surface defects, especially reflective cracking. Field pavement cores were taken to evaluate the bonding strength at the interface.
3. *Thermal and mechanical behaviors.* A first-of-its-kind effort was made to evaluate the thermal and mechanical behaviors of HFST systems based on the site-specific conditions such as existing pavement structural capacity, traffic, and temperature variation. Comprehensive laboratory tests were first conducted to determine the

physical and mechanical properties of the epoxy-bauxite mortar of HFST, including specific gravity, Poisson's ratio, coefficient of thermal expansion (CTE), dynamic modulus, and crack resistance. Finite element analysis (FEA) was then performed to model the mechanical behaviors of HFST in terms of interface bonding and crack development to capture the possible effects of the pre-treatment of existing pavement surface. Finally, both laboratory and field tests and inspections were undertaken to validate the FEA results.

4. *HFST friction performance.* Surface friction and texture tests were conducted multiple times for all HFST initiative projects with conventional test methods during the study period. An attempt was also made to measure textures by using smartphone image processing techniques. Both the friction and texture measurements were utilized to evaluate the long-term friction performance of HFST and would be used to revise the INDOT's current USP for HFST.
5. *CMF development*. Vehicle crash data for the period of 2015–2020 at the HFST initiative project sites were utilized to examine the crash characteristics before and after installing HFST. The empirical Bayes methodology was employed to estimate the number of crashes after placing HFST and generate the corresponding CMF. In addition, a binomial model was introduced to predict the crash frequency at horizontal curves in terms of some critical influencing factors, such as curve radius and length, pavement friction, and Annual Average Daily Traffic (AADT).

2. DETERMINATION OF PROPERTIES OF EPOXY-BAUXITE MORTAR OF HIGH FRICTION SURFACE TREATMENT

2.1 Mix Design

2.1.1 Materials

The epoxy resin binder used in INDOT's HFST initiative projects was a two-component epoxy resin binder system for both mechanical and manual applications, and was claimed as a low-modulus, moisture tolerant, and high strength adhesive. The mix ratio of the two components was 1:1 by volume. The mixing temperature recommended by the supplier ranges between 60°F and 95°F. The cure time varies from 2.5 hours to 6 hours, depending on the temperature. Presented in Table 2.1 are the test results for the physical properties of the selected epoxy resin binder from the supplier and the AASHTO (2014a) requirements for HFST epoxy-resin binders. Notice that the current AASHTO requirement for the compressive strength is measured in accordance with ASTM C579, *Standard Test Methods for Compressive Strength of Chemical-Resistant Mortars, Grouts, Monolithic Surfacings, and Polymer Concretes* (ASTM, 2018a), instead of ASTM D695, *Standard test method for compressive properties of rigid plastics* (ASTM, 2015b). The former is designated for chemical-resistant mortars, grouts, monolithic surfacings, and polymer concretes, and the latter is designated for rigid plastics. Also, the test specimens

TABLE 2.1
Properties of the epoxy resin binder

Property	Test Result	AASHTO Requirement
Viscosity	14.2 poise	7–30 poises
Gel time	19 minutes	10 minutes min
Ultimate tensile strength	2.89 ksi	2.5–5.0 ksi
Elongation at break	50.9%	30%–70%
Durometer hardness	65	60–80
Compressive strength (3 h)	6.63 ksi	1.0 ksi min
Adhesive strength (24 h)	0.78 ksi	0.25 ksi min
Water absorption (24 h)	0.11%	1%

are commonly right cylinders of 1″ in diameter by 1″ in height in ASTM C579 and ½″ in diameter by 1″ high in ASTM D695.

Table 2.2 presents the test results of the calcined bauxite aggregate from the supplier and the corresponding property requirements established by AASHTO (2014a). Caution should be exercised when determining the polishing resistance of aggregate. The polishing resistance of aggregate may be measured using the so-called polished stone value (PSV) in accordance with BS EN 1097, *Tests for Mechanical And Physical Properties of Aggregates: Determination of the Polished Stone Value* (BSI, 2009), widely recognized by European countries or PV-10 in accordance with AASHTO T279, *Standard Method of Test for Accelerated Polishing of Aggregates Using the British Wheel* (AASHTO, 2014b), accepted by State DOTs in the US. It was concluded that, however, no unique correlation exists between PSV and PV-10 and no evidence has been reported to suggest which one is more accurate for measuring polishing resistance (Yu et al., 2019). PSV or PV-10 varies with the size of aggregate used for testing. In general, PSV or PV-10 increases as aggregate size increases.

2.2 Determination of Binder Content

2.2.1 Approximation of Binder Content

Experimental work was conducted to determine an appropriate epoxy binder content for the epoxy-bauxite mortars of HFST. Three HFST square specimens were first made using 2.4″ × 2.4″ tiles. As a general rule of thumb, the epoxy binder and calcined bauxite aggregate should be applied in accordance with the supplier's recommended application rates, i.e., 1 gallon per 26–32 square feet for the binder and 14–20 lbs. per square yard for the aggregate in this case. In reality, the maximum application rate of 1.31 L/square yard was utilized for these specimens, considering that the content of epoxy binder for making epoxy-bauxite mortar specimens for property tests would be higher than that for the epoxy-bauxite mortars in actual HFST projects. After the HFST was fully cured, the loose aggregate particles were removed and the weights of the binder and seated aggregate particles were measured for each

TABLE 2.2
Properties of the calcined bauxite aggregate

Property	Result	AASHTO Requirement
Al_2O_3	88.10%	87% min
LAA loss	9.3%	20% max
PSV	71.0	–
Moisture	0.3	0.2% max
Aggregate Grading	**Mass % Passing**	
No. 4 (4.75 mm)	–	100%
No. 6 (3.35 mm)	95%–100%	95%
No. 16 (1.18 mm)	0%–5%	5%

specimen as shown in Table 2.3. The percentage of epoxy binder by mass for the HFST square specimens ranged between 14.01% and 15.25% with an average of 14.56%. As shown in Figure 2.1 is an HFST square specimen. Its surface consists of many irregular voids. This may imply that a higher epoxy binder content should be used to provide sufficient bonding between aggregates when making epoxy-bauxite mortars due to the voids. Notice that the mean profile depth (MPD) (ASTM, 2015c) was utilized by the authors to measure the average depth of the surface voids in this paper.

Thus, four cylinder specimens of 4″ in diameter by 2″ high were made with a binder content higher than 14.56%, i.e., 15%, 16%, 17%, and 18%, respectively. Table 2.4 presents the weight measurements of the binder and aggregate of these specimens after cured overnight. The actual epoxy binder contents are slightly less than the binder contents used to prepare these cylinder specimens. To visually inspect the binder content, these specimens were cut vertically into two equal parts as shown in Figure 2.2. It is demonstrated that in the cross sections, many voids exist inside Specimen A. In addition, many irregular voids exist on its surface. This indicates that the amount of epoxy binder is not enough for Specimen A. In contrast, the surfaces of both Specimens C and D are heavily flushed with epoxy binder, which indicates that the contents of epoxy binder are more than sufficient. Nevertheless, Specimen B contains very few internal voids and its surface is covered with a very thin skin of epoxy binder. Therefore, it may be concluded that binder content of Specimen B is the most appropriate for the mix design of HFST epoxy-bauxite mortars. Accordingly, a binder content of 15.93% was selected for making epoxy-bauxite mortars used in preparing specimens for determining all physical and mechanical properties.

2.2.2 Regression Model for Binder Content

Determination of an appropriate binder content for the HFST epoxy-bauxite mortar is complicated and consists of a process of trial and error. The authors examined the surface variations of five FHST square specimens, including the three specimens in Table 2.3. Figure 2.3(a) shows the surface of one specimen constructed with the texture profile measurements. Figure 2.3(b) further shows one of the measured texture profiles, which precisely indicates that the HFST surface

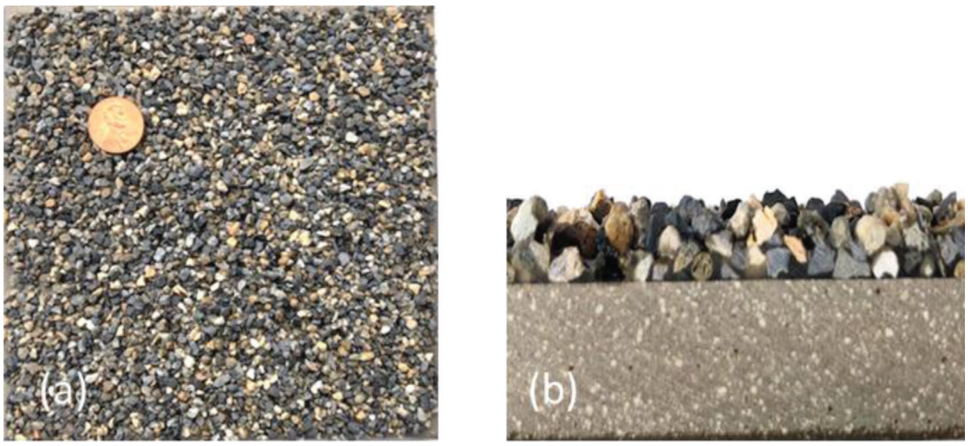

Figure 2.1 HFST square specimen: (a) surface close-up and (b) cross section.

Figure 2.2 Cylinder specimens: (a) plan view and (b) cross section.

TABLE 2.3
Weights of the epoxy binder and aggregate of the HFST square specimens

Specimen	Aggregate (g)	Epoxy Binder (g)	Binder % by Mass	MPD (mm)
1	35.64	6.0	14.41	1.895
2	37.44	6.10	14.01	1.924
3	33.13	5.96	15.25	1.956
Average	35.40	6.02	14.56	1.925

TABLE 2.4
Weights of the epoxy binder and aggregate of the cylinder specimens

Specimen	Aggregate (g)	Epoxy Binder (g)	Binder Content (% by mass)
A	830.76	144.54	14.82
B	818.50	155.09	15.93
C	809.19	163.51	16.81
D	789.10	180.91	18.65

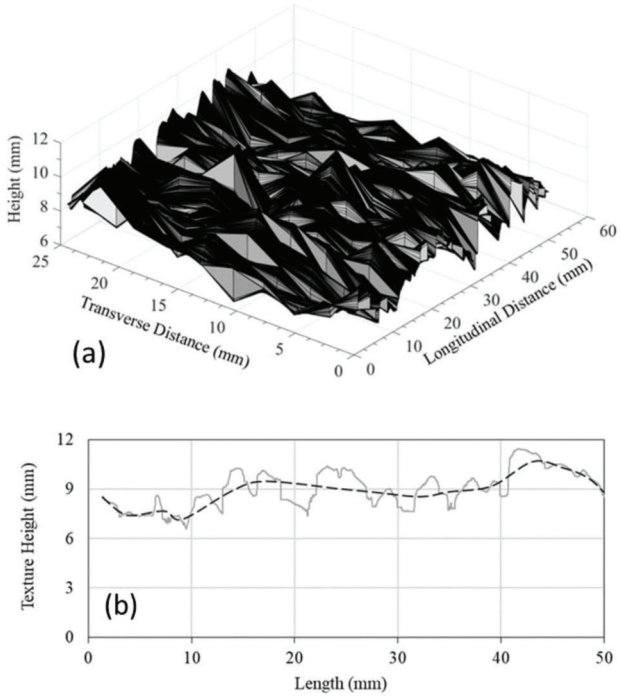

Figure 2.3 Visualization of HFST square specimen surface: (a) constructed surface and (b) texture profile.

is made up of valleys and spikes (grey solid line). As demonstrated earlier, the amount of binder in an actual HFST system is not sufficient for making epoxy-bauxite mortars. However, if the binder content is increased to fill all surface voids completely, excess binder may result in heavily flushed specimen surface (see Figure 2.2). In the authors' opinion, an appropriate binder content is approximately the sum of two parts: the amount of the epoxy binder for placing HFST, R0, and an additional amount of epoxy to cover the total surface area of all valleys beneath the MPD line (dark broken line), R1. R0 can determined in accordance with the supplier's recommended application rate, i.e., the binder % as shown in Table 2.3. It is a rough estimate that, however, the total area of the aggregate above the MPD line is equal to the total area of the valleys below the MPD line. Therefore, $R1$ is used to bond the aggregate intended to fill the valleys below the MPD line and varies with MPD. An empirical relationship can be developed to approximate the binder content as follows:

$$R = R_0 + R_1 = R_0 + (1.755 + 0.090MPD) \qquad \text{(Eq. 2.1)}$$

where R is the approximation of the epoxy binder content, percent by mass; $R0$ is the binder used to place the actual HFST, percent by mass; $R1$ is the additional binder as defined earlier, percent by mass; and MPD is the mean profile depth of the HFST surface as defined earlier, mm. The coefficient of determination (r_2) is 0.433.

2.3 Determination of Physical Properties

2.3.1 Poisson's Ratio

The Poisson's ratio of HFST epoxy-bauxite mortar was measured using a tensile test machine in accordance with method of ASTM E132, *Standard Test Method for Poisson's Ratio at Room Temperature* (ASTM, 2017). As shown in Figure 2.4 are the test set-up and the resultant variations of both the axial and lateral strains with the applied force. During the test, a force was applied to the specimen in a uniaxial direction. The applied force and the axial and lateral deformations were measured simultaneously. Notice that on the one hand, the applied force should be large enough to generate adequate axial and lateral strains to ensure sufficient accuracy for the measurements. On the other hand, the applied force should not cause collapse of the test specimen. The authors conducted pre-tests and concluded that a 133 pounds force with a loading speed of 0.663 pounds/s would fulfill the above needs.

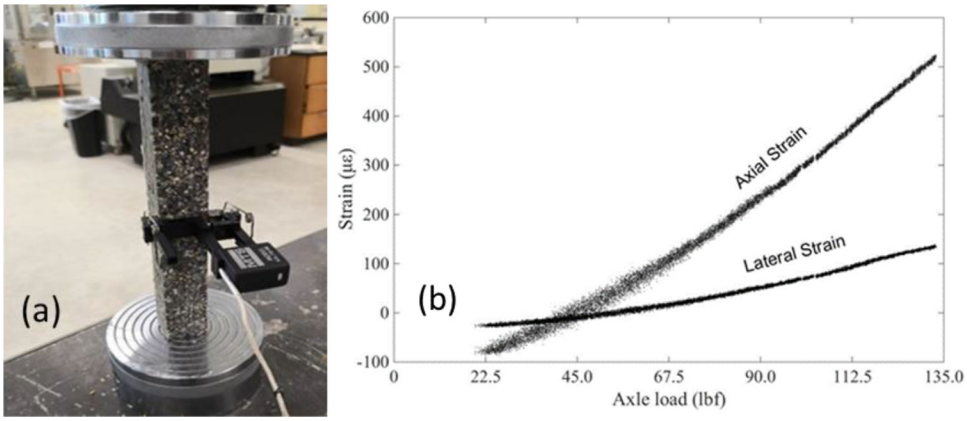

Figure 2.4 Poisson's ratio test: (a) set-up and (b) strain-force curve.

TABLE 2.5
Poisson's ratio test results

Specimen	Length (in.)	Width (in.)	Thickness (in.)	Poisson's Ratio
P-1	8.544	1.270	1.218	0.2727
P-2	8.576	1.265	1.220	0.2886
P-3	8.552	1.286	1.246	0.2844
P-4	8.541	1.283	1.239	0.3159

Note: Average Poisson's ratio = 0.29 and standard deviation = 0.018.

Four rectangular specimens were prepared using epoxy-bauxite mortars with an epoxy binder content of 15.93% as determined earlier. All tests were conducted at a room temperature of 77°F. It is shown that in Figure 2.4(b), both the axial and lateral strains are linearly proportional to the applied force. The axial strain experienced a greater increase rate as the applied force increased. Table 2.5 presents the dimensions of the four rectangular specimens used in the test and the corresponding Poisson's ratio test results. It is shown that the Poisson's ratios of these four specimens range from 0.2727 to 0.3159. The average of Poisson's ratio of HFST is 0.29 and the standard deviation is 0.018.The corresponding coefficient of variation (COV) is 6.3%, which indicates that the relative variability associated with the test results is low.

Figure 2.5 CTE test set-up.

2.3.2 Coefficient of Thermal Expansion

CTE is one of the important property aspects for analyzing the thermal incompatibility related distresses that may occur in an HFST system. However, there is no standard test method designated for determining the CTE of HFST epoxy-bauxite mortar. Wilson and Mukhopadhyay (2016) measured the CTE of HFST in accordance with both AASHTO T336, *Standard Method of Test for Coefficient of Thermal Expansion of Hydraulic Cement Concrete* (AASHTO, 2019) and ASTM C531, *Standard Test Method for Linear Shrinkage and Coefficient of Thermal Expansion of Chemical-Resistant Mortars, Grouts, Monolithic Surfacings, and Polymer Concretes* (ASTM, 2018b). They demonstrated that the AASHTO T336 test method tends to yield lower CTE. The AASHTO T336 was utilized by the authors due to the test equipment available. Figure 2.5 shows the set-up of the transducer, i.e., linear variable differential transformer (LVTD) for measuring the CTE of HFST cylinder specimen. During the test, both calibration and verification tests were first conducted to ensure accuracy using metal specimens with a known CTE of 8.89 $\times$ 10^{-6}/°F. The measured CTE was 9.06 $\times$ 10^{-6}/°F, about 1.9% greater than the actual CTE value. This indicates that the test method and equipment were accurate.

A total of four cylinder specimens of 4″ in diameter by 7″ in height were tested, and the results are presented in Table 2.6. Again, the binder content was 15.93% as

TABLE 2.6
Coefficient of thermal expansion (CTE) test results

Specimen	Height (in.)	Diameter (in.)	CTE ($\times 10^{-6}$/°F)
C-A	7.048	3.985	20.34
C-B	7.026	4.031	13.89
C-C	7.077	3.998	21.17
C-D	6.993	3.994	21.36

determined earlier. Initially, two specimens, i.e., Specimens C-A and C-B were tested, and their CTEs, respectively, were 20.34 $\times$ 10^{-6}/°F and 13.89 $\times$ 10^{-6}/°F. Because the difference between the two CTE values was greater than 0.3 $\times$ 10^{-6}/°F, i.e., the maximum difference specified in AASHTO T336, two more tests were further conducted on Specimens C-C and C-D, respectively. It is shown that the difference between the two CTE values is 0.19 $\times$ 10^{-6}/°F. Therefore, the average of these two CTE values, i.e., 21.27 $\times$ 10^{-6}/°F, was calculated as the CTE of the HFST epoxy-bauxite mortar. It is also worth noting that the CTE of HFST reported by Wilson and Mukhopadhyay (2016) is around 20.0 $\times$ 10^{-6}/°F. The CTE of epoxy mortar for concrete repairs is around 24.0 $\times$ 10^{-6}/°F reported by Kemphues (1972). In addition, the CTEs range between 7.4 $\times$ 10^{-6} /°F and 15.6 $\times$ 10^{-6} /°F for HMA (Islam & Tarefder, 2014) and between 4.8 $\times$ 10^{-6}/°F and 5.4 $\times$ 10^{-6}/°F for Portland cement concrete (PCC) (Dellinger & Poursee, 2016), which are evidently much less than the CTE of HFST epoxy-bauxite mortar.

2.4 Determination of Mechanical Properties

2.4.1 Dynamic Modulus

The dynamic modulus test of HFST epoxy-bauxite mortar was conducted according to AASHTO T342, *Determining Dynamic Modulus of Hot Mix Asphalt* (HMA) (AASHTO, 2015). Three cylinder specimens of 4″ in diameter by 6.7″ high, as shown in Figure 2.6(a), were prepared for the test. After the specimens had been fully cured, both ends of the specimens were cut off to achieve the desired specimen height. The bulk specific gravities of these specimens were first determined in accordance with AASHTO T166, *Standard Method of Test for Bulk Specific Gravity (Gmb) of Compacted Hot Mix Asphalt (HMA) Using Saturated Surface-Dry Specimens* (AASHTO, 2016). The density and water absorption of the calcined bauxite aggregate, i.e., 3.38 g/cm^3 and 0.81% as reported elsewhere (Li et al., 2017), were used in the calculation. As shown in Table 2.7, the average bulk specific gravity of HFST epoxy-bauxite mortar is 2.307, lower than the typical densities of HMA mixture and PCC. This may imply that the aggregate in the epoxy-bauxite mortar is not fully interlocked. In addition, the water absorption is 0.02%, which indicates that the HFST is basically a non-water absorption material.

During the test, four test temperatures (14°F, 39°F, 70°F, and 99°F) and six loading frequencies (25 Hz, 10 Hz, 2 Hz, 1 Hz, 0.5 Hz, and 0.1 Hz) were used by the authors. Presented in Table 2.8 are the modulus test results for the epoxy-bauxite mortar. Phase angle is an ideal indicator to distinguish between the elastic and viscous properties of a typical material (Ferry, 1980). A phase angle of 0° represents a perfectly elastic material and a phase angle of 90° represents a perfectly viscous material. As shown in Table 2.8, both the dynamic modulus and phase angle did not experience any significant changes as the loading frequency increased from 0.1 Hz to 25 Hz at 14°F. The resultant phase angles are less than 3.12°, which indicates that the epoxy-bauxite mortar is essentially an elastic material at low temperatures. However, the effects of loading frequency and the phase angle increased as temperature increased. The phase angles at 99°F varied from 22° to 36°, depending on the loading frequency, a huge increase as compared to the phase angle at 14°F. Therefore, the epoxy-bauxite mortar is a viscoelastic material, particularly at a temperature of 70°F or higher.

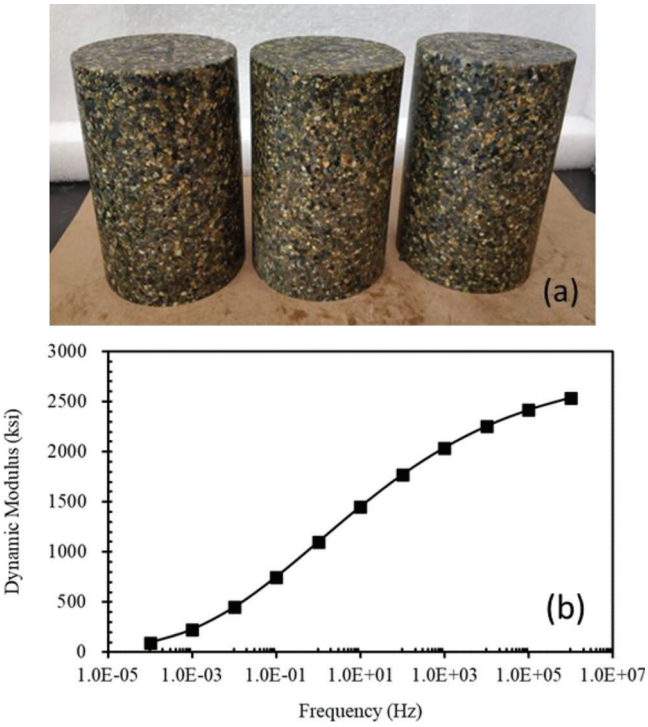

Figure 2.6 Dynamic modulus test: (a) cylinder specimens and (b) master curve.

The dynamic modulus master curve, as shown in Figure 2.6(b), was further developed for the epoxy-bauxite mortar of HFST in accordance with the method of AASHTO R62, *Standard Practice for Developing Dynamic Modulus Master Curves for Asphalt Mixtures* (AASHTO, 2017). This dynamic modulus master curve can be approximated using the general form of function as follows (AASHTO, 2017):

$$\log|E^*| = \delta + \frac{\alpha}{1 + e^{\beta + \gamma \log f_r}} \qquad \text{(Eq. 2.2)}$$

TABLE 2.7
Specimen dimensions and bulk specific gravities

Specimen	Diameter (mm)	Height (mm)	Specimen Mass in Air (g)	Surface-Dry Specimen Mass in Air (g)	Specimen Mass in Water (g)	Bulk Specific Gravity	Water Absorption (%)
Den-A	3.998	5.868	2,783.60	1,582.8	2,783.8	2.318	0.02
Den-B	4.002	5.846	2,759.60	1,559.9	2,759.8	2.300	0.02
Den-C	3.994	5.961	2,813.60	1,592.1	2,814.0	2.303	0.03
Average	3.994	5.891	2,785.60	1,578.3	2,785.9	2.307	0.02

TABLE 2.8
Dynamic modulus test results

Conditions		Dynamic Modulus (ksi)				Phase Angle (degree)			
Temperature (°F)	Frequency (Hz)	D-A	D-B	D-C	COV (%)	D-A	D-B	D-C	Std. Dev. (degree)
14	25	2,831	2,651	2,752	2.68	1.09	1.40	1.40	0.15
14	10	2,816	2,624	2,727	2.89	1.24	1.57	1.52	0.15
14	2	2,752	2,554	2,654	3.05	1.48	1.82	1.69	0.14
14	1	2,722	2,519	2,621	3.15	1.61	1.94	1.80	0.14
14	0.5	2,683	2,483	2,584	3.15	1.76	2.08	1.89	0.13
14	0.1	2,580	2,391	2,482	3.11	2.17	2.52	2.34	0.14
40	25	2,524	2,278	2,508	4.60	5.80	2.98	2.61	1.42
40	10	2,402	2,195	2,461	4.84	3.07	3.08	2.69	0.18
40	2	2,272	2,067	2,352	5.39	3.74	3.9	3.13	0.33
40	1	2,211	2,005	2,299	5.67	3.97	4.23	3.32	0.38
40	0.5	2,144	1,943	2,244	5.94	4.35	4.56	3.59	0.42
40	0.1	1,974	1,779	2,100	6.76	5.16	5.49	4.26	0.52
70	25	1,551	1,384	1,640	6.96	8.20	8.35	7.20	0.51
70	10	1,433	1,255	1,537	8.27	9.23	9.65	7.86	0.76
70	2	1,197	1,026	1,332	10.58	11.22	12.18	9.44	1.14
70	1	1,096	930	1,244	11.79	12.24	13.4	10.19	1.33
70	0.5	998	836	1,155	13.07	13.26	14.67	11.06	1.49
70	0.1	774	629	939	16.23	16.11	17.97	13.53	1.82
100	25	663	505	676	12.62	21.70	24.18	20.42	1.56
100	10	529	392	552	14.37	24.34	26.95	23.42	1.50
100	2	331	230	349	17.16	28.68	30.92	28.55	1.09
100	1	264	179	279	18.20	29.63	31.51	30.28	0.78
100	0.5	255	139	216	23.72	22.80	31.52	31.74	4.16
100	0.1	134	78	107	21.69	45.46	28.95	32.74	7.06

$$\log f_r = \log f + a_1(T_R - T) + a_2(T_R - T)^2 \qquad \text{(Eq. 2.3)}$$

where $|E^*|$ is the dynamic modulus, psi; f_r is the reduced frequency, Hz; f is the loading frequency, Hz; T_R and T are the reference and test temperatures, respectively, °F; α, β, γ, δ, a_1 and a_2, i.e., the fitting parameters, respectively, are 6.636, -2.715, -3.182, -0.364, 0.019, and 0.00029; $\sum error^2$ is the sum of squared errors and is equal to 0.00171 in this case; n is the number of temperature/frequency combinations used in the test.

2.4.2 Crack Resistance

The flexibility index (FI) of HSFT epoxy-bauxite mortar was measured using the semi-circular bending (SCB) test according to AASHTO TP124, *Provisional Standard Method of Test for Determining the Fracture Potential of Asphalt Mixtures Using Semicircular Bend Geometry (SCB) at Intermediate Temperature* (AASHTO, 2018b). During the test, the specimens were conditioned in an environmental chamber at 77°F for 3 hours. The force was applied at a rate of 50 mm (2″)/min until the load dropped below 22.5 pounds. A total of seven specimens were tested and the results are presented in Table 2.9. The HFST epoxy-bauxite mortar experienced very low FI values. Only two specimens' FI values are over 1.5 but less than 2.0. Benefiting from the higher peak load, however, the fracture energy of the specimens is higher than that of HMA mixture, i.e., 800 to 2,500 J/m^2 as reported elsewhere (Al-Qadi et al., 2015). For the same reason, the tensile strength of the specimens is greater than that of HMA, i.e., 87 psi or less. It is evident that while the fracture energy or FI tends to exhibit great variations, the SCB test may provide mix results about the cracking resistance of HFST epoxy-bauxite mortar.

Therefore, the overlay test (OT) was employed to further evaluate the crack resistance of the HFST epoxy-bauxite mortar according to the Texas Department of Transportation (TxDOT) test method, i.e., Tex-248-F, *Test Procedure for Overlay Test* (TxDOT, 2008). As shown in Figure 2.7 is a photo of the test set-up for HFST OT using a universal testing machine (UTM). A total of four specimens were tested with a maximum load ranging from 384 pounds to 432 pounds. As illustrated in Figure 2.8, the load reduction during the test was not significantly after 1,000 load cycles. Presented in Table 2.10 are the overly test results for these four specimens. The average load reduction of HFST is about 31.62%, indicating that this type of material has very good cracking resistance. The crack progression rate (CPR), commonly used to assess the cracking property during the crack propagating (Garcia et al., 2017), was also calculated from the load reduction curves. The average CPR is 0.046, which indicates a very good anti-cracking performance for the tested HFST epoxy-bauxite mortar.

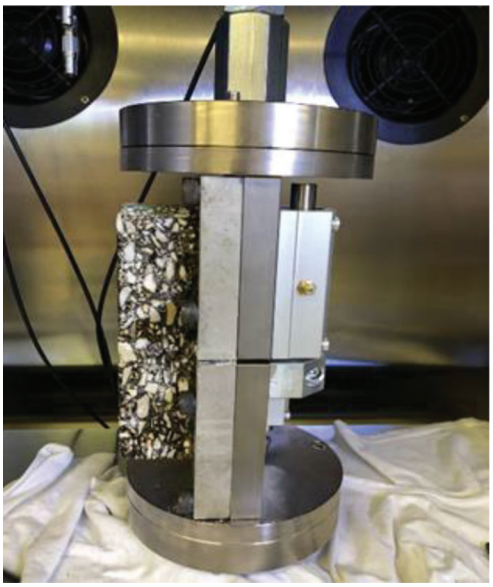

Figure 2.7 Set-up of UTM OT test.

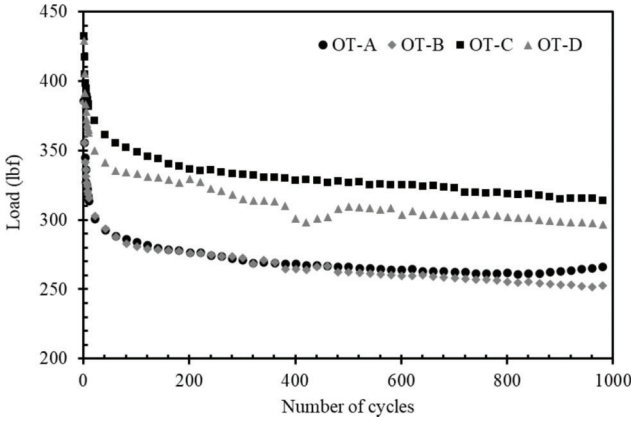

Figure 2.8 Load reduction curves.

TABLE 2.9
Flexibility index test results

Specimen	Dimension (in.)			Fracture Energy (J/m^2)	Flexibility Index	Tensile Strength (psi)
	Diameter	Thickness	Ligament			
F-A	5.837	1.906	2.369	8,278.76	1.89	358
F-B	5.919	1.913	2.385	3,868.58	0	425
F-C	5.886	1.959	2.380	3,557.81	0	395
F-D	5.929	1.950	2.390	4,114.51	0	413
F-E	5.888	1.952	2.382	7,485.05	1.85	374
F-F	5.933	1.949	2.386	3,972.49	0	393
F-G	5.911	1.938	2.374	4,041.48	0	396

TABLE 2.10
Overlay test (OT) results

Specimen	TO-A	OT-B	OT-C	OT-D	Average	COV (%)
Crack progression rate (CPR)	0.041	0.049	0.042	0.046	0.046	8.31
Reduction (%)	32.65	34.63	28.01	31.18	31.62	8.82

3. EARLY DISTRESSES AND THEIR MECHANISMS IN HIGH FRICTION SURFACE TREATMENT

3.1 HFST Initiative Projects

3.1.1 Existing Site Conditions

Of the 25 HFST projects, 21 projects were included in the INDOT's HFST initiative and 4 projects were included in a pavement resurfacing project. Pre- and post-construction inspections were only conducted at the 21 HFST initiative projects to evaluate the possible effects of curve length and radius, traffic characteristics such as Annual Average Daily Traffic (AADT), truck %, posted speed, drainage condition, and existing pavement condition (surface distresses) on the durability of HFST, as shown in Table 3.1. All curves were simple circular curves, except for the five curves were reverse curves consisting of two (SR-446, SR-65, SR-450, and SR-56) or three (SR-237) adjoining circular curves. The radii of these curves ranged between 148 ft. (i.e., SR-32) and 1,391 ft. (i.e., US-24a). The lowest traffic volume was 133 AADT at the site on SR-56 and the highest traffic volume was 5460 AADT at the site on SR-23. The percentages of trucks varied between 3% at the site on SR-450 and 20% at the four sites on US-35 and US-24, respectively.

Inspection results revealed that the drainage conditions were rated as good at 15 sites. At the sites with a fair drainage rating, possible drainage problems commonly occurred on the inner curve. The most common type of distress in the existing pavements was cracking, including transverse, longitudinal, and block cracks. Transverse cracks occurred mostly in the driving lanes. Longitudinal cracks occurred either in the driving lanes or the inside shoulder of the curve with drainage problems. The block cracks tended to occur on the inside shoulder experiencing drainage problems. The occurrence of transverse cracks was normalized by dividing the total number of cracks by the curve length. However, a subjective rating scale of 0 (no cracks) to 5 (severe cracks) was employed to rate the longitudinal and block cracks. The overall pavement conditions were subjectively rated in terms of mainly cracks. Notice that although the existing pavement was a new HMA mill and fill on SR-32, the distresses in the pavement surface before mill and fill would ultimately affect the durability of HFST.

3.1.2 HFST Constructions

The HFST projects, respectively, were placed between August and October 2018. Table 3.2 is the information regarding road, type of existing pavement, Average Annual Daily Traffic (AADT), treatment length,

TABLE 3.1
Site and existing pavement conditions

		Geometrics		Traffic Characteristics				Existing Pavement				
No.	Road	Length (ft)	Radius (ft)	AADT	Truck (%)	Post Speed (mph)	Drainage	Type	Trans. Crack[1]	Long. Crack[2]	Block Crack[3]	Overall Condition
1	SR-32	256	148	9,679	5%	40	Good	New HMA[4]	0.000	0.0	0.0	New
2	US-35a	1,050	1,324	2,886	20%	No	Good	Chip seal	3.620	2.0	1.2	Fair
3	US-35b	1,486	1,384	2,886	20%	30	Fair	Chip seal	3.298	2.5	2.0	Fair
4	SR-25	1,312	518	4,282	10%	35	Good	Chip seal	1.676	0.2	0.1	Good
5	SR-62a	509	303	2,754	7%	35	Good	Chip seal	5.499	0.0	0.0	Good
6	SR-62b	558	236	2,282	8%	25	Fair	Chip seal	3.774	0.5	0.0	Good
7	SR-62c	682	293	2,176	8%	30	Good	Chip seal	4.250	0.1	0.0	Good
8	SR-62d	577	302	2,367	7%	35	Good	Chip seal	2.944	0.1	0.0	Good$^-$
9	SR-237	3,202	353	685	5%	35	Good	Chip seal	0.250	0.1	0.0	Good
10	US-24a	883	1,391	5,205	20%	No	Fair	Chip seal	3.402	1.0	0.2	Good$^-$
11	US-24b	945	1,383	5,205	20%	No	Fair	Chip seal	3.493	1.0	0.2	Good$^-$
12	SR-14	289	503	3,675	18%	45	Fair$^-$	Chip seal	6.581	0.8	2.0	Fair$^-$
13	SR-23	568	577	5,460	17%	40	Fair$^+$	Chip seal	7.938	0.7	0.2	Fair
14	SR-43	492	131	2,043	18%	15	Good	Chip seal	1.420	0.1	0.0	Good$^+$
15	SR-56	735	382	133	16%	30	Good	Chip seal	1.905	0.5	0.0	Good
16	SR-65	1,083	773	3,207	9%	35	Good	Chip seal	2.497	0.0	0.0	Good
17	SR-205a	420	483	3,641	4%	35	Good	Chip seal	5.239	0.1	0.0	Fair
18	SR-205b	823	591	3,641	4%	40	Good	Chip seal	9.464	0.1	0.0	Fair
19	SR-257	787	164	527	33%	20	Fair	Chip seal	7.112	3.0	1.0	Poor
20	SR-446	1,686	412	1,705	17%	25	Good	Chip seal	0.950	0.1	0.0	Good
21	SR-450	735	166	888	3%	25	Fair	Chip seal	1.089	1.0	0.2	Good$^-$

Note:
The negative and positive signs indicate that the condition ratings are slightly below and above Good or Fair, respectively.
[1]Transverse crack rated as the number of cracks per 100 feet.
[2]Longitudinal crack rated using a scale of 0 (no cracks) to 5 (severe cracks).
[3]Block crack rated using the same 0–5 scale.
[4]1.5″ mill and fill.

TABLE 3.2
Information on 21 HFST projects

No.	Road	Existing Surface	AADT	Construction Date	Air Temperature (°F)[1]	Surface Preparation	Epoxy Resin (L/yd^2)	Calcined Bauxite (lb/yd^2)
1	SR-32	New HMA[2]	9,679	8/13/2019	61–84	Shotblasting	25.07	15.32
2	US-35a	Chip seal[3]	2,886	9/14/2019	63–84	Vacuum	27.21	19.32
3	US-35b	Chip seal	2,886	9/18/2019	64–90	sweeping	23.41	20.81
4	SR-25	Chip seal	4,282	10/24/2019	30–52		26.75	14.19
5	SR-62a	Chip seal	2,754	10/12/2019	70–88		28.52	13.53
6	SR-62b	Chip seal	2,282	10/2/2019	70–90		28.60	12.76
7	SR-62c	Chip seal	2,176	10/3/2019	68–90		29.61	13.11
8	SR-62d	Chip seal	2,367	10/7/2019	72–90		26.96	12.96
9	SR-237	Chip seal	685	10/6/2019	37–54		26.31	13.40
10	US-24a	Chip seal	5,205	10/29/2019	36–52	Scarification	27.17	17.47
11	US-24b	Chip seal	5,205	10/29/2019	36–52	milling	26.60	15.72
12	SR-14	Chip seal	3,675	10/24/2019	27–521		24.86	20.83
13	SR-23	Chip seal	5,460	10/26/2019	39–52		23.65	15.59
14	SR-43	Chip seal	2,043	10/28/209	36–57		21.20	16.90
15	SR-56	Chip seal	133	10/9/2019	72–88		27.40	13.09
16	SR-65	Chip seal	3,207	10/8/2019	72–88		29.59	11.98
17	SR-205a	Chip seal	3,641	10/23/209	36–61		23.68	19.24
18	SR-205b	Chip seal	3,641	10/23/2019	36–61		25.02	19.32
19	SR-257	Chip seal	527	10/13/2019	37–55		28.00	14.97
20	SR-446	Chip seal	1,705	10/19/2019	36–57		24.44	16.44
21	SR-450	Chip seal	888	10/17/2019	39–63		20.25	17.70

Note:
Not even a single sample failed at the interface between the HFST and underlying chip seal or between the chip seal and underlying HMA pavement. This implies that chip seal may not affect the durability of HFST and scarification milling does not necessarily provide better interface bonding between the HFST and chip seal, compared to vacuum sweeping.
[1]Air temperature range on the construction date.
[2]New HMA is 9.5-mm HMA mixture.
[3]Chip seals are all single layer chip seals.

Figure 3.1 Photos of surface preparation operations: (a) shotblasting, (b) sweeping, and (c) scarification.

construction time, daily air temperature, method of surface preparation, and material application rates. The treatment length varies from 256 ft. to 3,200 ft., depending on the geometric features of the curve. In general, a short curve represents a sharp curve. The existing pavements at all sites except for that on SR-32 are chip sealed HMA pavements. The pavement surface on SR-32 is a new 1.5″ mill and fill HMA surface with more than 30 days of curing. Three techniques, including shotblasting, vacuum sweeping, and scarification milling (Figure 3.1), respectively, were used for existing pavement surface preparations. Shotblasting was used to roughen the surface and remove the asphalt binder on the new mill and fill HMA surface on SR-32. For chip seal pavements, either vacuum sweeping or scarification milling was used, depending on the pavement conditions. It was hypothesized that scarification milling could reduce the potential effects of chip seal on the durability of HFST. Before the construction of HFST, areas with severe cracks in the existing pavements were removed and patched with HMA mixes. However, no crack filling was carried out to fill both transverse and longitudinal cracks in the existing pavements. There was a thought that these cracks would be filled in place by the epoxy binder while placing HFST.

The air temperature is the air temperature range during the day when placing HFST. Notice that as the manufacturer's recommended temperature for mixing and placing the epoxy binder ranges between 50°F and 95°F. However, 12 HFST projects were constructed below the recommended temperatures. Currently, the epoxy binders for HFST are thermoset resin binders that require heat for curing. In the authors' opinion,

working with epoxy resins at low temperatures will not only require much longer cure time, but also compromise the performance of the final product. All of these 21 HFSTs were placed using the semi-automated application method. The manufacturer's recommended application rates were 1.58 to 1.88 L/m^2 for epoxy binder and 7.56 to 10.80 kg/m^2 for calcined bauxite aggregate. As shown in Table 3.2, the epoxy binder application rates are higher than 1.58 L/m^2 at these 21 sites and higher than 1.88 L/m^2 at nine of these 21 sites. The calcined bauxite application rates are lower than 7.56 kg/m^2 at seven sites and are high than 10.80 kg/m^2 at two sites, which implies the calcined bauxite application rates are relatively low.

It can also be found that by careful inspection of Table 3.2, more materials were applied at the HFST sites with the existing pavements pre-treated by scarification milling than by vacuum sweeping. The average epoxy binder and aggregate application rates, respectively, are 1.97 L/m^2 and 9.01 kg/m^2 for scarification milling, and 1.81 L/m^2 and 8.14 kg/m^2 for vacuum sweeping. On average, the epoxy binder application rate increased by 8.1% for surface preparation by scarification milling compared with vacuum sweeping, an increase of 4.5% compared to the manufacturer's recommended maximum application rate. However, the increase in the aggregate application rate for scarification milling is negligible compared to that for vacuum sweeping. It should be pointed out that at these sites, the epoxy binder application rate varied more significantly for surface preparation by scarification milling than by vacuum sweeping. On the one hand, more epoxy binder will be needed when the existing pavement surface is prepared by scarification milling than by vacuum sweeping. On the other hand, the surface texture produced by scarification milling varies more greatly than that by vacuum sweeping. This may cause issues about the determination of both the epoxy binder and bauxite aggregate application rates, thereby resulting in negative impacts on both the cost and quality of HFST construction.

3.2 Identification of Most Common Early Distresses

3.2.1 Field Investigations

Field investigations consisted of site visits, reviewing historical pavement records, taking core samples, in-situ testing, and laboratory testing. Two site visits, one before and one after the construction of HFST, were made for all of these 21 HFST projects. The pre-construction site visit was conducted as shown previously. Historical pavement records comprised of road survey data, historical coring information, and pavement design documents. The post-construction site visit focused on the early HFST distresses and was performed in April 2019 when these 21 HFSTs had gone through an entire winter season and experienced the effects of freeze-thaw cycles and snowplows. Photographs and sketches were made to show the physical positions and types of distress occurred in all of these 21 HFSTs. Infrared images were also taken to determine the possible issues beneath the HFST. It was observed that the existing pavements were in good conditions at the majority of these 21 HFST sites and in fair condition at some of these 21 HFST sites. At the HFST site on SR-257, the existing pavement was in poor to fair condition before the construction of HFST.

Six HFST sites, including SR-32, SR-205b, US-35a, SR-114, SR-446, and SR-450, were selected in terms of the existing pavement condition, surface preparation, and geographical location for in-situ falling weight deflectometer (FWD) and ground penetration (GPR) tests before the construction of HFST to evaluate the structural condition of the existing pavement. The center FWD deflections, i.e., the deflections at the center of loading plate, varied between 0.16 mm (6.57 mils) and 0.23 mm (9.13 mils) at the HFST sites on SR-32, SR-205b, US-35a, and SR-14. The center deflections varied between 0.44 mm (17.4 mils) and 0.52 mm (20.5 mils) at the two HFST sites on SR-446 and SR-450, respectively. It was also revealed that the deflections in the lanes in different directions may be very different even on a small curve. A total of 14 HFST core samples were further taken at four of the above selected six HFST sites, including SR-32, SR-205b, US-35a, and SR-446, to examine the possible defects in the underlying layers of the existing pavement and the HFST-substrate interface bonding. To quantitatively evaluate the bonding at the HFST-substrate interface, pull-off testing was conducted on the core samples at room temperature in the laboratory, thereby eliminating the possible effects due to the variations associated with the ambient temperatures between different sites. Presented in Figure 3.2 are the photos of failed samples after pull-off testing, including three from HFSTs and one from a chip seal pavement. It is shown that all samples, including the one from chip seal pavement, failed in the HMA layer below the chip seal, regardless of the method of surface preparation.

3.2.2 Most Common Early Distresses

The HFST distresses that have been reported are commonly divided into four categories such as aggregate loss, interface debonding (delamination), substrate failure, and reflective cracking (Waters, 2011; Wilson & Mukhopadhyay, 2016). Hereinafter, debonding refers to the failure of interface between the HFST and underlying substrate, and delamination refers to the failure of interface between the chip seal and underlying HMA surface. Both debonding and delamination may result in an area of the pavement layers above the interface missing. It has been recognized that the probable causes for HFST distresses include, but are not limited to, material failures (insufficient mixing or cure, dirty or wet aggregate), construction (surface preparation, material application, curing, and ambient temperature), and candidate selection (pavement condition and structural capacity). As continuous advances

Figure 3.2 Photos of failed samples after pull-off testing: (a) HFST with scarification milling, (b) HFST with vacuum sweeping, (c) HFST with shot-blasting, and (d) chip seal pavement.

Figure 3.3 Most common early HFST distresses: (a) cracking, (b) aggregate loss, (c) delamination, and (d) surface wrinkling.

in HFST technologies, especially in epoxy binder properties and automated construction, have taken place over the past decade, it becomes possible to reliably ensure material quality, sufficient binder mixing and cure, uniform binder and aggregate applications, and accurate specification compliance. Based on the observations made during the post-construction site visits by the authors, it was found that the most common types of early HFST distresses are reflective cracking, aggregate loss, delamination, and surface wrinkling (slippage) as illustrated in Figure 3.3. Notice that reflective cracking thereafter refers to any types of reflective cracks due to the discontinuities on the surface of existing pavement, including cracks, pothole patches, and alligator crack repair patches.

Table 3.3 presents the occurrences of these four most common distresses observed at the HFST sites during the post-construction visits. The crack rate refers to as the ratio of the total number of cracks in the existing pavement before the construction of HFST to the total number of cracks in HFST and is calculated as a percentage. All of these HFST sites, except for the one on SR-56, had experienced reflective cracking to some extent. It is also interesting to note that the crack rate

TABLE 3.3
Summary of early HFST distresses occurred after the first winter

No.	Road	AADT	Cracks (number)			Aggregate Loss	Delamination	Surface Wrinkling
			Before	After	Rate	(Yes or No)	(Yes or No)	
1	SR-32	9,679	0	15	∞	No	No	No
2	US-35a	2,886	38	36	95%	No	No	Yes
3	US-35b	2,886	49	22	45%	No	No	No
4	SR-25	5,688	22	18	82%	No	No	Yes
5	SR-62a	2,754	28	24	86%	No	No	Yes
6	SR-62b	2,282	21	26	124%	No	No	No
7	SR-62c	2,176	29	50	172%	No	No	Yes
8	SR-62d	2,367	17	30	176%	No	No	No
9	SR-237	685	8	2	25%	No	No	No
10	US-24a	5,205	30	29	97%	Yes	No	Yes
11	US-24b	5,205	33	6	18%	No	No	No
12	SR-14	3,675	19	27	142%	No	No	No
13	SR-23	5,460	45	42	93%	Yes	Yes	No
14	SR-43	2,043	7	18	257%	No	No	No
15	SR-56	133	1	0	0%	No	No	No
16	SR-65	3,207	27	48	178%	No	No	Yes
17	SR-205a	3,641	22	27	123%	Yes	Yes	Yes
18	SR-205b	3,641	78	74	95%	Yes	Yes	Yes
19	SR-257	527	56	31	55%	Yes	No	No
20	SR-446	1,705	16	15	94%	Yes	Yes	No
21	SR-450	888	8	5	63%	No	Yes	No

increases as the number of cracks in the existing pavement before the construction of HFST. Aggregate loss was observed at six sites where scarification milling was utilized for surface preparation. Coincidently, delamination is another common distress observed at all these six HFST sites except for the one on SR-450. Surface wrinkling (slippage) was observed at eight of these 21 HFST sites, regardless of the method of surface preparation. No slippage cracks occurred. It was also observed that surface wrinkling commonly occurred in the HFST along the direction of traffic. The two HFST projects on US-35 are located close to each other. They were installed around the same time and had the same AADT. Interestingly, one HFST, i.e., the HFST on US-35a experienced surface wrinkling, and the other, i.e., the HFST on US-35b, did not have any surface wrinkling. It can be concluded that reflective cracking is the most common early HFST distress occurred at the HFST sites in Indiana, followed by surface wrinkling, aggregate loss, and delamination at the interface between the chip seal and HMA pavement.

3.3 Mechanisms of Early Distresses

3.3.1 Reflective Cracking

Presented in Figure 3.4 are the photos of typical reflective cracks taken by the authors during the post-construction visits. Reflective cracking mainly includes both transverse cracking and longitudinal cracking as shown in Figures 3.4(a) and 3.4(b), whereas transverse cracking is the predominant type of reflective cracking. In addition, any other discontinuities in the existing pavement surface, such as patching for pothole or fatigue cracks, can cause reflective cracking around the boundary of the patch as shown in Figure 3.4(c). Once reflective cracking has occurred, the differential thermal movements will further make the HMA pavement adjacent to the crack to curl, which will accelerate the deterioration of the adjacent HFST and underlying pavement as illustrated in Figure 3.6(d).

Generally speaking, reflective cracking may occur due to the effect of traffic load, temperature variation, or both. Plotted in Figure 3.5 are the development trends of reflective cracking at three HFST sites, including SR-32, US-35a, and US-35b. On November 28, 2018 when the HFST on SR-32 had been in service for 3 months and the two HFSTs on SR-35 had been in service for 2 months, there were not any cracks in the HFSTs on SR-32 and US-35b, and only one crack in the HFST on US-35a. This implies that traffic loading may not be the most important contributing factor for reflective cracking. Afterwards, the reflective cracking developed at an increasing rate that relied seemingly on the number of cracks in the existing pavement before the construction of HFST. The more the cracks in the existing pavement, the more rapid the development of reflective cracking through the HFST. The development of reflective cracking in the HFST on SR-32 is slower than that on SR-35a or SR-35b because the existing pavement at the site on SR-32 is a new mill and fill HMA pavement. As illustrated by the HFST on SR-32 in Figure 3.5, although a mill and fill could not prevent the reflection of the cracks through the HFST, it could slow the development of reflective cracking in HFST.

To help reliably identify the most probable cause(s) for reflective cracking and to provide material property

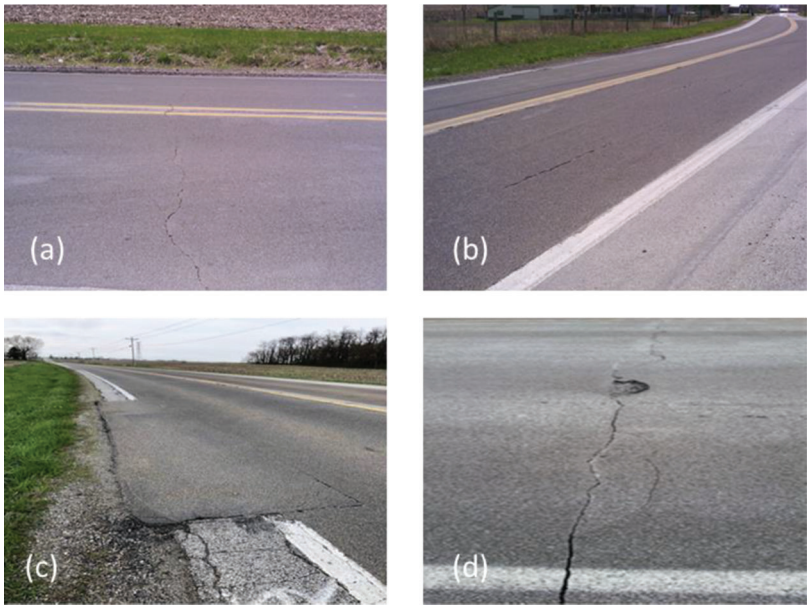

Figure 3.4 Typical reflective cracks in HFST: (a) transverse reflection, (b) longitudinal reflection, (c) patch reflection, and (d) crack deterioration.

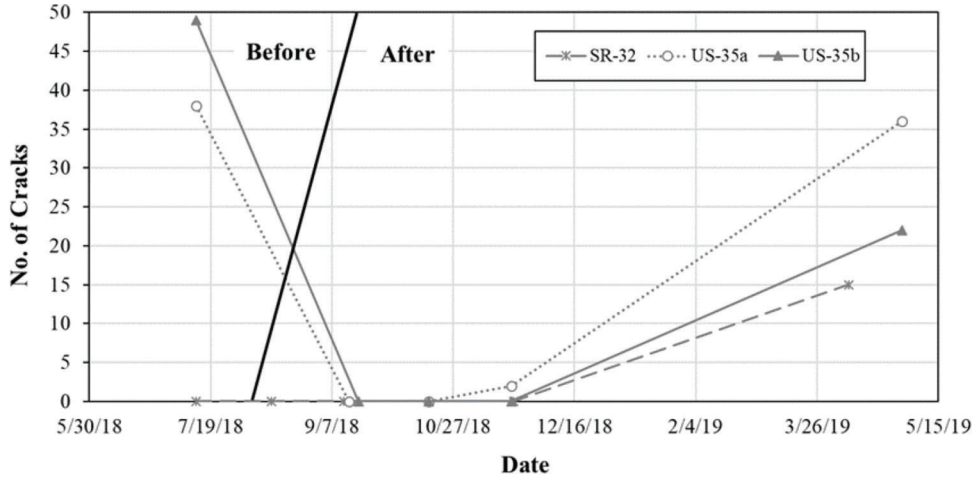

Figure 3.5 Illustration of cracking development trends.

inputs for mechanistic analysis of HFST, the authors conducted comprehensive laboratory testing to determine the properties of HFST epoxy-bauxite mortar, including CTE, dynamic modulus, and crack resistance (Islam & Tarefder, 2014). It was found that the crack progression rate (CPR) and CTE of the HFST epoxy-bauxite mortar, respectively, are 0.046 and 38.28 $\times$ 10^{-6}/°C (Wei et al., 2020). Evidently, a typical HFST has not only high fracture energy and tensile strength, but also high cracking resistance to traffic loading, compared to HMA mixtures. On the other hand, The CTE of HFST epoxy-bauxite mortar is much higher than that of typical HMA mixtures, i.e., 12.6 $\times$ 10^{-6}/°C (Wilson & Mukhopadhyay, 2016). Consequently, daily, or seasonal temperature variations will produce repeated differential thermal movements between the HFST and underlying pavement and severer thermal stresses in the critical zone in the HFST, thereby resulting in reflective cracking through the HFST. As pointed out earlier, no crack filling had been carried out to fill both transverse and longitudinal cracks in the existing pavements at these 21 HFST sites. Figures 3.6(a) and 3.6(b), respectively, present two images of the HFST surface taken at the same location. As shown in the digital image, the cracks in the HFST surface appear very small. Nevertheless, it can be seen that inthe infrared image, these cracks are indeed very large. Evidently, the above does not support the thought that the cracks in the existing pavement would be filled by the epoxy binder during application.

Two-sample t-tests were further conducted to determine the effect of surface preparation such as scarification milling and vacuum sweeping on the development of reflective cracking. To accomplish this, two variables, including (a) crack rate (see Table 3.3); and

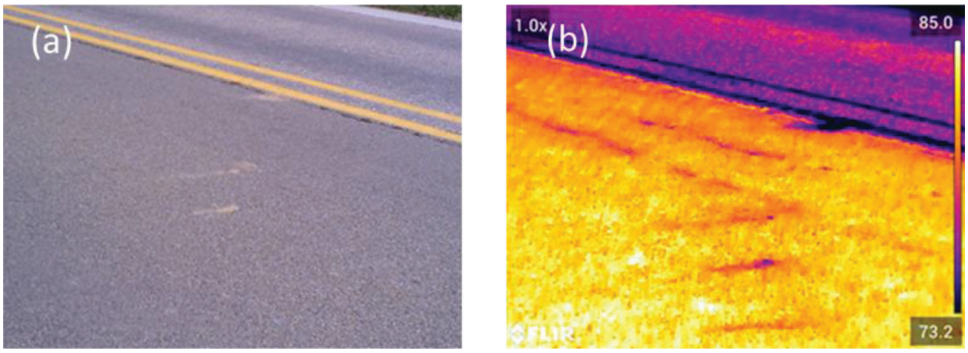

Figure 3.6 Photos of HFST cracks in the same area: (a) digital image and (b) infrared image.

TABLE 3.4
T-test results for cracks reflected rates and crack intervals

Variable	H0	H1	p-value	Decision
Crack rate	$\mu_{broom} = \mu_{milling}$	$\mu_{broom} < \mu_{milling}$	0.51	Fail to reject H0
Crack interval	$\mu_{broom} = \mu_{milling}$	$\mu_{broom} < \mu_{milling}$	0.15	Fail to reject H0

(b) crack interval, i.e., the interval distance between two consecutive cracks, were examined, respectively. The null and alternative hypothesis hypotheses in both t-tests are as follows:

Null Hypothesis (H0): $\mu_{vacuum} = \mu_{milling}$
Alternative Hypothesis (H1): $\mu_{vacuum} < \mu_{milling}$

where μ_{vacuum} is the mean of the crack rate or crack interval for vacuum sweeping and $\mu_{milling}$ is the mean of the crack rate of crack interval for scarification milling.

Presented in Table 3.4 are the results of the two t-tests. The calculated p-values, respectively, are 0.51 and 0.15 for the crack rate and crack interval. As both the calculated p-values are greater than 0.05, i.e., the significance level, it is not justified to reject the null hypothesis for either the crack rate or crack interval. The above can be extended to imply that there is no statistically significant difference between vacuum sweeping and scarification milling in terms of the reflective cracking development in the HFST.

3.3.2 Aggregate Loss

As mentioned earlier, a total of six HFST sites experienced aggregate loss after an entire winter. On the one hand, a common feature associated with these six HFST sites is that the surfaces of the existing pavements were prepared by scarification milling. On the other hand, these six HFST sites account for 50% of the total number of HFST sites with surface preparation by scarification milling. Therefore, it is very natural to attribute the aggregate loss at these six HFST sites to scarification milling. Scarification milling is designed to produce a surface consisting of parallel ridges and valleys with a cutting depth of up to ¾″ (19 mm) (INDOT, 2019). The authors conducted texture testing on the existing pavements at these 21 HFST sites. It was found that the mean profile depths (MPDs) ranged between 1.30 mm and 1.50 mm for the surfaces produced by scarification milling, and between 0.25 mm and 0.70 mm for the surfaces produced by vacuum sweeping. This suggests that additional epoxy binder will be needed for a surface produced by scarification milling, compared to a surface produced by vacuum sweeping. In addition, concerns may also arise associated with the field operation of scarification milling on horizontal curves, especially small, sharp curves. Some areas on the curve may be left un-scarified due probably to the effect of superelevation, unevenness of the existing pavement surface, or both. In Indiana, a rural two-lane highway may consider a maximum superelevation of up to 12% for horizontal curves (AASHTO, 2018a). Therefore, the applied epoxy binder applied over the prepared surface may, to some extent, flow to the low side of a super-elevated section during curing. The un-scarified areas are more likely to have insufficient amount of epoxy binder. Consequently, the film of epoxy binder in these areas may not be thick enough to retain the aggregate and early aggregate loss will occur after opening to traffic as shown in Figure 3.7(a).

Moreover, the application of epoxy binder such as mixing or curing relies significantly on the ambient temperature. In particular, the curing time for epoxy binder increases greatly as the ambient or pavement temperature decreases. It is shown that in Tables 3.2 and 3.3, the six sites with aggregate loss were all installed at a temperature lower than 60°F. As recommended by the manufacturer, it normally takes at least 6 hours for the epoxy binder to cure at a temperature of 65°F. On the one hand, low temperature curing of the epoxy binder may cause variations in the epoxy binder system, thereby affecting the mechanical properties of the epoxy binder system. On the other hand, maintaining

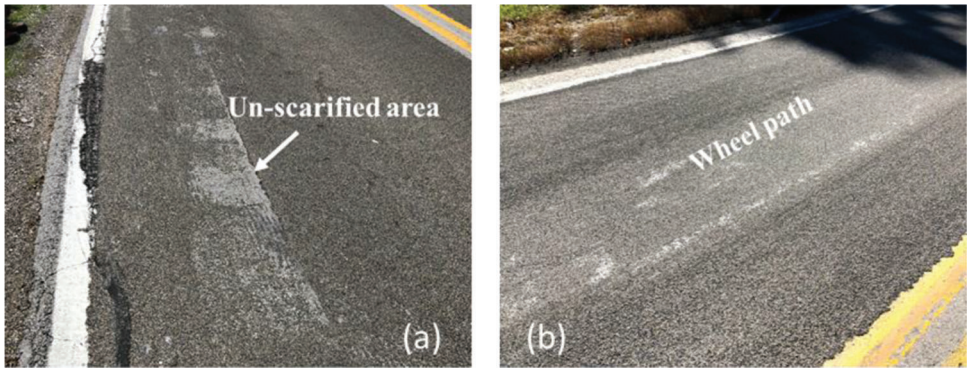

Figure 3.7 Photos of HFST aggregate loss: (a) un-scarified area and (b) wheel path.

traffic control for more than six hours will cause substantial inconvenience to motorists and increase the total cost for installing HFST. It may become possible the epoxy binder may not be fully cured to hold the aggregate firmly before opening to traffic. As a result, excessive aggregate loss may arise in the wheel paths as shown in Figure 3.7(b) after opening the HFST to traffic. The above agrees with a recommendation made by Wilson and Mukhopadhyay (2016), i.e., epoxy resin binders should not be applied at temperatures below 60°F.

3.3.3 Delamination

As pointed out earlier, scarification milling was utilized or surface preparation at all of the five HFST projects experiencing delamination at the interface between the chip seal and underlying HMA pavement. Figure 3.8(a) presents a photo of the delaminated HFST, which clearly shows the layers of HMA, chip seal, and HFST. There are two probable causes for this type of delamination, including shear stress and scarification milling. In general, the shear stress in a pavement first increases with depth to a peak value, and then decreases with depth. As the peak stress tends to arise at a depth ranging between 2 mm and 6 mm, the interface between the chip seal and underlying HMA pavement is commonly located below the critical zone before scarification milling. As mentioned earlier, scarification milling is normally used to remove a portion of the pavement within a depth of ¾″ and produce a surface with parallel ridges and valleys. Therefore, the thickness of the chip seal in the valleys will be reduced significantly after scarification milling, which moves the interface between the chip seal and underlying HMA pavement close to or into the critical zone of shear stress.

In addition, scarification milling may also cause some damage to the chip seal-HMA pavement interface. During the operation of scarification milling, the impact force from the rotating drum and cutters will be transferred through the chip seal to the interface, which may thereby affect the chip seal-HMA pavement interface negatively. In particular, the interface in an area with cracks in the underlying HMA pavement are more prone to delamination as shown in Figure 3.8(b). When moisture is present in the crack(s), delamination may develop more rapidly. It has been widely recognized that scarification milling would provide a surface more receptive to bonding to the new surface treatments such as micro-surfacing, ultra-bonding wearing course (UBWC), and HMA overlay. This, however, may not be true for installing HFSTs on chip sealed HMA pavements. In reality, all delamination distresses occurred in the HFSTs with surface preparation by scarification milling. Furthermore, scarification milling does not necessarily provide better interface bonding between the HFST and chip seal, compared to vacuum sweeping as illustrated in Figure 3.2.

3.3.4 Surface Wrinkling

Although slippage cracks may not occur associated with surface wrinkling, it affects not only the appearance of an HFST but also the ride quality of HFST. Undoubtedly, surface wrinkling may cause stress concentrations in the HFST under moving traffic loads, thereby increasing aggregate loss and affecting the durability of HFST. As shown in Table 3.3, surface wrinkling was observed at a total of eight HFST sites. Currently, it may be very difficult to make a firm conclusion about the probable cause(s). However, any factors that affect the lateral shear force and the strength of epoxy binder will affect the occurrence of surface wrinkling as surface wrinkling arises fundamentally due to the lateral and shear forces caused by moving traffic loads. When a vehicle is traveling on a horizontal curve,there is a centripetal force acting on the vehicle toward the center of the curve, which is supplied by the friction force between the tires and pavement surface and the gravity of vehicle (on a super-elevated curve). Therefore, the shear forces acting on the pavement surface by the side thrust of the vehicle tires increase as speed increases, compared to traveling on a straight road. Consequently, part of the HFST surface moves away laterally. This may be particularly true when heavy trucks are present.

Several observations can be made through careful inspection of Tables 3.2 and 3.3. First, the traffic

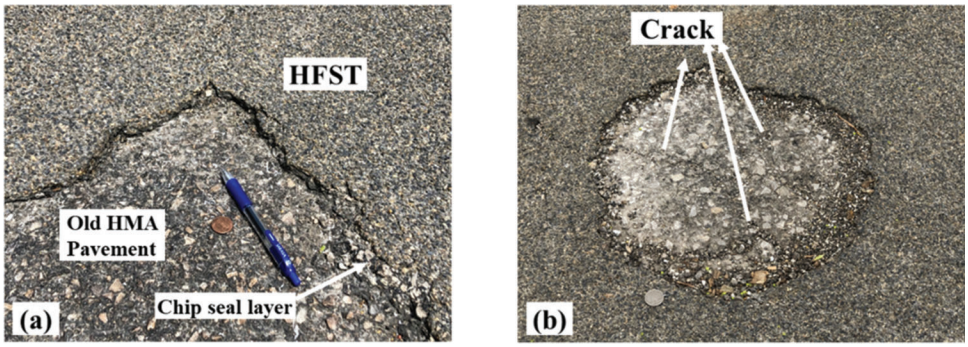

Figure 3.8 Photos of HFST surface delamination: (a) position of delamination and (b) cracks presented.

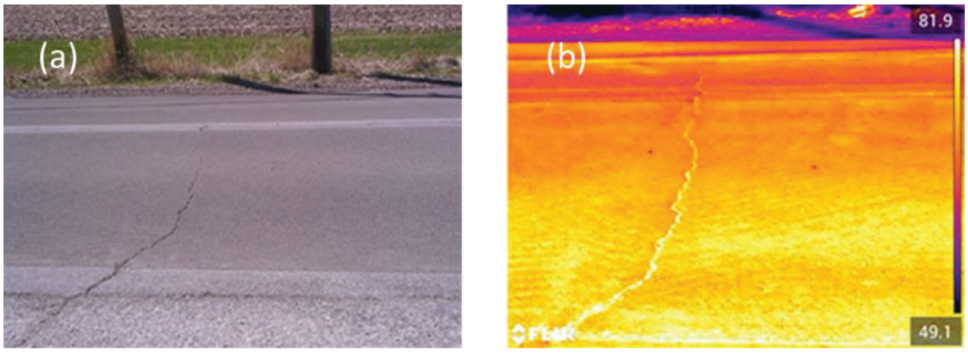

Figure 3.9 Surface wrinkling adjacent to crack: (a) digital image and (b) infrared image.

volumes are relatively high at the majority of these eight HFST. In particularly, the semi-truck traffic volumes are high at the HFST sites such as US-35a and US-24a. Therefore, the lateral forces induced by heavy trucks may be very large on newly installed HFSTs that normally have a coefficient of friction around 0.90. Second, four of these eight HFST sites, including SR-25, US-24a, SR-205a, and SR-205b, were installed at temperatures close to or below 60°F. As pointed out earlier, curing an epoxy binder system at low temperatures not only requires longer cure time, but also affects the mechanical properties of the epoxy binder such as its strength. Surface wrinkling tends to arise when the strength of the epoxy binder is low. Third, the AADT volumes are around 2,000 at the two HFST sites on SR-62. Nevertheless, the superelevation rates are very high at these two sites. The lateral force increases due to the gravity of vehicle as the superelevation increases. Finally, it is surprising that considerable crack distresses were encountered in the existing pavements at these eight sites. Presented in Figure 3.9 are two images that clearly show the surface wrinkling adjacent to a transverse crack in the HFST on SR-25. It is well known that an HMA pavement or overlay with low strength or bonding tends to experience slippage cracking induced due to large shear forces. This can also be extended to imply that there is a greater possibility for an HFST with a weak HMS substrate to experience surface wrinkling.

4. ANALYTICAL AND EXPERIMENTAL EVALUATION OF HFST-PAVEMENT INTERFACE BONDING AND REFLECTIVE CRACKING

4.1 Texture Characteristics of Pre-Treated Existing Pavement Surfaces

4.1.1 Pretreatment Method of Existing Pavement

The Indiana Department of Transportation (INDOT) primarily uses one of the three pretreatment techniques such as vacuum sweeping, shotblasting, and scarification milling for preparing existing pavements in terms of the existing surface condition before placing HFST. Vacuum sweeping is commonly used to remove dust, dirt, and debris on the existing pavement surface that is in good condition with a limited number of cracks. Shotblasting is utilized to remove the excessive asphalt binder, curing compounds, oil, and other contaminants on the surface of a newly constructed HMA pavement less than 30 days. Scarification milling is commonly used for existing pavements with distresses such as cracking, raveling, rutting, and bleeding. Although scarification milling is designated to produce a finished surface consisting of parallel ridges and valleys with a cutting depth of up to ¾″ and recommended as a standard practice for HMA overlay (INDOT, 2019), it is currently used as an expedient

solution to eliminate the possible effects of chip seal on HFST by INDOT districts.

Pretreatment is applied to ensure that HFST can be fully bonded onto the surface of existing pavement and reduce the possible effects of existing pavements. However, the pretreatment, especially shotblasting or scarification milling, alters the texture (or topography) of existing pavement surface. As shown in Figure 4.1 are the surface close-ups of two existing pavements, respectively, before and after shotblasting and scarification milling. After shotblasting, the existing pavement surface became free of excessive asphalt binder and exhibited an exposed aggregate finish. After scarification milling, the existing pavement surface became much rougher. To the authors' knowledge, a change to the texture of existing pavement surface will change the aspects of HFST-pavement interface bonding and the interlaminar stresses, and therefore affect the durability of HFST. The characteristics of pavement surface texture should be included in the analytical and experimental evaluation of the durability of HFST.

4.1.2 Surface Texture Characteristics after Pretreatment

There are two categories of texture, including macro- and micro-texture (Permanent International Association of Road Congress, 1987). The former can be readily measured (ASTM, 2019a; ASTM, 2019b), the latter is beyond observation with the naked eye. In the context of pavement structural responses, the focus is on the macro-texture that is characterized with the mean profile depth (MPD) (ASTM, 2019c). Table 4.1 presents the MPD values measured using a laser scanner before and after pretreatment for four pavements, respectively. During testing, the laser scanner was configurated to produce ten texture profiles over an area of 4.3″ × 2.8″, yielding an average MPD for the area scanned. Because a pretreatment with vacuum sweeping is not to retexture the pavement surface, the

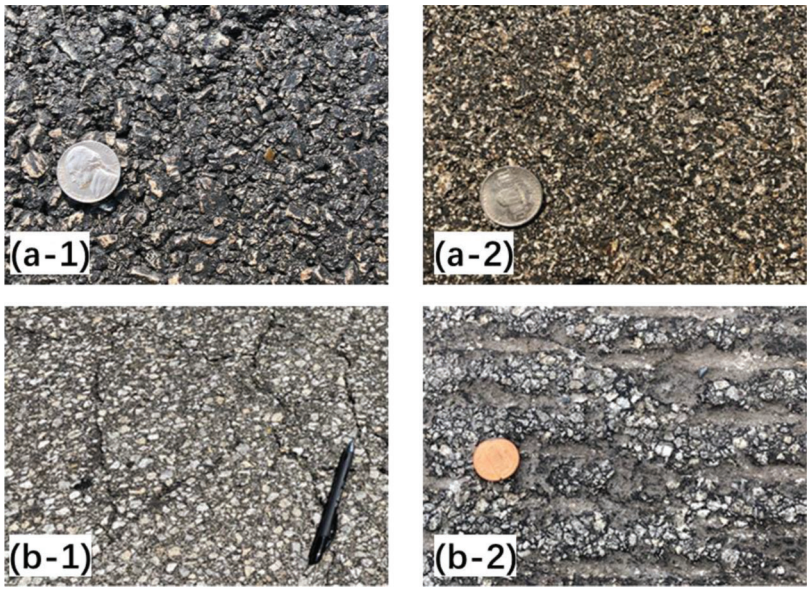

Figure 4.1 Surface close-ups before and after treatment: (a) shotblasting before (left) and after (right) and (b) scarification milling before (left) and after (right).

TABLE 4.1
Summaries of existing pavement and HFST conditions and surface frictional characteristics

Road	Existing Pavement	Pretreatment	MPD[1] (mm)			Coefficient of Friction	
			Existing Pavement		HFST	Existing Pavement	HFST
			Before	After			
US-35	Chip seal	Vacuum sweeping	–	0.530	1.897	0.454	0.820
SR-32	New HMA	Shotblasting	0.509	0.612	2.044	0.459	0.789
SR-446	Chip seal	Scarification milling	0.334	1.474	1.803	0.204	0.857
SR-205	Chip seal	Scarification milling	0.417	1.516	1.859	0.235	0.814

[1]Average of the MPDs from ten texture profiles measured using a laser scanner.

MPD values were assumed to be the same before and after vacuum sweeping. The MPD increased by about 20% after shotblasting and by up to 263% after scarification milling. No trend was found between the HFST surface MPD and the method of pretreatment. This implies that the HFST surface MPD is independent of the pretreatment of existing pavement surface. Scarification milling and shotblasting do not necessarily increase the MPD of HFST. Figure 4.2 shows the macro-texture profiles measured on three pavement surfaces prepared with vacuum sweeping, shotblasting, and scarification milling, respectively. These three surface macro-texture profiles are dramatically different from each other. The macro-texture profile with vacuum sweeping is the smoothest one with narrow and shallow valleys. As shown in the middle of Figure 4.2, shotblasting yielded wider and deeper valleys. Scarification milling retextured the pavement surface dramatically, resulting a significantly different macro-texture profile with largest valleys and peaks. It was expected that the geometric features of a profile, such as shape, depth, and spacing, might affect the inter-laminar stresses at the HFST-pavement interface, resulting in stress concentrations that may affect the durability of HFST.

4.2 FEA Evaluation of Mechanical Behaviors of HFST-Pavement Interface Bonding

4.2.1 Finite Element Model and Parameters

To consider the effects of the profile geometric features, a two-dimension (2D) finite element (FE) model was adopted in the finite element analysis (FEA) of HFST-pavement systems. To represent a true surface topography, the ten 4″ long profiles measured with the laser scanner were combined together to yield a 40″ long surface profile that was used in the FE model. The 2D FE model consisted basically of two layers, including both HMA and HFST. The structural layers underneath the HMA layer, such as base, subbase, subgrade, were simplified as a Winkler foundation characterized with the foundation reaction modulus. The thicknesses of HMA and HFST layers in the FE model were determined from pavement cores and the average thicknesses are 11.5″ and 1/8″, respectively. Consequently, the HFST-pavement FE model was 40″ long and 11.7″ thick.

Figure 4.3(a) demonstrates the meshing in the 2D FE model. The 3-node linear plane stress triangle (CPS3) finite elements with a mesh size of 0.04″ were assigned

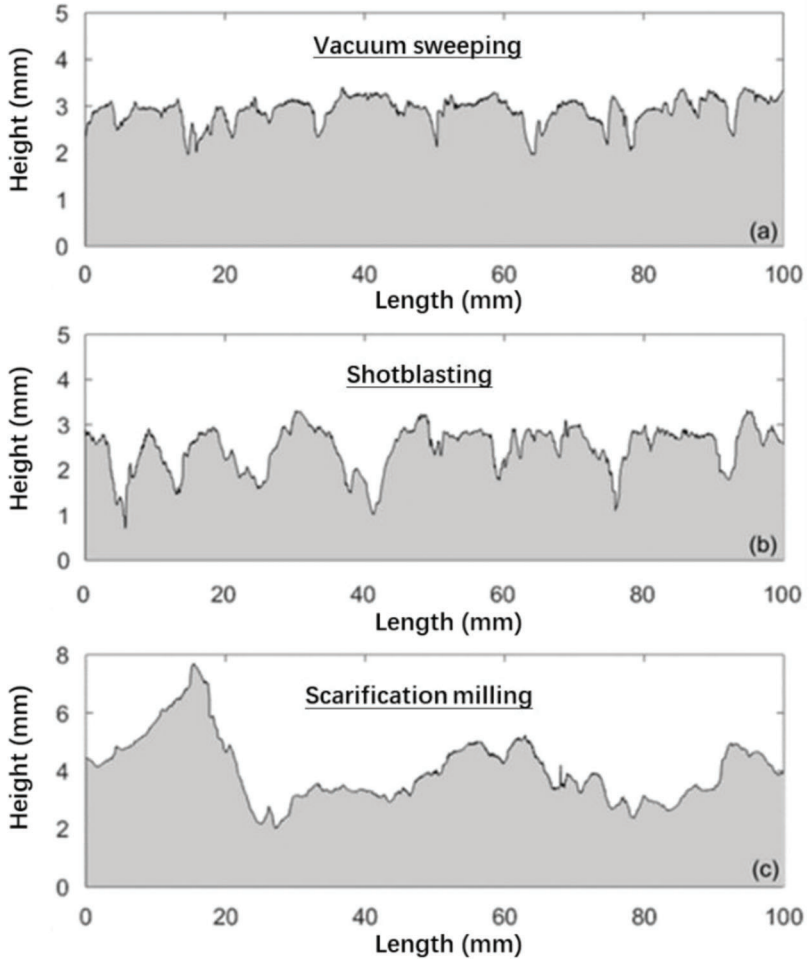

Figure 4.2 Macro-texture profiles on three pavement surfaces after different pretreatments.

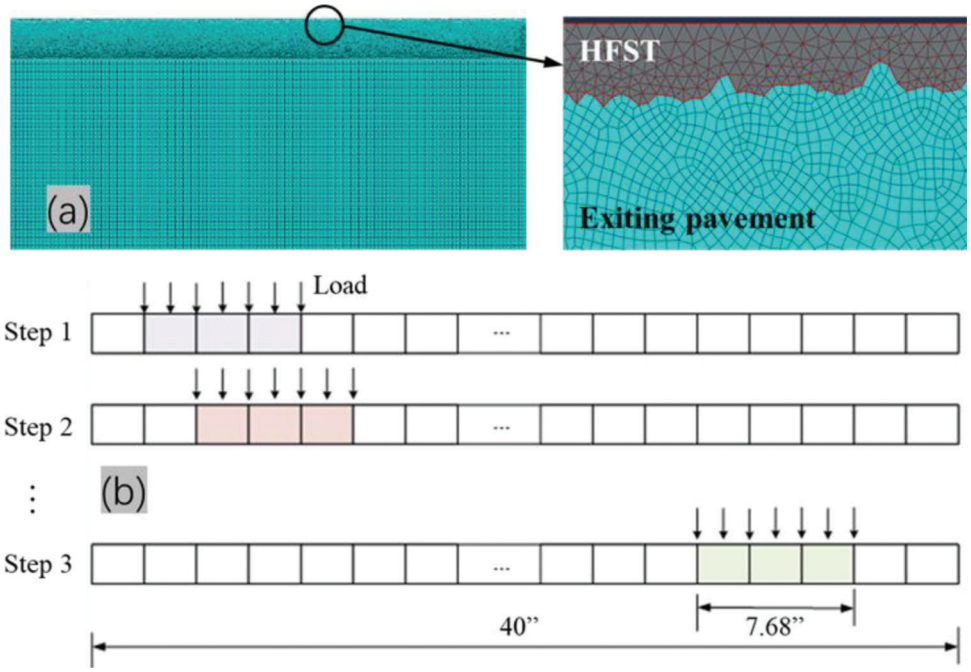

Figure 4.3 The FE model: (a) meshing and (b) moving load and steps.

to the HFST layer. The 4-node bilinear plane stress quadrilateral finite elements with reduced integration (CPS4R) were assigned to the HMA layer. Two mesh sizes were adopted in meshing the HMA layer, i.e., 0.08″ for the top 2″ area and 0.2″ for the rest part. Fully bonded contact was applied at the HFST-HMA interface. The normal displacements were constrained at two sides of the FE model. A standard single axle load of 18-kip was applied with a tire pressure of 104 psi. Because the applied load was considered as a dynamic load, the contact area would move forward one third of the footprint for each increment step as illustrated in Figure 4.3(b). A total number of 16 steps were applied in the FE model. The length of the tire-pavement contact area (i.e., footprint) was calculated to be 7.68″ with Equations (4.1) and (4.2):

$$A = \pi(0.3L)^2 + 0.4L \times 0.6L = 0.5227L^2 \qquad \text{(Eq. 4.1)}$$

$$a = 0.8712L; b = 0.6L \qquad \text{(Eq. 4.2)}$$

where A is the contact area of tire, in^2; L is the contact length of tire, mm; a is the contact length of the tire footprint, in.; b is the contact width of the tire footprint, in.

Vertical load and braking force were applied simultaneously onto the HFST surface. The braking force was equal to the vertical load multiplied by the coefficient of friction. The coefficients of friction before and after installing HFST, as shown in Table 4.1, were determined in accordance with the ASTM E274 method (2015d). It is shown that the coefficient of friction increased dramatically after placing HFST. The braking force of 86 psi was calculated from the average coefficient of friction (i.e., 0.82). Table 4.2 presents the

TABLE 4.2
Elastic moduli of pavement layers

Layers	Modulus (ksi)	Standard Deviation	Poisson's Ratio
HFST	1,452[1]	–	0.29
HMA	585	212	0.3
Subgrade	35 (73.9 MN/m^3)	5.9	0.35

[1]Measured at 70°F and 10 Hz loading frequency.

properties of HFST-HMA system. The layer moduli of the existing HMA pavements were determined with falling weight deflection (FWD) testing. The dynamic modulus and Poisson's ratio of HFST were measured with laboratory testing (Wei et al., 2020). Five different surface profiles, including four from the actual pavements and one perfectly smooth surface (i.e., MPD = 0) as a reference for comparison, were included in the FE model. Consequently, a total of 16 FE models were developed in the FEA prediction.

4.2.2 Simulation Results and Analysis

Presented in Figure 4.4 are the interlaminar stresses with different pretreatments when the vehicle load was applied at the center of the FE model. The maximum interlaminar stress in the reference model is equal to the braking force of 86 psi. When the surface texture was included in the FE model, however, noticeable stress concentrations occurred, depending on the texture characteristics of the pre-treated surfaces. The above confirms that comparing the interlaminar stresses is a reasonable way to determine the effect of pretreatment. The stress concentrations occurred along the entire

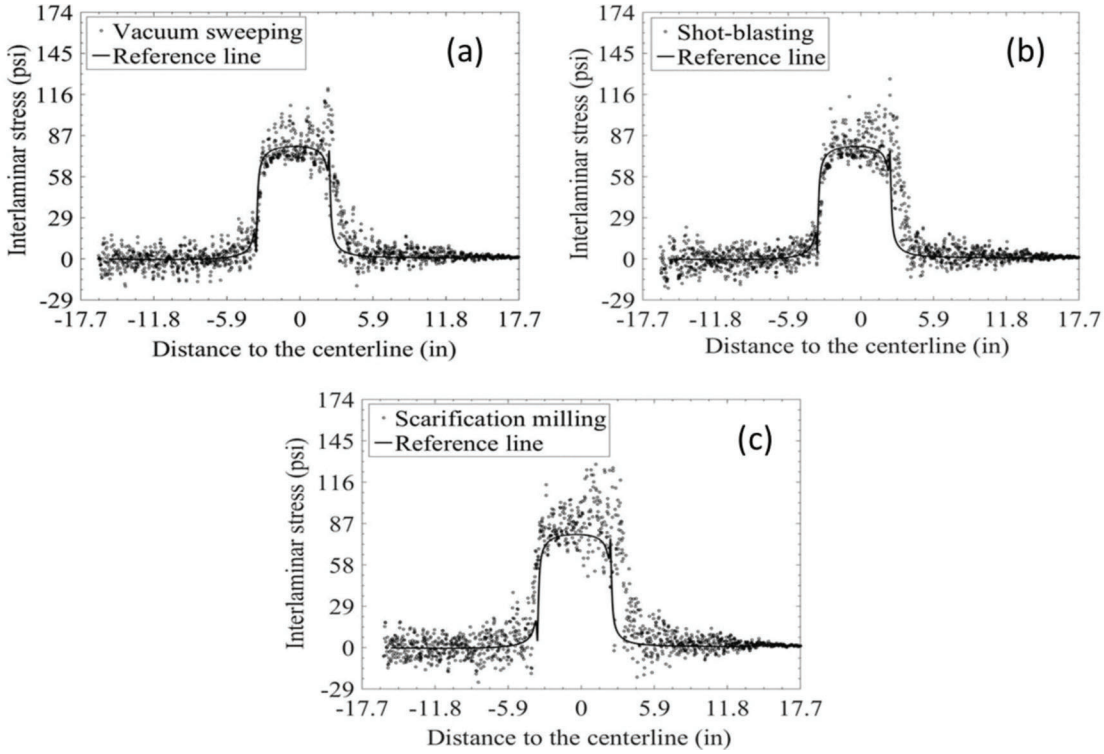

Figure 4.4 Interlaminar stress with different surface pretreatments: (a) no pretreatment, (b) shotblasting, and (c) scarification milling.

TABLE 4.3
The percentages of nodes with interlaminar stresses greater than 86 psi

Surface Pretreatments	Profile 1	Profile 2	Profile 3	Profile 4	Profile 5	Average
Vacuum sweeping	3.92%	3.75%	3.00%	3.87%	4.30%	3.77%
Shotblasting	5.09%	3.69%	5.08%	5.38%	5.16%	4.88%
Scarification milling	6.07%	6.58%	6.44%	6.08%	6.44%	6.32%

interface and the most critical region was located at the leading edge of the footprint. The maximum interlaminar stresses were 102 psi, 126 psi, and 148 psi with vacuum sweeping, shotblasting, and scarification milling, respectively. The maximum stress with scarification milling was 22.9% greater than that with vacuum sweeping and 17.3% greater than that with shotblasting. Evidently, scarification milling will result in a significant increase of interlaminar stress. This indicates that scarification milling may cause harmful effects on the durability of HFST.

However, the interlaminar stress distribution with the load applied at the center of the FE model may not represent the interlaminar stress distributions with the load applied at other locations because the surface textures vary randomly across the entire interface. To fully understand the interlaminar stresses with the load applied at other locations in the FE model, the authors examined the simulation results at the increment steps of 1, 4, 7, 10, 13, and 16 by moving the tire load to cover the most area of the FE model. For each type of pretreatment, calculations were performed in terms of five measured surface texture samples, respectively. Summarized in Table 4.3 are the percentages of the interface nodes with interlaminar stresses greater than 86 psi in all cases (i.e., combinations of pretreatment and texture profile). The average percentages are 3.77%, 4.88%, and 6.32% for vacuum sweeping, shotblasting, and scarification milling, respectively. Evidently, vacuum sweeping resulted in the smallest region of stress concentration, while scarification milling produced the largest region of stress concentration along the HFST-pavement interface.

To further examine the percentages of high interlaminar stresses with different pretreatments, Figure 4.5 shows the percentages of interlaminar stresses in four categories, i.e., greater than 100 psi, 115 psi, 129 psi, and 144 psi, respectively. The percentages of high stresses with scarification milling were always greater than those with either vacuum sweeping or shotblasting in all four categories. However, the percentages of high stresses with shotblasting were higher than those with vacuum sweeping in all categories except for the category greater than 144 psi. In the category greater than 144 psi, the percentages of high stresses with vacuum sweeping were

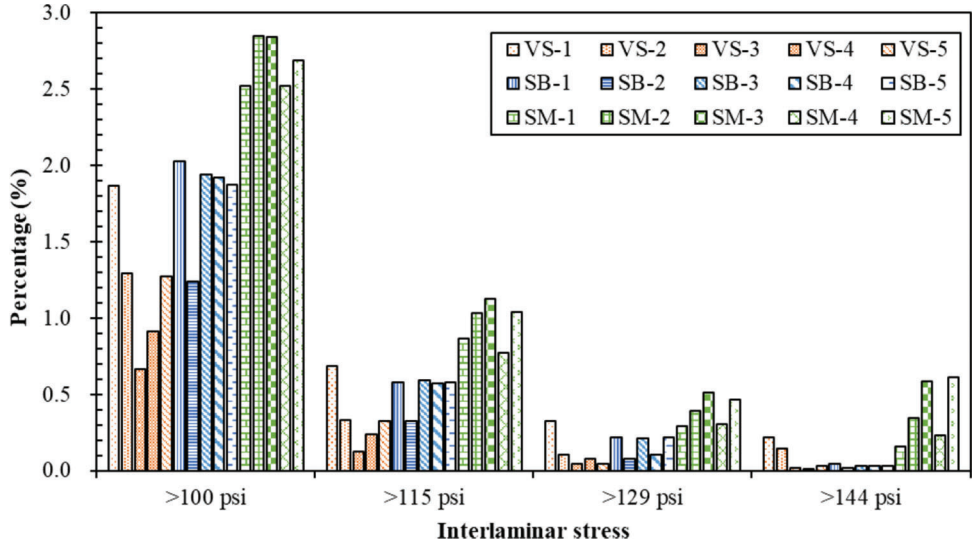

Figure 4.5 Percentage of interlaminar stress higher than threshold values.

greater than those with shotblasting, depending on the texture profiles utilized. This implies that shotblasting may remove the spikes in the existing pavement surface. Overall, the results of FEA prediction demonstrated that scarification milling may result in the greatest interlaminar stress, largest region of stress concentration, and highest percentage of high interlaminar stress. This suggests that scarification milling definitely cause harmful effects on the durability of HFST. Also, vacuum sweeping may result in better durability for HFST than shotblasting in the context of interlaminar stresses at the HFST-pavement interface.

4.3 Experimental Evaluation of Mechanical Behaviors of HFST-Pavement Interface Bonding

4.3.1 Experiment Design

The authors first developed a Material Test System (MTS) experimental protocol based on the concept of an inclined shear test machine reported elsewhere (Tozzo et al., 2014). This protocol utilizes both a loading head and a loading base as shown in Figure 4.6(a) and 4.6(b) to simulate a braking tire that exerts both vertical and horizontal forces onto the surface of HFST. The vertical force is equal to the weight of vehicle. The horizontal force is equal to the friction force, i.e., the vehicle weight multiplied by the coefficient of friction. The average coefficient of friction (i.e., 0.82) calculated from Table 4.1 was used to determine the magnitude of the cyclic load. The loading head is a 4″ wide, right-angled triangular prism made of aluminum alloy. The loading base consists of two triangular bearing plates and a rectangular base plate. Both the angle of the loading head and the slope of the triangular bearing plate are 39° calculated from Equation 4.3:

$$\tan\theta = f \qquad \text{(Eq. 4.3)}$$

where θ is the slope of the bearing plate, and f is the coefficient of friction.

The temperature was maintained at 77°F during testing. The specimens were 16″ × 4″ × 2.5″ HMA beams overlaid with HFST. A sinusoidal cyclic load of 10 Hz frequency with a contact pressure of 104 psi perpendicular to the HFST-HMA interface was applied to the specimen through the loading head. The loads parallel and perpendicular to the HFST surface, respectively, were 1,628 pounds and 1,335 pounds calculated from the contact area of 4″ × 4″ between the loading head and HFST. Consequently, the vertical actuator was configured to apply a total force of 2,104 pounds. The tests were terminated after a specific number of load cycles in terms of the total number of equivalent single axle loads (ESALs) over a period of 5 years. For simplicity, the average number of ESALs (i.e., 580,415) at the four sites shown in Table 4.1 was used. It took roughly 968 minutes for the test of each specimen. A total of six HFST-pavement specimens were tested, of which, three were pretreated with shotblasting and three were pretreated with scarification milling. Vacuum sweeping was not considered in the laboratory evaluation because the HFST-pavement specimens were freshly produced. After cyclic loading, pull-off tests were carried out in accordance with ASTM C1583/C1583M-13 (2013) at three positions. To fully understand the effects of loading on the bonding strength at the HFST-pavement interface, Positions 1, 2 and 3, respectively, were located at the center of the unloaded area, on the boundary of the loaded area, and at the center of loading area, as shown in Figure 4.6(c).

4.3.2 Test Results and Analysis

Presented at the top of Figure 4.7 are the failure modes observed in the pull-off tests. The substrate failure occurred commonly in the HMA substrate near the HFST-pavement interface. The adhesive failure that

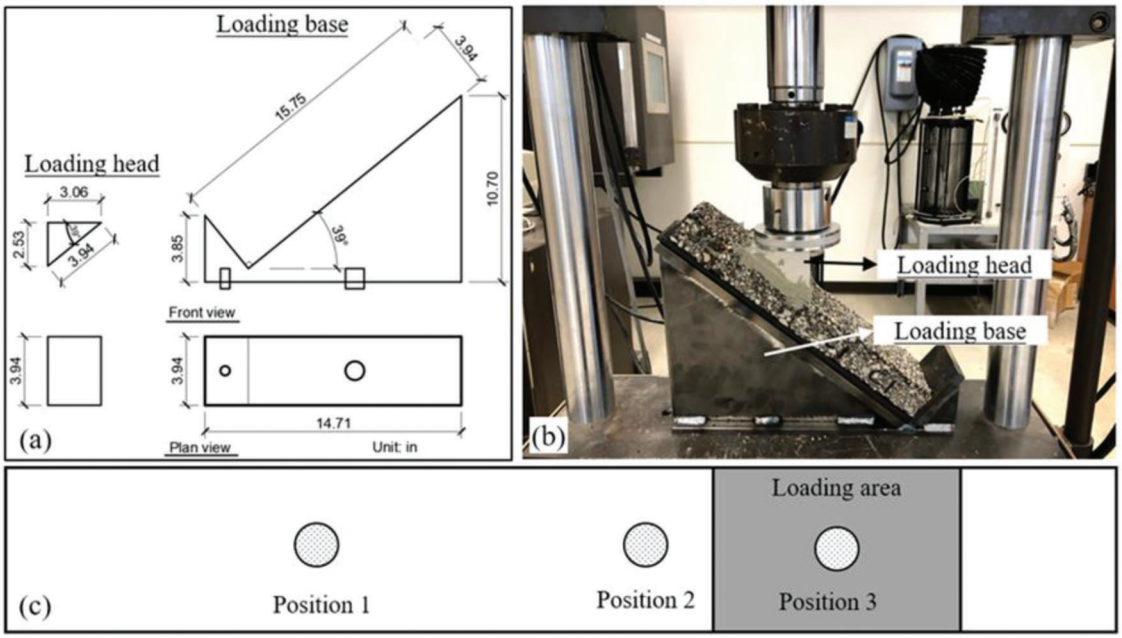

Figure 4.6 Test setup with special loading head and base.

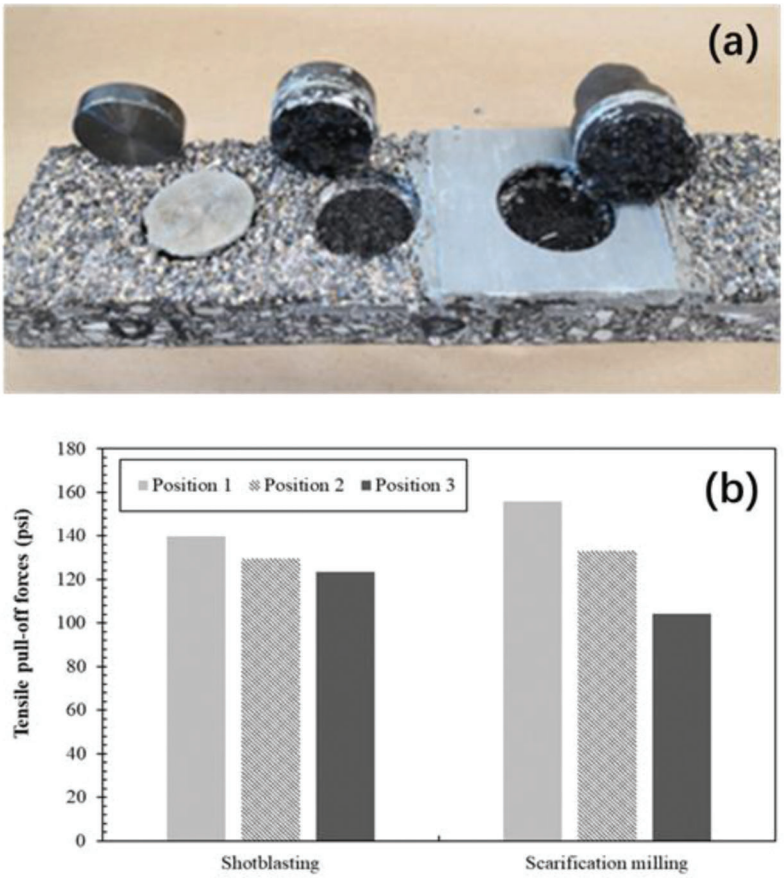

Figure 4.7 Failure modes and results of pull-off tests: (a) test positions and failure modes and (b) average tensile pull-off forces by pretreatment.

is usually considered as an invalid test commonly arose at the binder-dolly interface. The above agrees well with the finding from field HFST pull-off tests elsewhere (Li et al., 2019), which states the interface bonding strength was greater than the tensile strength of HMA substrate. Presented at the bottom of Figure 4.7 are the pull-off forces for substrate failures. The pull-off forces in the loaded areas were less than those in the unloaded areas. The unloaded areas experienced the greatest pull-off forces. This indicates the possible impacts of cyclic loading, regardless of the type of pretreatment.

In addition, noticeable differences arose between the pull-off forces with different pretreatments, particularly at Position 1 (unloaded area) and Position 3 (loaded area). At Position 1, the average pull-off force with scarification milling was 11.3% greater than that with shotblasting. At Position 3, the average pull-off force with scarification milling was roughly 18.6% less than that with shotblasting. The pull-off force decreased from 139 psi at Position 1 to 123 psi at Position 3 for shotblasting, and from 155 psi at Position 1 to 104 psi at Position 3 for scarification milling. The former indicates a 11.8% reduction, the latter indicates a 33.1% reduction. Evidently, scarification milling will cause harmful effects on the durability of HFST-pavement system, which agrees well with the conclusion achieved from the FEA simulation presented previously.

4.4 Field Verification

4.4.1 Site Conditions

To verify the results from both the FEA simulation and laboratory evaluation, field verification was conducted at the four HFST sites (see Table 4.1). Table 4.4 further provides the detailed information about the site and existing pavement conditions, including type of existing pavement, curve geometrics, and number of transverse cracks. All roads at these four sites were two-lane highways. The existing pavements were chip seals at all sites except for SR-32 that was newly placed 1.5″ HMA mill and fill. Low severity transverse cracking was the most prevalent distress in the existing pavements at all sites except for SR-32. Some edge and longitudinal cracks were occasionally observed at the site on US-35a. No obvious problems were observed in both surface drainage and subsurface drainage from visual inspection and ground penetration radar (GPR) testing. The existing pavement pretreatment methods and resultant MPDs can be found in Table 4.1.

HFSTs at these four sites were placed in 2018. Before placing HFSTs, no crack seal was applied to both transverse and longitudinal cracks. It was believed that those cracks in the existing pavement surfaces would be sealed by the epoxy binder during HFST placement. Patching was used only to repair an area of moderate severity block cracks in the HMA shoulder on US-35a. The application rates recommended by the contractor were 26–32 square feet per gallon for epoxy binder and 14–20 pounds per square yard for calcined bauxite aggregate. As shown in Table 4.4, more epoxy binder was applied at HFST sites with the existing pavements pretreated with scarification milling (i.e., SR-446 and SR-205b) than with other pretreatments, particularly vacuum sweeping (i.e., US-35a), approximately an increase of 10% in quantity.

4.4.2 Observations and Results

Field post-construction inspections were carried out in mid-April 2019 when the four HFSTs had experienced an entire winter season and undergone the possible harmful effects of freeze-thaw cycles and snowplows. Transverse cracking and delamination were the two predominant types of HFST failure observed at these four sites (see Table 4.4). The crack rate was calculated as the ratio of the number of cracks in the existing pavement before placing HFST to the number of cracks in HFST. Approximately, 94% of the transverse cracks in the existing pavements had reflected through the HFSTs at the three sites on US-35a, SR-446, and SR-205b, respectively. Notice that at the site on SR-32, the reflective cracking in HFST occurred due mainly to the cracks in the existing pavement beneath the new HMA overlay. It can be concluded that the transverse cracks in the existing pavement will reflect through HFST, regardless of the type of pretreatment, and overlay cannot eliminate reflective cracking through HFST.

Delamination was found only at the sites on both SR-446 and SR-205b where the existing pavements were pretreated with scarification milling. No delamination

TABLE 4.4
Summaries of site and existing pavement conditions and distresses in HFST

	Site Condition				Material Application Rate		Distress in HFST		
Site	Lengths (ft)	Radius (ft)	Traffic[1]	Transverse Cracks (No.)	Epoxy Resin (1 gallon/sq.ft.)	Calcined Bauxite (bs/sq.yd.)	Transverse Cracks (No.)	Crack Ratio (%)	Debonding
US-35a	971	1,322	2886/20	38	27.21	19.41	36	94.7%	No
SR-32	259	118	9679/5	0	25.07	15.38	15	NA	No
SR-446	709	384	1705/17	16	24.44	16.52	15	93.8%	Yes
SR-205b	830	591	3641/4	78	25.02	19.40	74	94.9%	Yes

[1]Traffic AADT/truck %.

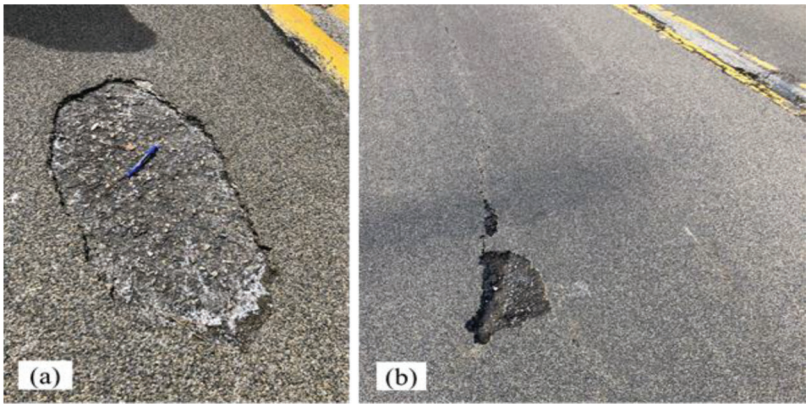

Figure 4.8 Typical delamination failures in HFSTs on SR-446 and SR-205b.

TABLE 4.5
Interface bonding strengths

Road	Surface Pretreatments	Interface Bonding Strength (psi)			
		Specimen 1	Specimen 2	Specimen 3	Average
US-35a	Outside HFST	29.0	36.3	–	31.9
US-35a	Vacuum sweeping	30.5	29.0	24.7	27.6
SR-32	Shotblasting	82.7	85.6	71.1	79.8
SR-446	Scarification milling	36.3	56.6	63.8	52.2
SR-205b	Scarification milling	63.8	63.8	63.8	63.8

was observed at the sites on US-35a and SR-32. The delamination occurred commonly at the interface between chip seal and underlying HMA pavement, instead of the interface between HFST and chip seal (see Figure 4.8). As stated previously, scarification milling is designated to remove a portion of the pavement within a depth of ¾″ and produce a surface with parallel ridges and valleys. Consequently, the thickness of the chip seal in the valleys will be reduced significantly. In addition, scarification milling may also cause some damage to the chip seal-HMA pavement interface due to the impact from the rotating drum and cutters.

Pavement cores were taken in the HFSTs to determine the bonding (i.e., pull-off) strength between HFST and the existing pavement. Additionally, two cores were taken in the existing chip seal near the boundary of HFST on US-35a to determine the bonding strength between the chip seal and the underlying HMA pavement. All pull-off tests on the cores were conducted in the laboratory at 77°F to eliminate the possible effects of temperature. Table 4.5 presents the average bonding strengths for all cores. The cores from SR-32 exhibited the highest bonding strength and the cores from US-35a exhibited the lowest bonding strength. Careful inspection of the failed core specimens revealed that all failures occurred in the HMA layers underneath chip seals, regardless of the method of pretreatment. Notice that the existing pavement on US-35a experienced more surface distresses than those on the other roads. Nevertheless, the existing pavement on SR-32 was newly placed HMA overlay. Therefore, the bonding strength might actually represent the tensile strength of the existing HMA pavement rather than the bonding strength at the HFST-pavement interface. There is no evidence that vacuum sweeping is not capable of creating durable interface bonding for HFST.

4.5 Experimental Evaluation of Reflective Cracking

4.5.1 Laboratory Test and Results

Reflective cracking is one of the main distresses in HFST, which affects the HFST's durability. Laboratory overlay test was used to investigate the causes and development of reflective cracking in HFST. Details about the overlay test can be found elsewhere (TxDOT, 2008). Figure 4.9 is the setup of the laboratory overlay test. The specimen was glued to the metal plates using epoxy binder. The test temperature was 77 ± 1.0°F. The specimen was placed in a temperature chamber for a minimum of one hour before testing. Because a 93% reduction of the maximum load did not occur for all specimens during the tests, load conditionings were terminated after 1,000 loading cycles was reached. In addition, two parameters, including the maximum peak load (MPL) and maximum load reduction (MLR), were calculated at the end of test for each specimen. MPL has been used to evaluate the tensile strength of the specimens. The higher the MPL, the stiffer the specimen. The MLR has been used to assess the anti-reflective cracking ability. The lower the MLR, the higher the cracking resistance. To the authors' knowledge, for two

Figure 4.9 Setup of laboratory overlay test.

materials with the same MPL, the one having less MLR tends to have higher cracking resistance. For two materials with the same MLR, however, the one having larger MPL tends to have higher cracking resistance.

Presented at the top of Figure 4.10 are both the MPL and MLR of epoxy-bauxite mortar and HMA specimens, respectively. It is shown that there is little difference in both the MPL and MLR between these two materials. The average MPL and MLR, respectively, are 407 pounds and 31.6% for epoxy-bauxite mortar. For the HMA specimen, its MPL is slightly lower and its MLR is slightly higher. Presented at the bottom of Figure 4.10 are the results from the laboratory overlay tests conducted on the HFST-HMA specimens made from field HFST cores. Each HFST-HMA specimen consisted of both an HFST layer and an HMA layer. It is shown that the average MPL is 661 pounds, significantly higher than that of both the epoxy-bauxite mortar and HMA specimens, which indicates that the HFST-pavement specimens were much stiffer. The average MLR of HFST-HMA is around 76.1%, which is expected.

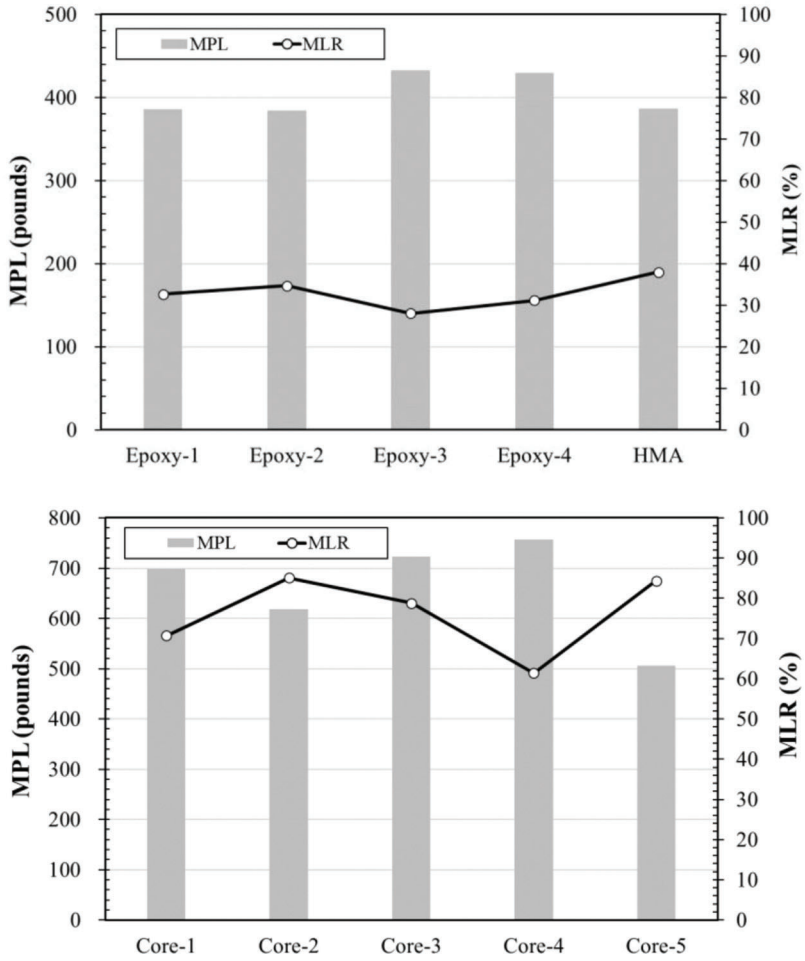

Figure 4.10 MPL and MLR for epoxy-bauxite mortar, HMA, and HFST-HMA.

4.5.2 Effects of Crack Aspects

Laboratory overlay tests were also performed to further examine the possible effects of crack aspects in the existing pavement before placing HFST, including crack location, crack direction, crack length, and crack treatment. To accomplish this, four types of specimens, each with two replicate specimens, were specially made as shown in Figure 4.11. Specimens Sp_A1 and Sp_A2, respectively, consisted of an HFST layer placed on an HMA beam without any cracks. Specimens Sp_B1 and Sp_B2, respectively, consisted of an HFST layer placed on an HMA beam with a 1″ (25.4 mm) long transverse edge crack occurred at the mid-point along the beam length. Specimens Sp_C1 and Sp_C2, respectively, consisted of an HFST layer placed on an HMA beam with a 2″ (50.8 mm) long transverse edge crack occurred at the mid-point along the beam length. Specimens Sp_C1 and Sp_C2, respectively, consisted of an HFST layer placed on an HMA beam with a 2″ (50.8 mm) long longitudinal crack occurred in the middle of the HMA beam. All cracks were surface cracks in the HMA beams.

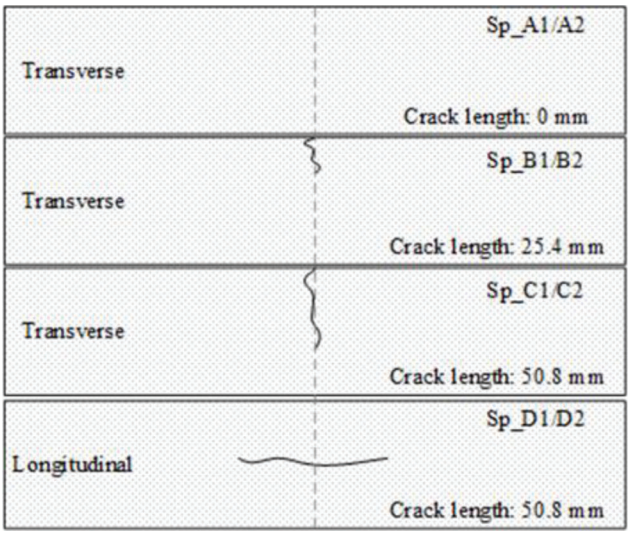

Figure 4.11 Specimens with different crack aspects in underlying HMA beams.

Summarized in Table 4.6 are the results of both MPL and MLR from the laboratory overlay tests for all four types of specimens. Three observations can be made with careful inspection of the MPL and MLR. First, the specimens with transverse cracks exhibited lower MPLs than those without cracks and the MPL decreased as the crack length increased. This is because the overlay test utilizes a displacement control mode, resulting in all specimens subject to the same displacement and the HMA beam became weaker with a longer crack. Nevertheless, the differences between the MLRs are so small as to be unimportant. Second, there are negligible differences in the MPLs between the specimens with transverse and longitudinal cracks, respectively. However, the latter demonstrated much higher MLRs. Third, the specimens with longitudinal cracks demonstrated higher MPLs and MLRs than those with transverse cracks, but it is difficult to say which may affect HFST more significantly. A firm conclusion is that cracks in the existing pavements will affect the durability of HFST.

Figure 4.12 presents the results of MPL and MLR from the laboratory overlay tests on HFST-HMA specimens with cracks in the underlying HMA beam, which were sealed with hot asphalt binder and epoxy binder, respectively. It is shown that the specimens with cracks sealed with epoxy binder exhibited much higher MPL and MLR than those sealed with hot asphalt. As illustrated in Chapter 3, reflective cracking was caused mainly by seasonal temperature variations due to the incompatible thermal expansion between HFST and HMA, rather than traffic loads. A higher MLR may indicate that the thermal incompatibility between epoxy binder and HMA will affect the reflective cracking more significantly. Therefore, asphalt binder may outperform epoxy binder for sealing the cracks in the existing pavements before placing HFST.

TABLE 4.6
Summary of overlay test results

Specimen	Crack Direction	Crack Length (in)	Maximum Peak Load (MPL) (pounds)	Maximum Load Reduction (MLR) (%)
Sp_A1	N.A.	0	470	71.6
Sp_A2			378	66.2
Sp_B1	Transverse	1.0	448	74.1
Sp_B2			345	61.1
Sp_C1		2.0	370	65.1
Sp_C2			413	65.9
Sp_D1	Longitudinal	2.0	444	77.9
Sp_D2			399	89.7

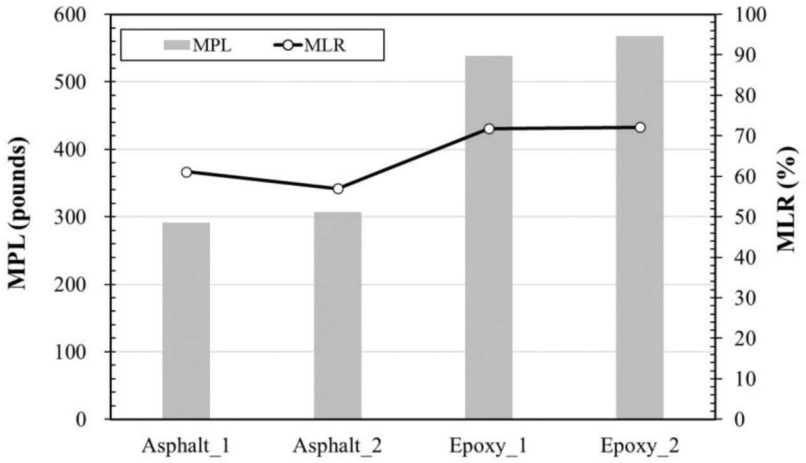

Figure 4.12 MPL and MLR for cracks treated with hot asphalt and epoxy binder.

5. DETERMINATION OF FRICTION PERFORMANCE METRICS

5.1 Fundamentals of Vehicle-Pavement Dynamics

5.1.1 Vehicle Dynamics on Level Ground

Newton's second law states that the acceleration of a body is directly proportional to the applied net force in the direction of the net force, but inversely proportional to the mass of the body, and can be expressed as follows (Kleppner & Kolenkow, 1973):

$$F = ma \qquad \text{(Eq. 5.1)}$$

where F = net force; m = mass of the body; and a = acceleration of the body.

As a vehicle wheel is skidding over a flat, straight ground as illustrated in Figure 5.1, substituting the external forces into Equation 5.1 yields the following equation:

$$F_t - F_f = ma \qquad \text{(Eq. 5.2)}$$

where F_t = tractive force; and F_f = friction force expressed as follows:

$$F_f = f \cdot F_{wy} \qquad \text{(Eq. 5.3)}$$

where f = coefficient of friction; and $F_{wy} = W = mg$, i.e., the weight of the wheel (g = 32.17 ft/s^2, i.e., the gravitational acceleration).

Notice that the wheel is skidding at a constant speed, i.e., $a = 0$, Equation 5.2 can then be rewritten as follows:

$$f = \frac{F_t}{F_{wy}} = \frac{F_t}{mg} \qquad \text{(Eq. 5.4)}$$

5.1.2 Vehicle Dynamics on Straight Grades

As a vehicle wheel is skidding over a straight grade, the external forces include F_t, F_f, F_{wy}, and F_{wx} as shown in Figure 5.2. F_t and F_f, respectively, are the tractive force and friction force as defined in Equation 5.2. F_{wy} and F_{wx}, respectively, can be determined as follows:

$$F_{wy} = mg \cdot \cos\theta \qquad \text{(Eq. 5.5)}$$

$$F_{wx} = mg \cdot \sin\theta \qquad \text{(Eq. 5.6)}$$

where θ = slope of the grade; and all other variables are as defined earlier.

Substituting the external forces and $a = 0$ into Equation 5.2 yields the following equations:

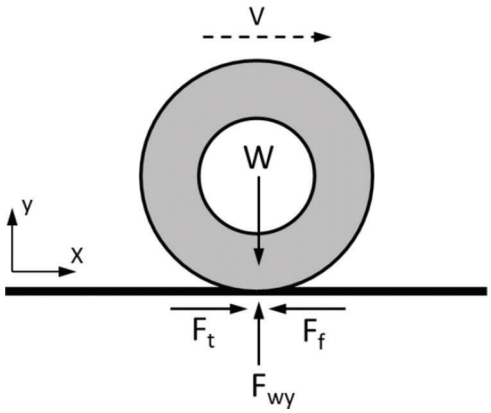

Figure 5.1 Forces acting on a wheel on level, straight ground.

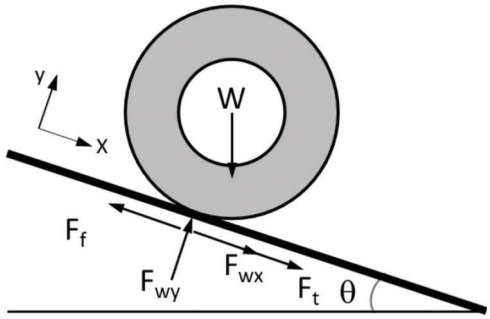

Figure 5.2 Forces acting on a wheel on straight grade.

Uphill:

$$F_{tU} = mgf \cdot cos\theta + mg \cdot sin\theta \qquad \text{(Eq. 5.7)}$$

Downhill:

$$F_{tD} = mgf \cdot cos\theta - mg \cdot sin\theta \qquad \text{(Eq. 5.8)}$$

where F_{tU}, F_{tD} = uphill or downhill tractive force.

Taking the average of the uphill and downhill tractive forces gives:

$$F_{tA} = \frac{F_{tU} + F_{tD}}{2} = mgf \cdot cos\theta \qquad \text{(Eq. 5.9)}$$

where F_{tA} = average of the uphill or downhill tractive forces.

Since the maximum grades are very small, i.e., $tan\theta$ = 17%, 12%, 8%, and 6% for local, collector, arterial, and interstate, respectively (INDOT, 2019), cos $\theta \approx 1$. The average tractive force can be approximated as the tractive force on level, straight ground. The coefficient of friction, i.e., f, can be expressed as follows:

$$f \approx \frac{F_{tA}}{mg} \qquad \text{(Eq. 5.10)}$$

5.1.3 Vehicle Dynamics on Horizontal Curves

As a vehicle wheel is skidding over a horizontal curve on level ground as shown in Figure 5.3, the external forces acting on the wheel may be explained using a cornering model and expressed as follows:

$$F_{t'} = F_f + \frac{mv^2}{R} sin\alpha \qquad \text{(Eq. 5.11)}$$

$$F_y = F_c cos\alpha = \frac{mv^2}{R} cos\alpha \qquad \text{(Eq. 5.12)}$$

where $F_{t'}$ = total tractive force; F_f = friction force; R = radius of the curve; v = speed of the vehicle; α = slip angle; F_y = lateral force; and F_c = centripetal force.

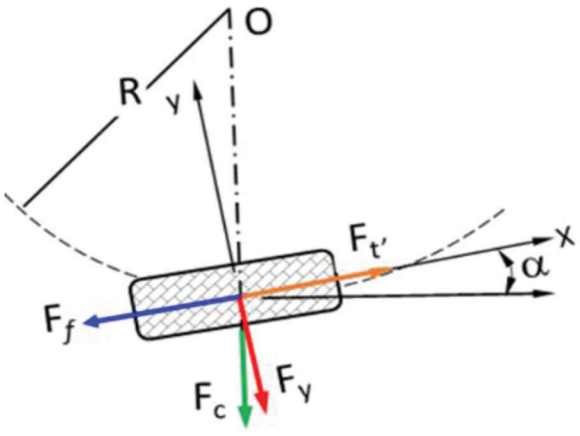

Figure 5.3 Forces acting on a wheel in cornering.

At small slip angles (i.e., 5 degrees or less), the relationship between the lateral force and slip angle is expressed as follows (Gillespie, 1992):

$$F_y = \alpha C_\alpha \qquad \text{(Eq. 5.13)}$$

where C_α = cornering stiffness that is dependent on variables such as tire size and type (radial- versus bias-ply construction), number of plies, cord angles, wheel width, and tread.

Substituting Equation 5.13 into Equation 5.12 yields the radius of the curve in Equation 5.14:

$$R = \frac{mv^2 cos\alpha}{C_\alpha \alpha} \qquad \text{(Eq. 5.14)}$$

Furthermore, substituting R and $F_f = mgf$ into Equation 5.11 yields the tractive force below by assuming that $tan\alpha \approx \alpha$:

$$F_{t'} \approx mgf + C_\alpha \alpha^2 \qquad \text{(Eq. 5.15)}$$

The coefficient of friction on a horizontal curve can then be calculated as follows:

$$f' = \frac{F_{t'}}{mg} = f + \frac{\alpha V^2}{Rg} \qquad \text{(Eq. 5.16)}$$

5.2 Friction Testing and Results

5.2.1 Locked Wheel Skid Tester Method

Several standard test methods such as the British pendulum tester (ASTM, 2018c), locked wheel skid tester (LWST) (ASTM, 2015d), and dynamic friction tester (ASTM, 2019c) have been accepted for measuring surface frictional properties in the field or laboratory or both in the US. However, the LWST method is currently the most widely used method for measuring the skid resistance of pavement at high speeds by State DOTs (Henry, 2000). The LWST method utilizes a measurement representing the steady-state friction force on a locked test wheel while (1) it is dragged over a wetted pavement surface under constant load and at a constant speed; and (2) its major plane is parallel to its direction of motion and perpendicular to the pavement.

When performing friction testing on a straight, level pavement section by the use of LWST, the friction measurement is expressed as skid number (SN) called in ASTM E274 or friction number (FN) called by INDOT in Equation 5.17:

$$SN(or\ FN) = f \cdot 100 = \frac{F_t}{mg} \cdot 100 \qquad \text{(Eq. 5.17)}$$

where f = coefficient of friction on a level, straight pavement section as defined in Equation 5.5.

On the one hand, the ASTM E274 LWST method is designated for pavement sections that are straight with flat surface. On the other hand, HFST is commonly

installed to enhance pavement friction performance on curves or steep grades. Therefore, caution should be exercised if the LWST method is utilized to evaluate the friction performance of HFST. When performing friction testing by the use of LWST on straight grades, the potential errors due to the effect of grade may be cancelled by averaging the friction measurements made in both directions as shown in Equation 5.10. Substituting Equation 5.10 into Equation 5.17 yields a value that represents the actual friction number on a level pavement in Equation 5.18:

$$FN = \frac{FN_U + FN_D}{2} \qquad \text{(Eq. 5.18)}$$

where FN_U and FN_D = friction numbers measured using the LWST method uphill and downhill, respectively.

When the pavement test section is on a horizontal curve, the coefficient of friction may be determined from Equation 5.16. The coefficient of friction consists of two parts. The first part is *f*, i.e., the actual friction provided on a straight pavement. The second part is here called "virtual friction" that arises due to the centripetal force and explains the extra friction demand on horizontal curves. Notice that during the LWST test, the vertical static load provided to the locked wheel is $1{,}085 \pm 15$ lbf and the test speed is either 40 mph or 30 mph utilized by INDOT on horizontal curves. The virtual friction can be estimated from Figure 5.4 by further assuming a slip angle of 5°. The virtual friction increases as test speed increases or radius decreases. The actual friction number on a straight pavement can then be determined in Equation 5.19:

$$FN = FN' - \left(\frac{\alpha V^2}{Rg} \times 100\right) \qquad \text{(Eq. 5.19)}$$

where FN = actual friction number on a straight pavement section; and FN' = total friction number on a horizontal curve measured directly by the use of LWST method.

5.2.2 FN Test Results

The protocol utilized for FN measurements is illustrated in Figure 5.5. On a simple circular curve as shown in Figure 5.5(a), FN measurements were made at three positions, i.e., before the point of curvature (PC), at the midpoint of the curve (MC), and after the point of tangency (PT). On a reverse curve as shown in Figure 5.5(b), FN measurements were made at five positions, i.e., before the point of curvature (PC), at the midpoints of the curve (MC_1 and MC_2), at the point of reverse curvature (PRC), and after the point of tangency (PT). Figure 5.6 shows the typical FN measurements made at two HFST sites, including SR-62a with a simple circular curve and SR-446 with a reverse curve. At the SR-62a site, the FNs at the midpoints are less than those at both PC and PT. This confirms the dynamics of vehicle on horizontal curves, i.e., the pavement surface on a curve tends to polish more rapidly due to the extra external force (see Equation 5.15). However,

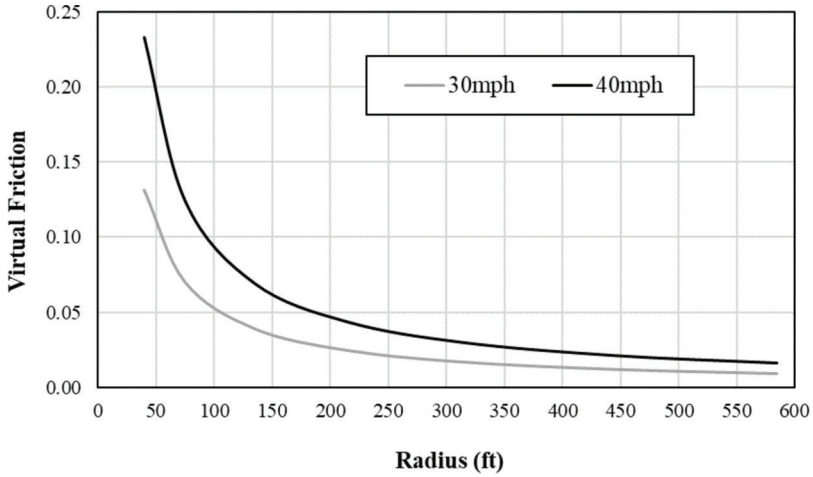

Figure 5.4 Reduction in friction on horizontal curves.

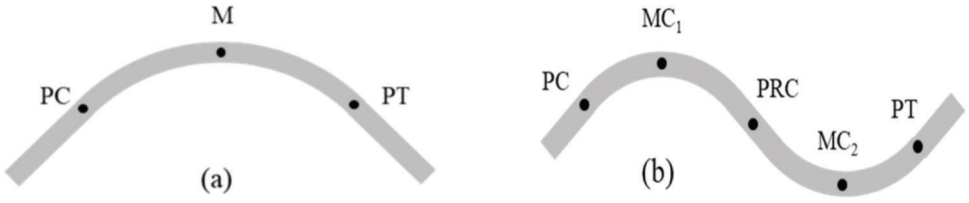

Figure 5.5 Test protocol for friction testing: (a) simple curve and (b) reverse curve.

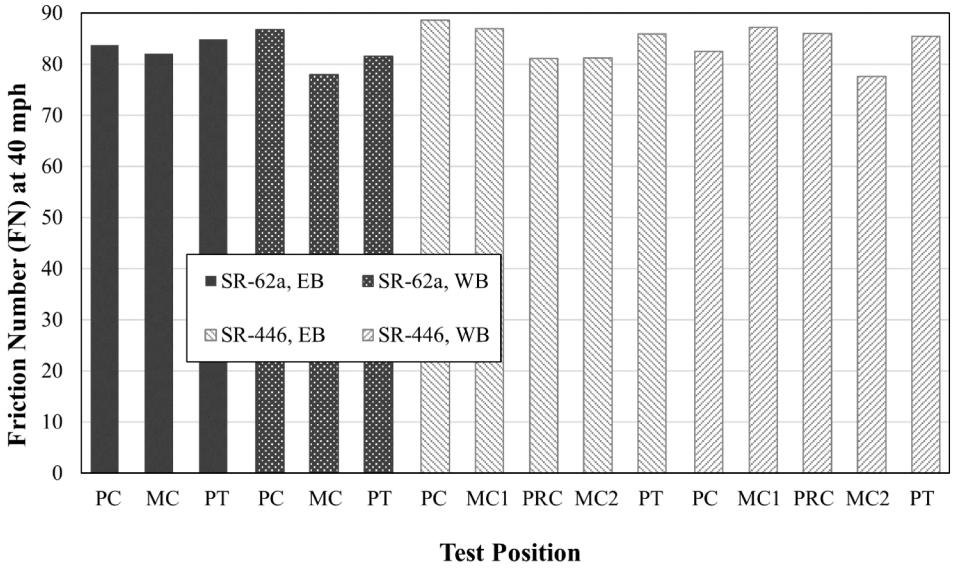

Figure 5.6 Friction measurements: (a) SR-62a (simple curve) and (b) SR-446 (reverse curve).

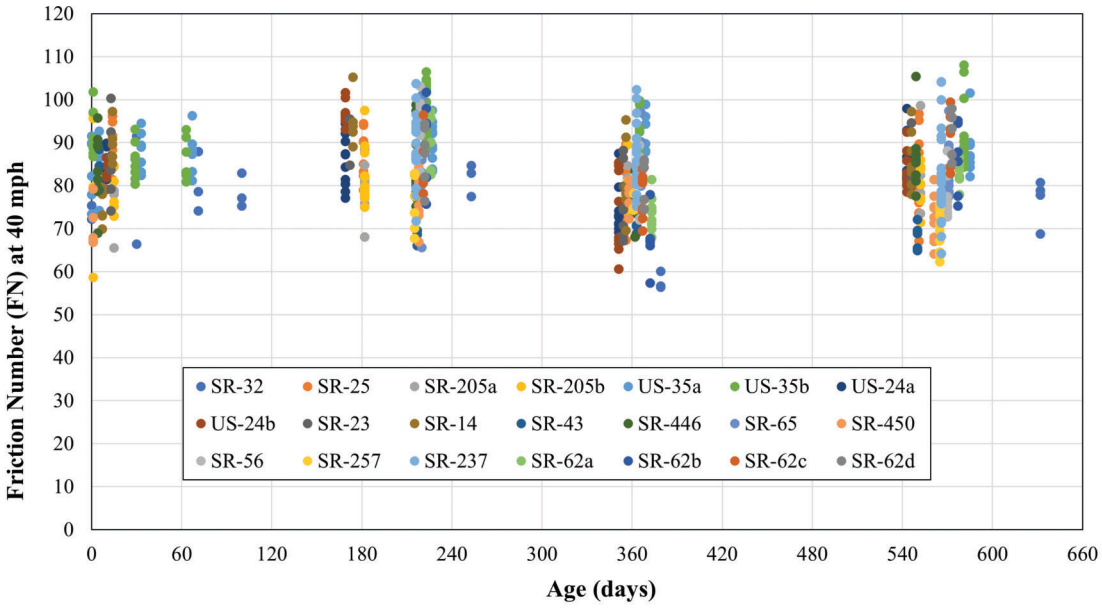

Figure 5.7 Friction number (FN) measurements made over an 18-month period after construction.

the FN at the midpoint of curve on SR-446, such as FN at MC_1 westbound, is greater than those at PC and PRC. This is probably due to the variation of pavement friction. It was reported that pavement friction may vary from position to position, especially laterally (Li et al., 2005). While performing friction testing on horizontal curves by the use of LWST, it is very difficult to position the test wheel in the wheel track. Moreover, HFST is placed by casting calcined bauxite chips onto the epoxy binder and its surface texture may vary greatly.

To determine the surface friction of HFST and its variation, friction testing has been conducted multiple times, i.e., right after, 6 months, 12 months, and 18 months after construction. Friction testing has been conducted several more times at seven HFST sites, including SR-32, SR-205b, US-35a, US-35b, SR-14, SR-446, and SR-450. Overall, a total of 701 valid FN measurements have been made at these 21 HFST initiative sites (see Figure 5.7). Both Pearson (linear) and Spearman rank (non-linear) correlations were examined to determine the relationships between FN and the

independent variables such as AADT, Truck, Age, and Radius (see Table 5.1). The coefficients are very consistent between these two methods except AADT. The negative *r* for Age indicates that FN tends to decrease over time. The absolute values of all correlation coefficients are less than 0.30 except Radius. The relationship is weak to very weak between FN and AADT, Truck or Age, and is moderate between FN and Radius. The p-value between FN and AADT is greater than 0.05 (i.e., the level of significance), which indicates there is inconclusive evidence about the significance of the relationship between FN and AADT. Evidently, the effects of AADT, Truck, and Age on FN are negligible when compared to Radius.

5.2.3 Expected Friction Numbers

Because no significant correlations exist between FN and variables such as AADT, Age, and Radius, it is possible to combine all 701 FN measurements (see Figure 5.6) to establish a rational basis for determining expected friction performance. Table 5.2 presents the summary statistics of the FN measurements, including mean, standard deviation, lower bound, and upper bound, by the age of HFST such as new HFST, and 6, 12, and 18 months after construction. The largest mean value occurred at the age of 6 months and the smallest mean value occurred at the age of 12 months. However, the standard deviations remain consistent. Although there is no clear trend in the summary statistics shown in Table 5.2, two significant observations can be made for the FN measurements as follows:

TABLE 5.1
Summary of correlation analysis results

(a) Pearson Correlation				
Variable	**AADT**	**Truck[1]**	**Age[2]**	**Radius[3]**
Coefficient (r)	0.000	0.138	-0.143	0.342
p-value	0.995	0.000	0.000	0.000
(b) Spearman Rank Correlation				
Variable	**AADT**	**Truck**	**Age**	**Radius**
Coefficient (r)	-0.011	0.212	-0.124	0.353
p-value	0.774	0.000	0.001	0.000

[1]Truck = truck volume.
[2]Age = age of HFST.
[3]Radius = radius of curve.

TABLE 5.2
Summary statistics of FN measurements by age

Age	N	Mean	SD[1]	Lower Bound	Upper Bound
New	78	83.4	9.0	81.4	85.4
6 Months	223	87.8	9.1	86.6	89.0
12 Months	181	80.9	9.7	79.5	82.3
18 Months	219	82.8	9.0	81.6	84.0
All	701	84.0	9.6	83.3	84.7

[1]SD = standard deviation.

1. Although FN has varied over time, it tends to be stable 12 months after construction.
2. Although the mean FN values have fluctuated over time, they are all greater than 80.

The summary statistics of HFST measurements are sensitive to data outliers due to system error, human error, and the deviation of HFST surface characteristics. The INDOT's friction test program consists of robust procedures for calibrating testing systems (Li et al., 2007). In addition, all friction tests were performed by certified friction test operators. It is reasonable to attribute the possible outliers mainly to the deviations of HFST surface characteristics, including spatial variability in surface texture. The lower and upper bounds with a confidence level of 95% are used to identify and remove the data outliers. Presented in Table 5.3 are the summary statistics of FN measurements such as mean, standard deviation, and coefficient of variation by exclusion of the data outliers. It is shown that the standard deviations decrease dramatically but the mean values remain almost the same after the data outliers are removed (see Tables 5.2 and 5.3).

5.3 Macrotexture Testing and Results

5.3.1 Mean Profile Depth and Test

A single texture height parameter, i.e., the mean profile depth (MPD), was utilized to characterize the texture profile of HFST surface. This is because MPD may also be used as a construction contractual requirement in the process of quality control (QC) and quality assurance (QA) for certain pavement surface treatments such as chip seal (Zhao et al., 2018). In addition, MPD is the depth parameter of pavement surface macrotexture and has proven to have a well-pronounced correlation with wet pavement friction (Li et al., 2016) and wet pavement crash (Henry, 2000). In particular, continuous texture data can be readily measured at highway speeds and provides solid advantages over the spot FN measurement by the use of LWST (de León Izeppi et al., 2019). The calculation of MPD is performed in accordance with ASTM standard practice as follows (ASTM, 2015c):

$$MPD = \frac{1}{N}\sum_{i=1}^{N} MSD_i \qquad \text{(Eq. 5.20)}$$

TABLE 5.3
Summary statistics of FN measurements by exclusion of outliers

Age	Mean	SD[1]	COV[2], %
New	83.0	1.3	1.51
6 Months	87.8	0.7	0.83
12 Months	80.8	0.7	0.92
18 Months	82.7	0.5	0.64
All	84.0	0.4	0.50

[1]SD = standard deviation.
[2]COV = coefficient of variation.

where N is the number of 100-mm long segments in the test section, and MSD is the mean segment depth (MSD) of a 100-mm texture profile.

In reality, MPD is the reduction of thousands of MSD measurements in a single pavement section. A macrotexture test system developed in another study was utilized to provide accurate and precise MSD measurements (Zhao et al., 2018). This system utilizes the latest point laser texture sensing technologies to continuously collect macrotexture information with a sample rate of 100 kHz at highway speeds. One unique feature of this test system is the use of two point-lasers, one for each of the two wheel tracks, which is anticipated to generate two texture profiles for calculating MPD. Presented in Figure 5.8 are the typical macrotexture MSD measurements made over a 50 foot-long HFST. There are approximately a total of 154 MSD measurements in each wheel track. The average of the MSD measurements is 1.351 mm in the left wheel track and 1.154 mm in the right wheel track. Taking the average of these two MSD averages yields the MPD for this 50 foot-long HFST.

Due to the repeated applications of moving vehicle tires, the surface in the wheel tracks tend to be polished more rapidly and prone to aggregate loss. Continuously measuring the texture information in the two wheel tracks ensures a high probability of detecting early defects such as immediate and excessive aggregate loss. It should be pointed out that the texture profile generated by a point-laser is actually a 2D representation of 3D surface texture. Therefore, errors may occasionally arise from a lack of true 3D surface texture profiles. To simulate the possible effects of aggregate loss on MPD, the authors fabricated seven HFST tile specimens by assuming an aggregate loss of 0.0%, 25.0%, 37.5%, 50.0%, 62.5%, 75.0%, and 87.5%, respectively, as shown in Figure 5.9(a). Figure 5.9(b) shows the seven MPD measurements with an aggregate loss as specified above. The MPD with 25.0% aggregate loss is less than those with 37.5% and 50.0%, respectively, and the MPD with 75.0% aggregate loss is greater than that with 62.5% aggregate loss. This indicates that the MPD calculated from a 2D texture profile generated by the use of a point-laser may not occasionally represent the true surface texture. To address the above issues, the authors investigated an approach based on the 3D pavement surface models generated from smartphone images as shown in the appendix of this report.

5.3.2 Effect of Spikes in Texture Data

As mentioned earlier, two texture profiles are simultaneously measured in the left and right wheel tracks, respectively, during testing. Notice that the texture profiles are commonly generated after spikes in the collected texture data have been removed with a denoising method utilized in the test system.

Plotted in Figure 5.10 are the MSD measurements along the two left wheel tracks at the HFST site on SR-43. It is shown that the MSD measurements in both wheel tracks fluctuated around 1.0 mm. Evidently, some spikes up to 23.5 mm still remain in the texture data along the right wheel track. Because of the sensitivity of the summary statistics to spikes, it is of importance to understand those spikes and ensure that the descriptive statistics of the MSD measurements best represent the true surface texture. Nevertheless, the spikes in the collected texture data arise due to not only the laser system itself, but also the presence of surface distresses or defects, especially delamination, cracking, and aggregate loss in the surface of HFST. Removing all spikes, including those due to surface distresses and defects, may compromise the effectiveness of the use of texture metrics for QC and QA of HFST.

Macrotexture is categorized as the texture with wavelengths ranging from 0.5 mm to 50 mm and peak to peak amplitudes ranging from 0.01 mm to 20 mm (Permanent International Association of Road Congress, 1987). To further examine the spikes retained in the texture data, the authors assessed the MSD measurements and surface conditions at two HFST sites, including US-24b, and SR-23, as shown in Figure 5.11. At the HFST site on US-24b, the spikes represent mainly the delamination in the surface of HFST. At the HFST site on SR-23, the spikes represent mainly the surface defects, such as wide cracks due to severe raveling of

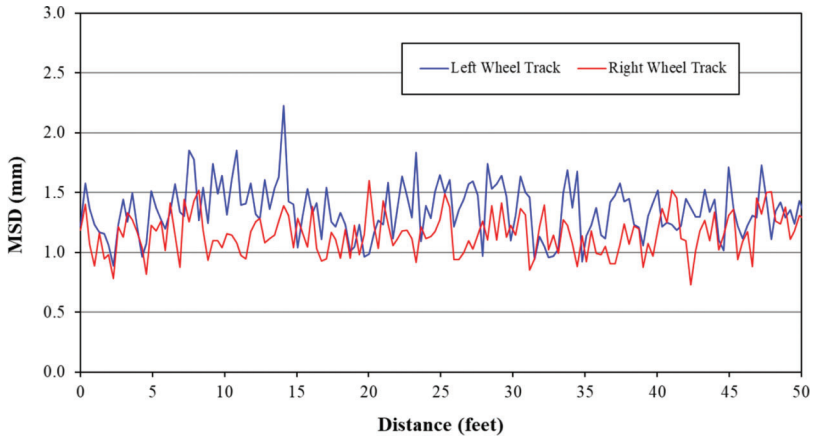

Figure 5.8 Graphical illustration of mean segment depth (MSD) measurements.

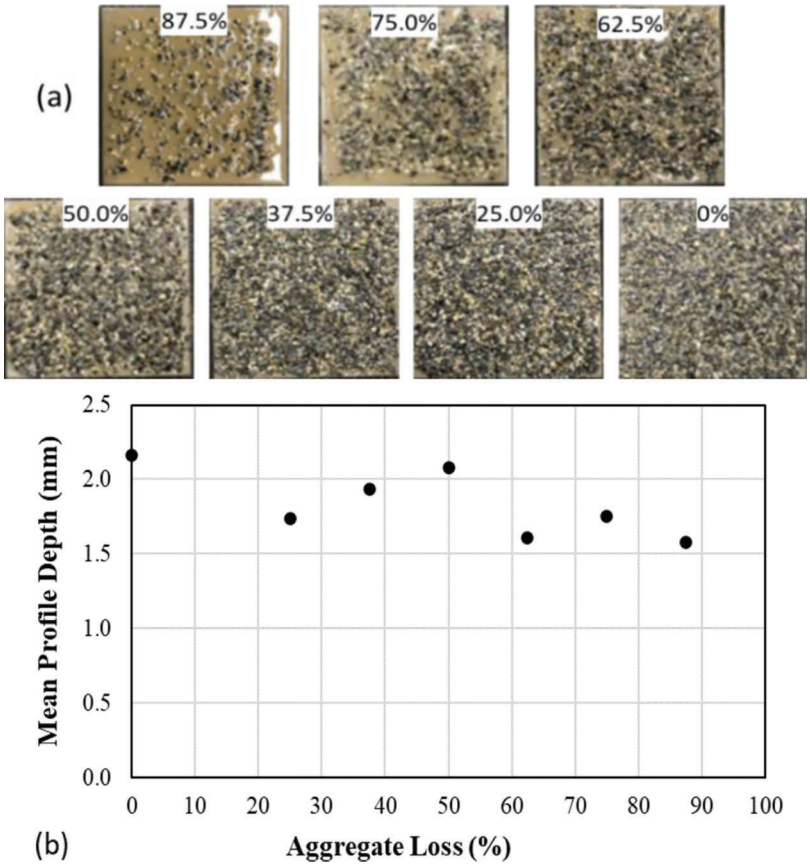

Figure 5.9 Simulation of aggregate loss: (a) photo of specimens and (b) mean profile depth (MPD) measurements.

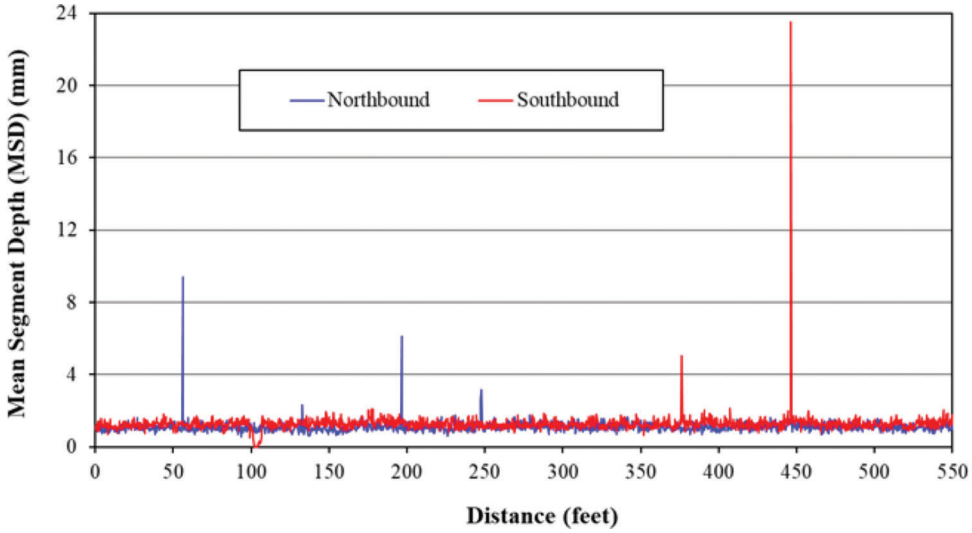

Figure 5.10 Mean segment depth (MSD) measurements of HFST at SR-43.

crack edges. Table 5.4 shows the summary statistics of the MSD measurements by keeping and removing the spikes in the measurements. Evidently, the spikes affect the standard deviation and coefficient of variation more significantly than the mean. As a general rule of thumb, therefore, spikes greater than 20 mm, i.e., the maximum amplitude of macrotexture defined by PIARC, are removed while calculating the statistics of MSD measurements, particularly MPD.

5.3.3 Expected Mean Profile Depths

Presented in Figure 5.12 are the MPD values measured in each of the two wheel tracks in both

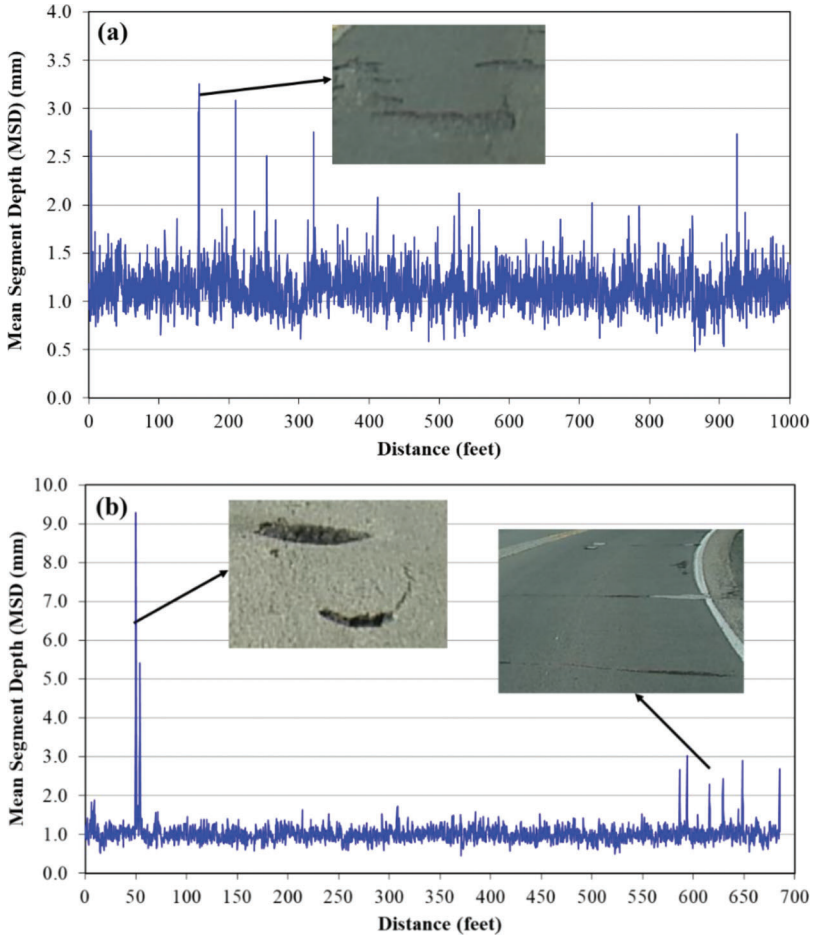

Figure 5.11 Causes for spikes in mean segment depth (MSD) measurements: (a) delamination, US-24b and (b) crack spalling, SR-23.

TABLE 5.4
Summary statistics of MSD measurements before and after removing spikes

	SR-62a		US-24b		SR-23	
HFST Site	**Before**	**After**	**Before**	**After**	**Before**	**After**
Mean (mm)	1.194	1.191	1.210	1.202	1.012	0.997
SD[1] (mm)	0.230	0.215	0.195	0.161	0.308	0.186
COV[2] (%)	19.3	18.1	16.1	13.4	30.5	18.7
Range (mm)	0.580–3.748		0.491–3.258		0.462–9.280	

[1]SD = standard deviation.
[2]COV = coefficient of variation.

directions at seven HFST sites, including SR-32, SR-205a, SR-205b, US-35a, SR-14, SR-446, and SR-450, over an 18-month period after construction. The MPD value decreased as the HFST age increased. It appears that the MPD values decreased dramatically in the first 3 months. Afterwards, the MPD values gradually approached 1.0 mm over time. This agrees very well with the finding reported elsewhere (Li et al., 2017), which states that the MPD of HFST will decrease noticeably in the first 3 months and remain very stable afterward. The relationships between MPD and the four independent variables, including AADT, Truck (volume), Age (of HFST), and Radius (of curve) were further examined by the use of both Pearson and Spearman rank correlation methods, respectively, and the results are presented in Table 5.5.

It is shown that all correlation coefficients are negative, regardless of the analysis method, which indicates that MPD decreases as these independent variables increase. MPD and AADT have a weak linear relationship (i.e., Pearson correlation coefficient = -0.280), but a moderate non-linear relationship (i.e., Spearman rank correlation coefficient = -0.410). Both the Pearson and Spearman rank correlation

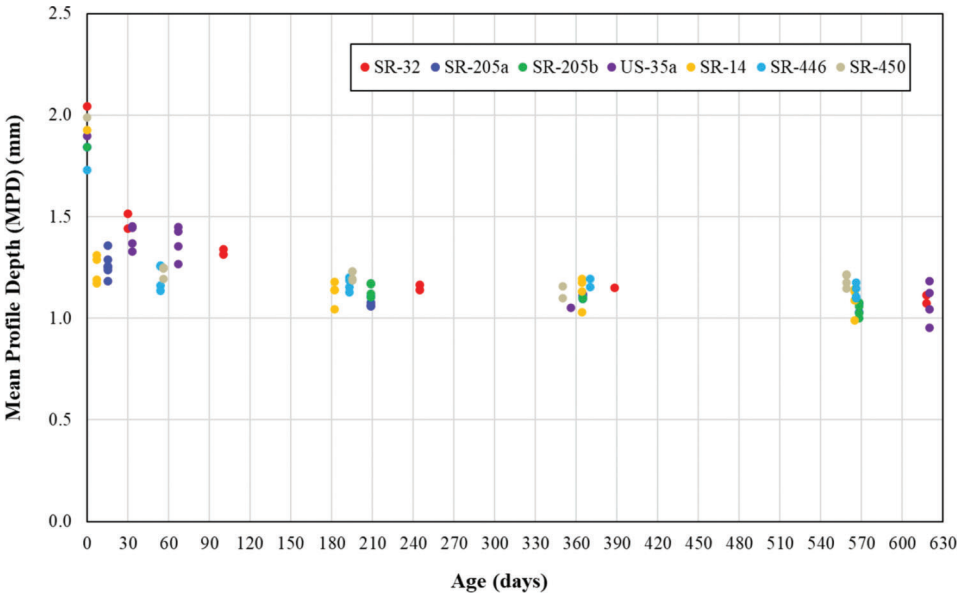

Figure 5.12 Mean profile depth (MPD) measurements at 7 HFST sites over an 18-month period.

TABLE 5.5
Summary of correlation analysis results

(a) Pearson Correlation				
Variable	**AADT**	**Truck**	**Age**	**Radius**
Coefficient (r)	-0.280	-0.249	-0.413	-0.016
p-Value	0.000	0.000	0.000	0.789
(b) Spearman Rank Correlation				
Variable	**AADT**	**Truck**	**Age**	**Radius**
Coefficient (r)	-0.410	-0.233	-0.329	-0.176
p-Value	0.000	0.000	0.000	0.003

coefficients indicate a weak relationship between MPD and Truck. The relationship between MPD and Radius is very weak based on both the Pearson and Spearman rank correlation coefficients, while there is no conclusive evidence about the significance of the linear relationship (Pearson correlation). Nevertheless, both the absolute values of Pearson and Spearman rank correlation coefficients between MPD and Age are greater than 0.30 with a p-value equal to zero. In other words, there is a moderate relationship between MPD and Age that is statistically significant. It should be pointed out that the age of HFST is essentially a measurement of traffic applications. In short, it is possible to determine the expected MPD by combining the MPD measurements at different HFST in terms of the age.

Assume there are a total of N HFST sites. The expected MPD in terms of all N HFST sites can be calculated as follows:

$$MPD = \frac{1}{N}\sum MPD_i \qquad \text{(Eq. 5.21)}$$

where MPD = expected MPD; N = number of HFST sites; and MPD_i = MPD of the ith HFST site.

Expand Equation 5.21 into a Taylor series and take the first-order approximation. Notice that the 1st derivative $\frac{\partial MPD}{\partial MPD_i} = \frac{1}{N}$. The mean and standard deviation of MPD are given as follows:

$$\overline{MPD} = \frac{1}{N}\sum \overline{MPD_i} \qquad \text{(Eq. 5.22)}$$

$$SD = \frac{1}{N}\sqrt{\sum SD_i{}^2} \qquad \text{(Eq. 5.23)}$$

where $\overline{MPD}$= mean of the expected MPD; $\overline{MPD_i}$ = mean of the MPD at the ith HFST site; SD = standard deviation of the expected MPD; SD_i = standard deviation of the MPD at the ith HFST site; and N = number of the HFST sites.

Similar to friction testing, texture testing has also been conducted multiple times, i.e., right after, 6 months, 12 months, and 18 months after construction. The detailed MPD measurements are presented in Appendix B. For new HFST, MPD measurements were made over the HFST surface using a laser texture scanner before opening to traffic at a total of six sites. Afterwards, MPD measurements were made in both the left and right wheel tracks in both directions by the use of the aforementioned test system with two point-lasers. Consider the MPD measured in each wheel track as an independent sample. Substituting the statistics of each MPD sample into Equations 5.22 and 5.23 yields the summary statistics of the expected MPDs at different ages as shown in Table 5.6. The MPD for new HFST is expected to be approximately 1.9 mm. It will decrease to around 1.40 mm after 1 month and to 1.20 mm after 2 months. As time

TABLE 5.6
Summary statistics of expected MPDs by age

Age	N	Mean (mm)	SD[1] (mm)	Lower Bound (mm)	Upper Bound (mm)
New	6	1.905	0.047	1.868	1.943
1 Month	18	1.444	0.061	1.415	1.472
2 Months	12	1.242	0.078	1.198	1.286
6 Months	72	1.222	0.028	1.215	1.228
12 Months	60	1.194	0.032	1.186	1.202
18 Months	80	1.181	0.025	1.175	1.186

[1]SD = standard deviation.

increases, the MPD approaches around 1.10 mm. The standard deviations at the age of 0 month (new), 1 month, and 2 months are much greater than those at the ages of 6, 12, and 18 months. This confirms again that HFST surface may experience the greatest variability in the first 3 months.

6. SAFETY EVALUATION OF HFST

6.1 Safety Performance Measure

6.1.1 Crash Modification Factors

It was reported by the Indiana Criminal Justice Institute (ICJI) (2017) that about 200,000 vehicle crashes occurred in Indiana every year from 2013 through 2017, of which about 34,000 crashes resulted in injuries and 755 crashes caused fatalities. Of these crashes, 20% were further attributed to insufficient surface friction on horizontal curves. Therefore, HFST plays an important role in reducing vehicle crashes on highway curves. This chapter mainly discusses the safety performance of HFST by performing before-after analysis of crash data at all 25 HFST sites to determine the so-called crash modification factor (CMF). Meanwhile, state-wide highway horizontal curve segment crash frequency model is developed to quantify the effect of curve radius and pavement friction on vehicle crashes and to verify the estimated HFST CMF.

When considering the implementation of a particular countermeasure such as HFST at a specific site, CMF may be used to assess its expected safety impact. A CMF value greater than, less than and equal to 1.0, respectively, indicate an increase, a decrease and no change in vehicle crashes that will result from the treatment (Gross et al., 2010). There have been multiple methods to develop CMFs. Before-after with comparison group studies use an untreated comparison group of sites similar to the treated ones to account for changes in vehicle crashes unrelated to the treatment such as crash trends over time and with traffic volume. Empirical Bayes before-after studies more precisely estimate the number of crashes that would have occurred at a treated site in the after period if a treatment had not been implemented. The effect of the safety treatment is estimated by comparing this value to the number of actual crashes after treatment. Full Bayes studies uses a reference group to estimate the expected crash frequency and its variance from a calibrated safety performance function (SPF). Cross-sectional studies examine the crash experience of locations with and without a certain feature and then attribute the difference to that feature. Case-control studies are based on cross-sectional data. They assess whether exposure to a potential treatment is disproportionately distributed between the cases and controls, thereby indicating the likelihood of an actual benefit from the treatment. In cohort studies, sites are assigned into a particular cohort and followed over time to observe exposure and event frequency. They then assess whether the time at risk is disproportionate between cohorts, which indicates the relative effect of the treatment (AASHTO, 2010).

6.1.2 Curve Crash Frequency Model

Considering that only 1-year data after treatment has been collected, the safety performance of HFST need to be proved without adequate multiple years of data. Modeling the statewide horizontal curve crash frequency is a way to calculate the efficiency of HFST in theory. Numerous models have been reported to model curve crash frequencies all over the world. Elvik (2013) has summarized three measures of safety for horizontal curves from several published studies in various countries: (1) the number of accidents per curve; (2) accident rate (number of accidents per million vehicle kilometers of travel); and (3) accident modification factors (AMFs). The number of accidents per curve is considered as a dependent variable. The horizontal curve crash prediction model for rural two-lane roads in Ontario, Canada (Persaud et al., 2000) is one of the most representative crash count models in such studies:

$$Accident\ per\ curve\ per\ year = (AADT)^b (L)^g R^p exp(a + h(L/R)) \quad \text{(Eq. 6.1)}$$

where $AADT$ is the Annual Average Daily Traffic; L is the length of the curve in kilometers; R is the radius of the curve in meters; L/R is the ratio of the length of the curve (kilometers) to the radius of the curve (meters); and a, b, g, h, and p are the coefficients estimated by means of negative binomial regression, respectively.

Another similar form of model has been developed to predict the number of single-vehicle run-off-road accidents to the left as follows (Jurewicz et al., 2010):

$$Number\ of\ accidents = \exp\left(\beta_0 + \beta_1 AADT_{one} + \beta_2 Radius + \beta_3 Grades + \beta_4 TLSS + \beta_5 CZ\right) + \varepsilon \quad \text{(Eq. 6.2)}$$

where β_0 to β_5 are the coefficients estimated by means of negative binomial regression; $AADT_{one}$ is the Annual Average Daily Traffic in one direction; *Radius* is the horizontal curve radius in meters; *Grades* refers to whether the road is flat or on a slope; *TLSS* is the width of the traffic lane plus sealed shoulder; *CZ* is the clear zone width category; and ε is the error term.

When considering crash count models, Poisson and negative binomial regression count models are the most appropriate methodological techniques for frequency modeling. Beyond the standard Poisson and negative binomial regressions, zero-inflated probability processes such as the zero-inflated Poisson (ZIP) and zero-inflated negative binomial (ZINB) regression models have been developed by Miaou et al. (1993) and attracted extensive interests in accident frequency analysis. Lee and Mannering (2002) applied the zero-inflated count models of accident frequency to rural run-off-roadway accidents. Lord et al. (2005, 2007) provided defensible guidance on how to appropriate model crash data with a preponderance of zeros.

6.2 Data

Automated Reporting Information Exchange System (ARIES Portal) stores all traffic crash records in Indiana. Because all HFST projects were completed around August–October 2018, crash data on State and U.S. routes from 2015–2020 was retrieved for the before-after crash analysis. The 2015–2018 data was sued as the "before" data. However, the "after" data did not include the 2020 data due to the impact of COVID-19 on traffic. As errors exist in GPS coordinates, the CLIP software was used to correct crash locations by referring position description in database (Imprialou et al., 2019). To get the most precise HFST pavement segment shapefiles, digitization was conducted to record the satellite images and construction information. These images were published in 2014 with pixel size of 3 m and available from National Agriculture Imagery Program (NAIP). Overall, 3.696 miles of 25 HFST pavement segments were digitized for crash counting. The crashes occurred within 25 meters from the centerline of HFST segment were considered as curve crashes. Table 6.1 shows the detailed crash counts and HFST site information.

TABLE 6.1
Indiana HFST site and crash information

		FN at 40 mph		Wet Weather Crashes		Injury Crashes		All Crashes	
HFST Site	**Length (mile)**	**Before**	**After**	**Before**	**After**	**Before**	**After**	**Before**	**After**
SR-25	0.25	34.9	81.5	5	0	5	0	11	3
SR-205	0.157	31.7	79.8	2	0	0	0	3	0
US-35	0.28	35.2	93.1	0	0	0	0	0	0
US-24	0.18	25.1	81.2	1	1	1	0	5	2
US-24	0.16	26.0	84.9	4	0	1	0	10	0
SR-23	0.11	47.5	82.7	0	1	0	0	1	1
SR-65	0.21	52.4	84.4	1	0	1	0	2	2
SR-450	0.14	23.1	75.3	1	0	1	0	2	1
SR-257	0.15	23.4	72.3	0	0	0	0	1	2
SR-237	0.61	38.1	87.6	2	0	1	0	3	0
SR-62	0.1	44.5	82.4	0	0	1	0	2	1
SR-62	0.11	46.7	81.9	0	0	3	1	6	3
SR-62	0.13	51.5	84.0	0	0	0	0	0	1
SR-62	0.11	52.4	88.2	0	0	0	1	1	1
SR-56	0.14	53.5	86.0	0	0	0	0	1	0
SR-14	0.05	24.3	87.1	1	1	0	0	1	1
SR-43	0.09	28.6	67.9	1	0	1	1	2	1
SR-446	0.33	19.9	83.1	4	0	2	1	4	4
SR-205	0.08	29.1	81.2	4	0	0	0	4	0
US-35	0.17	42.2	87.2	0	0	0	1	0	1
US-35	0.06	52.3	87.2	1	0	1	0	3	0
SR-38	0.06	52.3	85.9	1	4	2	0	12	6
US-35	0.2	41.1	88.9	1	0	2	0	3	0
SR-32	0.049	44.5	71.2	0	0	0	0	1	0
US-35	0.17	43.8	87.7	0	0	0	0	4	1
Sum	4.096	–	–	29	7	22	5	82	31

TABLE 6.2
Description of variables

Variables	Description
N	Number of crashes per curve segment during 2015–2018
rad (ft.)	Radius of curve segment in feet
FN	Friction number on the curve measured at 40 mph
L (ft.)	Length of curve segments in feet
AADT	The average AADT divided by 1,000 during 2015–2018

TABLE 6.3
Summary statistics for variables

Variables	Mean	SD[1]	Min	Max	Case
N	0.744	2.05	0	60	20955
rad (ft.)	1,172.80	666.31	82.15	3,261.58	20955
FN	43.74	14.68	8.1	111.5	20955
L (ft.)	338.12	293.27	82.02	4,090.35	20955
AADT	7.302	355.54	0.105	164.997	20955

[1]SD = standard deviation.

In curve crash frequency modeling, road shapefile was combined from INDOT road polylines of Boone and Putnam counties with Indiana Geographic Information Office (IGIO) road polylines for the rest counties. Curve segments were detected and calculated by the ROCA software in ArcMap (Bíl et al., 2018), and 20,599 curve segments were identified. A total of 146,831 crashes occurred on both state roads and US highways during 2016–2018 were collected from ARIES as the original crash dataset. There were 15,216 crashes that meet the following screening process: (1) corrected coordinates located within 164 ft. (50 meters) from the centerline of road shapefile; (2) corrected coordinates located within 164 ft. (50 meters) from the centerline of an identified curve segment; (3) no junction was involved. Friction shapefile data was created using the friction measurements by INDOT. All friction measurements were converted to friction numbers (FNs) with the standard smooth tire at 40 mph. The AADT shapefile data was downloaded from INDOT traffic flow website. Crash records, road curve segment, friction, and AADT are all spatially correlated by ArcMap. Description and summary statistics of five variables applied in this model are shown in Table 6.2 and Table 6.3, respectively.

6.3 Before-After Analysis for HFST

6.3.1 Empirical Bayes Method

Since HFSTs are installed at locations that may have a higher risk than at normal curve segments, before-after studies need to account for potential bias due to regression to the mean. One of the most popular way to address regression-to-the-mean problem is the Empirical Bayes (EB) procedure as outlined by Hauer (1997). SPFs are an integral part of the EB procedure (Srinivasan et al., 2013). The objective of the empirical Bayes methodology is to more precisely estimate the number of crashes that would have occurred at an individual treated site in the after period if HFST had not been implemented. The approach to solve regression-to-the-mean is to generate the number of crashes expected in the after period if there is no treatment and compare it with observed after period crash count. The parameters needed to calculate the number of crashes expected in the after period ($N_{expected,T,A}$) are the following:

- The observed number of crashes in the "before" period for the treatment group ($N_{observed,T,B}$).
- The observed number of crashes in the "after" period for the treatment group ($N_{observed,T,A}$).
- The predicted number of crashes (i.e., sum of the SPF estimates) in the "before" period ($N_{predicted,T,B}$).
- The predicted number of crashes (i.e., sum of the SPF estimates) in the "after" period ($N_{predicted,T,A}$).

The number of crashes predicted at the treated sites based on the sites with similar operational and geometric characteristics ($N_{predicted,T,B}$) is derived from SPF. An SPF is a mathematical model that predicts the mean crash frequency for similar locations with the same characteristics. These characteristics typically include traffic volume and may include other variables such as traffic control and geometric characteristics. All these HFST pavement sites are located on rural two-lanes roads with HFST installed in both directions, except C-5 that consists of HFST installed only in one direction. The SPF used to estimate road segments in the base condition without horizontal curvature is:

$$N_{spf\,rs} = AADT \times L \times 365 \times 10^{-6} \times e^{-0.312} \quad \text{(Eq. 6.3)}$$

where $N_{spf\ rs}$ is predicted total crash frequency for roadway segment in the base condition; AADT is average annual traffic volume; and L is length of roadway segment (miles).

The calibration factor for this SPF is the CMF for horizontal curvature:

$$CMF = \frac{(1.55 \times L_c) + (80.2/R) - (0.012 \times S)}{(1.55 \times L_c)} \quad \text{(Eq. 6.4)}$$

where CMF is crash modification factor for the effect of horizontal alignment on total crashes; L_C is length of horizontal curves (miles) which includes spiral transition; R is radius of curvature (feet); and S is 1 if spiral transition is present and 0 if spiral transition is not present.

The predicted number of crashes (i.e., sum of the SPF estimates) in the before period is calculated as:

$$N_{predicted,T,B} = N_{spf\,rs} \times CMF \quad \text{(Eq. 6.5)}$$

The empirical Bayes estimate of the expected number of crashes without treatment is computed as:

$$N_{expected,T,B} = w \times N_{predicted,T,B} + (1 - w) \times N_{observed,T,B} \quad \text{(Eq. 6.6)}$$

where w is the SPF weight derived from over-dispersion parameter in the SPF calibration process, but also depends on the number of years of crash data in the period before treatment. If the SPF has little over-dispersion, more weight is placed on the crashes predicted from the SPF ($N_{predicted,T,B}$) and less weight on the observed crash frequency ($N_{observed,T,B}$). However, the weight is reduced if many years of crash data are used. w is calculated as:

$$w = \frac{1}{1 + kP} \quad \text{(Eq. 6.7)}$$

where k is the over dispersion parameter; and P is the sum of the predicted number of crashes in the before period.

For rural two-lanes road segments, k is calculated as:

$$k = \frac{0.236}{L} \quad \text{(Eq. 6.8)}$$

where k is the overdispersion parameter; and L is length of roadway segment (miles).

Figure 6.1 illustrates how the SPF estimate is weighted with the observed crash count to estimate $N_{expected,T,B}$. It is shown that the empirical Bayes estimate falls somewhere between the values from the two information sources ($N_{observed,T,B}$, and $N_{predicted,T,B}$). The regression-to-the-mean effect is the difference between $N_{observed,T,B}$ and $N_{expected,T,B}$. Then it is easy to get the number of crashes expected in the after period ($N_{expected,T,A}$):

$$N_{expected,T,A} = N_{expected,T,B} \times \frac{N_{predicted,T,A}}{N_{predicted,T,B}} \quad \text{(Eq. 6.9)}$$

The variance of $N_{expected,T,A}$ is estimated from $N_{expected,T,A}$, the before and after SPF estimates, and the SPF weight. It is calculated as follows:

$$Var(N_{expected,T,A}) = N_{expected,T,A} \left(\frac{N_{predicted,T,A}}{N_{predicted,T,B}}\right)(1 - w) \quad \text{(Eq. 6.9)}$$

The CMF of HFST sites is calculated as:

$$\text{CMF} = (N_{observed,T,A}/N_{expected,T,A}) / \left(1 + \left(Var(N_{expected,T,A})/N^2_{expected,T,A}\right)\right) \quad \text{(Eq. 6.10)}$$

Variance of CMF is calculated as:

$$Variance\ of\ (CMF) = \frac{CMF^2\left[\left(\frac{1}{(N_{observed,T,A})}\right) + Var(N_{expected,T,A})/N^2_{expected,T,A}\right]}{\left[1 + Var(N_{expected,T,A})/N^2_{expected,T,A}\right]} \quad \text{(Eq. 6.11)}$$

6.3.2 CMF Estimation

This estimate is only an approximation since it applies to an ideal comparison group with yearly trends identical to the treatment group, a situation that is practically impossible. Estimating such as CMF is not trivial. It is recommended to estimate the variance assuming an ideal comparison group and recognize that this estimate is a conservatively low approximation. The result of Empirical Bayes analysis CMF for all 25 HFST sites is shown in Table 6.4.

As shown in Table 6.4, the estimate of the HFST CMF using the empirical Bayes method is 0.701 with a standard deviation of 0.184. A key feature of the empirical Bayes method is that it reduces uncertainty in CMF estimates because it uses more information and a

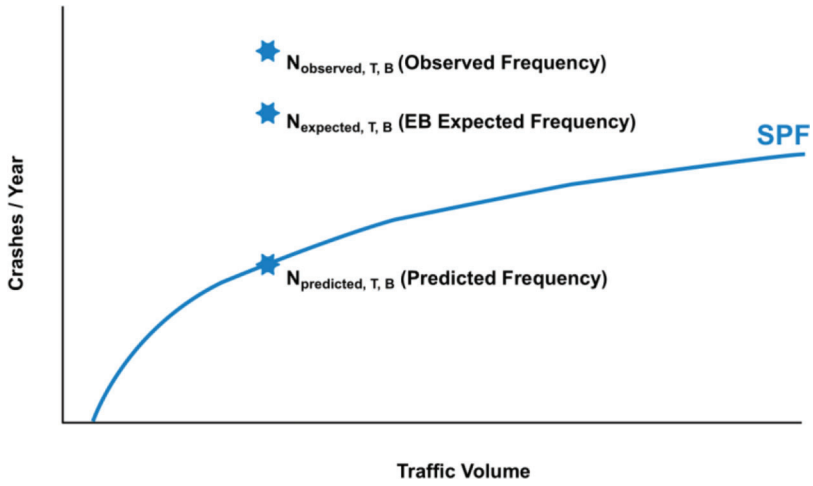

Figure 6.1 Illustration of regression-to-the-mean and empirical Bayes estimate (Gross et al., 2010).

TABLE 6.4
Aggregated CMF results for Indiana HFST sites

Crash Type	Observed Crash After	EB Expected After	CMF (std. dev)
Total	23	31.93	0.701 (0.184)
Injury	4	7.87	0.496 (0.195)
Wet weather	7	11.61	0.563 (0.172)

TABLE 6.5
Estimated HFST CMF value comparison with other states

Crash Type	Indiana	CMF by Merritt et al. (2015) (CO, KS, KY, MI, MT, SC, TN)	CMF by Lyon et al. (2020) (PA, WV, KY, AR)
Total	0.701	0.759	0.428
Wet weather	0.496	0.481	0.167

more rigorous methodology. There are research studies about HFST CMF in other states (see Table 6.5). Comparing the current study with the studies by other states, HFST installed around Indiana have demonstrated a safety impact in the well-proven range.

6.4 State-Wide Curve Crash Frequency Modeling

6.4.1 Model Selection

Since dependent variable crash frequency is count data, binomial, Poisson, negative binomial, zero-inflated Poisson, or negative binomial models (ZIP and ZINB) can be considered. To determine the most suitable model for this type of data, the characteristics of independent variable need to be examined. Total crash count with a mean of 0.744 and a standard deviation of 2.05 can possibly be regarded as an over-dispersed variable. Because the calculated overdispersion parameter α of 2.98 is greater than 1.96, i.e., the statistic at 95% confidence limit of the t-test, it can be confirmed that negative binomial model may provide a statistically better fit for the data.

Apart from over-dispersion, this type of crash data shows another property: 75% of curve segments have no crash records during the observation time period. With so many zero count cases, zero event may arise from two scenarios: (1) zeros come from inability to ever experience an event; and (2) zeros come from failing to observe an event during the observation time period. It is possible to apply the zero-inflated model. Because the calculated statistic is 13.34, i.e., greater than 1.96, the statistic at a confidence level of 95%, the zero-inflated negative binomial regression model may be better than the simple negative binomial model (Vuong et al., 1989).

6.4.2 Model Specification

The estimation results for the zero-inflated negative binomial specification for the crash frequency of curve segments are presented in Table 6.6. The coefficients for both non-zero crash state and zero-crash state were found to be statistically significant and of plausible sign. The zero-inflated negative binomial model consists of the following elements:

Count model:

$$\lambda_i = exp(\beta_0 + \beta_1 X_{1i} + \beta_2 X_{2i} + \beta_3 X_{3i} + \beta_4 X_{4i}) \quad \text{(Eq. 6.12)}$$

Logit model:

$$p_i = \frac{exp(\gamma_0 + \gamma_1 X_{1i} + \gamma_4 X_{4i})}{1 + exp(\gamma_0 + \gamma_1 X_{1i} + \gamma_4 X_{4i})} \quad \text{(Eq. 6.13)}$$

where λ_i is the expected value of count model; p_i is the probability of only zero counts; and X_1 is log (rad); X_2 is log (L); X_3 is log (FN); X_4 is log ($AADT$); and β_i and γ_i are given in Table 6.6.

Therefore, the curve crash count or frequency can be estimated as follows:

$$N = \frac{1}{3}\left(1 - \frac{e^{-8.83} rad^{0.29} AADT^{2.10}}{1 + e^{-8.83} rad^{0.29} AADT^{2.10}}\right) e^{-0.46} rad^{-0.22} L^{0.45} FN^{-0.46} AADT^{0.62} \quad \text{(Eq. 6.14)}$$

where N is the crash number per curve segment per year; rad is the curve radius (feet); L is the curve length (feet); and FN and $AADT$ are as defined earlier.

TABLE 6.6
Zero-inflated negative binomial estimation results

Variables	Estimated Coefficient	t-statistic	95% Confidence Interval
β_0	-0.46	-2.84	-0.68, -0.24
β_1	-0.22	-13.63	-0.25, -0.20
β_2	0.45	23.31	0.42, 0.50
β_3	-0.46	-9.14	-0.50, -0.41
β_4	0.62	51.59	0.60, 0.64
γ_0	-8.83	-21.83	-9.77, -7.89
γ_1	0.29	5.18	0.19, 0.39
γ_4	2.10	23.37	1.98, 2.22

6.4.3 Model Evaluation

The zero-inflated negative binomial model can be used not only to predict the crash frequency, but also to evaluate the potential effects of the primary variables in this study such as radius and friction. Increasing the radius of curve decreases the likelihood of crash frequency (negative coefficient in the negative binomial crash state), which suggests that curves with larger radii reduce angular velocity of speeding vehicles and decrease the probability of run off road (ROR), i.e., the major crash type on curves. It can also be seen that in the negative binomial crash state, increasing pavement friction decreases curve crash frequency. For a specific curve, however, increasing its length or AADT will increase the exposure of vehicle on curve segments and will eventually increase the crash frequency on it.

As shown in Table 6.7, only curve radius and AADT demonstrate statistical significance in terms of the zero-crash state. Increasing curve radius increases the probability that the curve segment would be in the zero-crash state, which reflects the better control of vehicles provided due to lower angular velocity. Pavement friction is moderately significant in the Negative binomial state, but not significant in the Zero-inflated logit state. AADT not only increases curve crash frequency in the negative binomial crash state, but also increases the probability of curve segment being in the zero-crash state. This indicates that increasing AADT prevents the model from becoming the negative binomial crash state but increases the crash frequency in this state. The greater the AADT, the more likely the curve segment is in the zero-crash state. This may be due to the high outliers in the traffic volume data for a few curve segments.

The log-likelihood value for this zero-inflated negative binomial model is -21953.2 and the restricted log-likelihood value is -30543.0. The number of parameters is 6F. The model goodness of fit parameters indicates an ρ^2 of 0.2812, while adjusted ρ^2 value is 0.2810. Due to large sample size (i.e., 20955 curve segments), the goodness of fit is not expected to be high, and thus, 0.281 is an acceptable value for this model. Elasticities were also computed to determine the marginal effects of the independent variables in the curve crash frequency model. As this is a double log model, the elasticity was calculated using Equation 6.15:

$$\frac{\Delta Y_i}{\Delta X_i} \cdot \frac{Y_i}{X_i} = \beta_i \qquad \text{(Eq. 6.15)}$$

The elasticities for each of the independent variables are shown in Table 6.7. The interpretation of elasticities is straightforward and provides a good indication of the relative importance of variables. As an example, a 1% increase in the radius of curve causes a 0.23 percent reduction in the crash frequencies in negative binomial state. As shown in Table 6.8, the highest correlation coefficient is 0.3544 between curve radius and length. Therefore, there are no statistically significant correlations among these 4 variables used in the model (see Equation 6.14). In other words, these four variables are statistically independent and justified to be included in the model development.

TABLE 6.7
Elasticity estimates

	Radius	Length	FN at 40	AADT
Negative binomial state	-0.22	0.45	-0.46	0.62
Zero-inflated logit state	0.29	–	–	2.10

6.4.4 CMF Prediction

Figures 6.2 and 6.3 present the predicted crash frequencies over the period of 2016–2018 with respect to curve radius and pavement friction, respectively, by setting curve length and AADT as mean values. Two observations can be made through careful inspection of the curves in Figures 6.2 and 6.3. First, as friction varies from lowest to highest, the expected crash frequency decreases significantly, especially when friction (i.e., FN) is less than 25 as shown in Figure 6.2. However, the effect of friction on crash frequency varies with curve radius. The crash frequency changes slightly for curves with radii of 1,640 ft. (500 m) or larger, regardless of friction. Second, the expected frequency decreases dramatically as curve radius increases, especially when curve radii are less than 820 ft. (250 m) as shown Figure 6.3. Nevertheless, the effect of curve radius on crash frequency varies with friction. The change of crash frequency is more noticeable when friction (i.e., FN) is 50 or less, regardless of curve radius. The above observations may imply that HFST is highly effective in reducing vehicle crashes on small curves, particularly curves with a radius of 820 ft. (250 m) or less.

As for all of the 25 HFSTs installed across Indiana in 2018, the average pavement friction increased from 38.6 to 82.9. To estimate the CMF of HFST in Indiana, Equation 6.14 can be rewritten as follows:

$$CMF = \frac{N_{after}}{N_{before}} = \left(\frac{FN_{before}}{FN_{after}}\right)^{0.46} \qquad \text{(Eq. 6.16)}$$

Substituting the pavement friction values before and after installing HFST into Equation 6.16 yields a predicted CMF. For these 25 HFST sites, the predicted CMFs range between 0.519 and 0.805 with an average of 0.696 and a standard deviation of 0.092. The predicted average CMF, i.e., 0.696, is close to 0.701 for total crashes, i.e., the CMF estimated from the before-after

TABLE 6.8
Correlation coefficients of four variables

	Radius	Length	FN at 40	AADT
Radius	1	0.35439824	0.03631509	0.12254181
Length	0.35439824	1	0.02804558	-0.02752954
FNS_40	0.03631509	0.02804558	1	-0.10868255
AADT	0.12254181	-0.02752954	-0.10868255	1

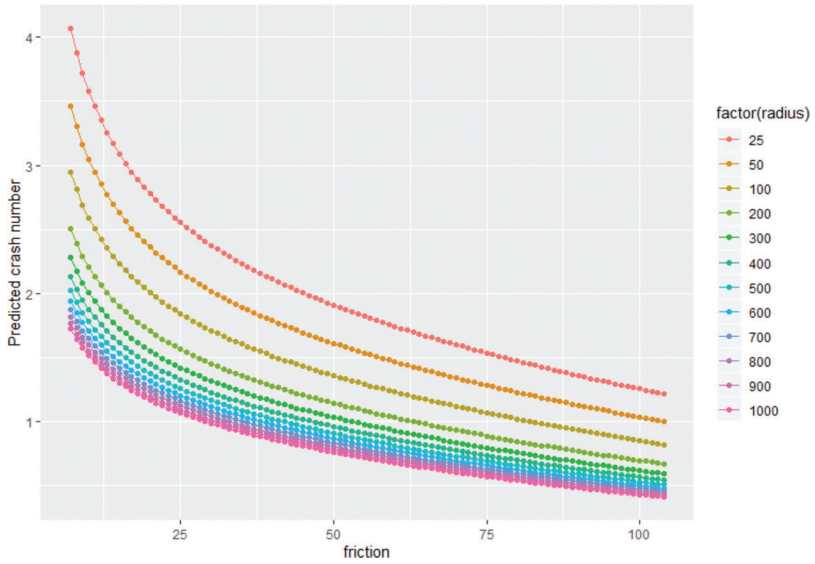

Figure 6.2 Predicted crash frequency change with friction by radius (m) (1 m = 3.28 ft.).

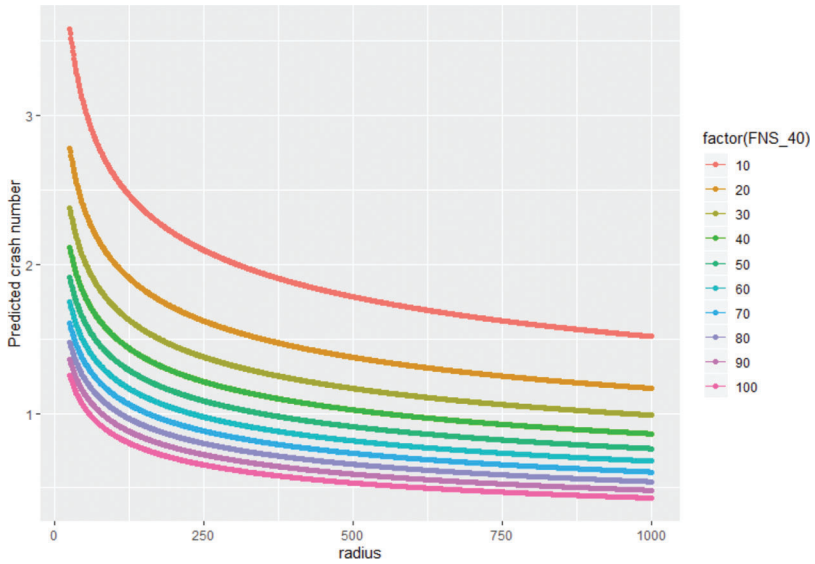

Figure 6.3 Predicted crash frequency change with radius (m) by friction (1 m = 3.28 ft.).

analysis (see Table 6.5). Evidently, the CMF predicted from Equation 6.16 agrees well with the CMF estimated from the field crash data.

7. FINDINGS AND RECOMMENDATIONS

7.1 Findings

7.1.1 Physical and Mechanical Properties

- An epoxy binder content of 15.93% is considered to be appropriate for making specimens for determining the physical and mechanical properties of the HFST epoxy-bauxite mortars.
- The laboratory test results show that the epoxy-bauxite mortar has a bulk specific gravity of 2.307, a Poisson's ratio of 0.29, and a CTE of 21.3 $\times$ 10^{-6}/°F.
- The CTE of HFST is significantly higher than those of HMA mixture and PCC, which implies that thermal incompatibilities will always arise between HFST and the underlying pavement.

7.1.2 Early Distresses

- The most common early HFST in Indiana are reflective cracking, aggregate loss, delamination at the interface between the chip seal and HMA pavement beneath HFST, and surface wrinkling (slippage). Any discontinuities in the existing pavement surface, including cracks, pothole patches, and alligator repair patches, will eventually reflect through the HFST. This may be extended to imply that there are tangible benefits to placing HFST on new pavements.

- Aggregate loss tends to occur in an HFST with surface preparation by scarification milling due to insufficient epoxy binder, installation of HFST at low temperatures, or both.
- Delamination between the existing chip seal and underlying HMA pavement tends to occur when the existing chip seal surface is pretreated by scarification milling.
- Surface wrinkling tends to occur due to the combined effect of the many factors, especially large traffic loads, low temperature application, steeper superelevation, and the strength of existing pavement.

7.1.3 Surface Preparation

- The MPD of HFST is independent of the methods for pretreating the surface of existing pavement before placing HFST. Scarification milling and shotblasting do not necessarily increase the surface MPD of HFST.
- Scarification milling produces large valleys and peaks in the treated surface, which will result in a large region of stress concentration and dramatically higher interlaminar stresses. The results of FEM analysis indicate that shotblasting tends to increase the possibilities of higher interlaminar stresses than vacuum sweeping.
- The bonding strength with scarification milling can be 18.6% less than that with shotblasting in the tire-pavement contact area. In addition, the impact of traffic loading on the bonding strength can be more severe with scarification milling than that with shotblasting.
- None of the three pretreatment methods, including power sweeping, shotblasting, and scarification milling, can outperform any of the others in terms of the mitigation of reflective cracking.

7.1.4 CMF Determination

- The CMF of HFST, i.e., 0.701, estimated from the empirical Bayes method in terms of before and after crash data is slightly less than the CMF, i.e., 0.696, derived from the crash prediction model in terms of curve geometrics, pavement friction, and AADT. The CMF from HFST sites in Indiana demonstrates good consistency with those developed by other state DOTs on both all crash reduction and wet weather crash reduction.
- The model for predicting vehicle crash on curves is a zero-inflated negative binomial model that is explanatory for horizontal curve safety performance. It can be used to evaluate the effects of pavement friction, curve radius, or both on safety performance. Most importantly, this model can be used to identify high risky curves and facilitate safety engineers to implement countermeasure efficiently.

7.2 Recommendations

Presented below are the major recommendations:

- The epoxy-bauxite mortar of HFST is a viscoelastic material at a temperature of 70°F or higher. Curing epoxy binders at low temperatures will not only increase the cost for traffic control but also the variation in the epoxy binder system, thereby affecting the durability of HFST. It is recommended to install HFST at higher end of the temperature range recommended by suppliers.
- The empirical relationship below can be utilized to estimate the binder content for fabricating epoxy-bauxite mortar specimens:

$$R = R_0 + (1.755 + 0.090MPD)$$

- The cracks in the existing pavement should be filled prior to the installation of HFST rather than by the epoxy binder spread on the existing pavement while installing HFST. Cracks reflected through the HFST should be sealed timely to slow the deterioration of cracks.
- Chip seal in good condition will not affect the durability of HFST in terms of interface bonding strength. Scarification milling does not necessarily provide better interface bonding between HFST and the underlying chip seal. It is recommended that vacuum sweeping be used as a method for preparing the surface of chip seal that is in good condition, and shotblasting be used a method for preparing the surface of new HMA pavement.
- To ensure the durability of HFST, either friction or texture testing should be performed 3 months after installation. In addition, field testing right after installation may identify potential problems when corrective actions can still be taken. The requirements for QC/QA of HFST at horizontal curves on two-lane highways can be defined in terms of surface friction, texture, or both in Table 7.1.

The above requirements are also recommended to revise INDOT's current USP for HFST.

- A CMF of 0.70 is recommended for use in estimating the safety effectiveness of HFST by INDOT. In addition, the following model can be used to identify high risk curves and facilitate safety engineers to implement countermeasure efficiently.

$$N = \frac{1}{3}\left(1 - \frac{e^{-8.83}rad^{0.29}AADT^{2.10}}{1+e^{-8.83}rad^{0.29}AADT^{2.10}}\right) e^{-0.46}rad^{-0.22}L^{0.45}FN^{-0.46}AADT^{0.62}$$

where N is the annual crash number at a specific curve; rad and L, respectively, are the radius and length of the curve, ft.; FN is the friction number at 40 miles per hour (mph); and $AADT$ is the Annual Average Daily Traffic.

TABLE 7.1
Surface friction and texture requirements for QC/QA of HFST at horizontal curves on two-lane highways

Time	Friction Number (FN)	Mean Profile Depth (MPD) (mm)
New	83	1.9
3 Months	83	1.2

REFERENCES

AASHTO. (2010). *Highway safety manual*. American Association of State Highway and Transportation Officials.

AASHTO. (2014a). *Standard practice for high friction surface treatment for asphalt and concrete pavements* (AASHTO PP79-14). American Association of State Highway and Transportation Officials.

AASHTO. (2014b). *Standard method of test for accelerated polishing of aggregates using the British wheel* (AASHTO T279-14). American Association of State Highway and Transportation Officials.

AASHTO. (2015). *Determining dynamic modulus of hot mix asphalt (HMA)* (AASHTO T342-11). American Association of State Highway and Transportation Officials.

AASHTO. (2016). *Standard method of test for bulk specific gravity (Gmb) of compacted hot mix asphalt (HMA) using saturated surface-dry specimens* (AASHTO T166-16). American Association of State Highway and Transportation Officials.

AASHTO. (2017). *Standard practice for developing dynamic modulus master curves for asphalt mixtures* (AASHTO R 62-13). American Association of State Highway and Transportation Officials.

AASHTO. (2018a). *Policy on geometric design of highways and streets*. American Association of State Highway and Transportation Officials.

AASHTO. (2018b). *Provisional standard method of test for determining the fracture potential of asphalt mixtures using semicircular bend geometry (SCB) at intermediate temperature* (AASHTO TP124-18). American Association of State Highway and Transportation Officials.

AASHTO. (2019). *Standard method of test for coefficient of thermal expansion of hydraulic cement concrete* (AASHTO T336-15). American Association of State Highway and Transportation Officials.

Al-Qadi, I. L., Ozer, H., Lambros, J., El Khatib, A., Singhvi, P., Khan, T., Rivera-Perez, J., & Doll, B. (2015). *Testing protocols to ensure performance of high asphalt binder replacement mixes using RAP and RAS* (Report No. FHWA-ICT-15-017). University of Illinois at Urbana-Champaign. http://hdl.handle.net/2142/88680

ASTM. (2013). *Standard test method for tensile strength of concrete surfaces and the bond strength or tensile strength of concrete repair and overlay materials by direct tension (pull-off method)* (ASTM C1583/C1583M-13). ASTM International.

ASTM. (2015a). *Standard specification for epoxy-resin-base bonding systems for concrete* (ASTM C881/C881M-15). ASTM International.

ASTM. (2015b). *Standard test method for compressive properties of rigid plastics* (ASTM D695-15). ASTM International.

ASTM. (2015c). *Standard practice for calculating pavement macrotexture mean profile depth* (ASTM E1845-15). ASTM International.

ASTM. (2015d). *Standard test method for skid resistance of paved surfaces using a full-scale tire* (ASTM E274/E274M-15). ASTM International.

ASTM. (2017). *Standard test method for Poisson's ratio at room temperature* (ASTM E132-17). ASTM International.

ASTM. (2018a). *Standard test methods for compressive strength of chemical-resistant mortars, grouts, monolithic surfacings, and polymer concretes* (ASTM C579-18). ASTM International.

ASTM. (2018b). *Standard test method for linear shrinkage and coefficient of thermal expansion of chemical-resistant mortars, grouts, monolithic surfacings, and polymer concretes* (ASTM C531-18). ASTM International.

ASTM. (2018c). *Standard test method for measuring surface frictional properties using the British pendulum tester* (ASTM E303-93). ASTM International.

ASTM. (2019a). *Standard test method for measuring pavement macrotexture depth using a volumetric technique* (ASTM E965-15). ASTM International.

ASTM. (2019b). *Standard test method for measuring pavement macrotexture properties using the circular track meter* (ASTM E2157-15). ASTM International.

ASTM. (2019c). *Standard test method for measuring surface frictional properties using the dynamic friction tester* (ASTM E1911-19). ASTM International.

Atkinson, J., Clark, J., & Ercisli, S. (2016, May). *High friction surface treatment curve selection and installation guide* (Report No. FHWA-SA-16-034). Federal Highway Administration.

Bíl, M., Andrášik, R., Sedoník, J., & Cícha, V. (2018). ROCA–An ArcGIS toolbox for road alignment identification and horizontal curve radii computation. *PLoS One 13*(12), e0208407. https://doi.org/10.1371/journal.pone.0208407

BSI. (2009). *Tests for mechanical and physical properties of aggregates: Determination of the polished stone value* (Standard No. BS EN 1097-8). British Standards Institution.

de León Izeppi, E., Flintsch, G. W., & McGee, K. K. (2010, June). *Field performance of high friction surfaces* (Report No. FHWA/VTRC 10-CR6). Virginia Tech Transportation Institute Center for Sustainable Transportation Infrastructure. http://www.virginiadot.org/vtrc/main/online_reports/pdf/10-cr6.pdf

de León Izeppi, E., Flintsch, G. W., Katicha, S. W., McCarthy, R., & Smith, K. (2019). *Indiana DOT data collection and analysis* (FHWA Pavement Friction Management [PFM] Support Program). VTRC and Applied Pavement Technology, Inc.

Dellinger, T. H., & Poursee, A. (2016). *Characterization of Portland cement concrete coefficient of thermal expansion in South Carolina* (Report No. FHWA-SC-17-03). Clemson University Glenn Department of Civil Engineering. https://www.scdot.scltap.org/wp-content/uploads/2017/06/SPR-722-Final-Report-PCC-Coefficient.pdf

Elvik, R. (2013). International transferability of accident modification functions for horizontal curves. *Accident Analysis & Prevention*, *59*, 487–496. https://doi.org/10.1016/j.aap.2013.07.010

Ferry, J. D. (1980, September). *Viscoelastic properties of polymers* (3rd ed.). John Wiley & Sons.

FHWA. (n.d.). *Crash modification factors clearinghouse* [Webpage]. Federal Highway Administration. Retrieved April 20, 2018, from https//www.cmfclearinghouse.org/results.cfm

Garcia, V., Miramontes, A., Garibay, J., Abdallah, I., & Nazarian, S. (2017, June). *Improved overlay tester for fatigue cracking resistance of asphalt mixtures* (Report No. TxDOT 0-6815-1). The University of Texas at El Paso Center for Transportation Infrastructure Systems. https://library.ctr.utexas.edu/hostedpdfs/utep/0-6815-1.pdf

Gillespie, T. D. (1992, February 1). *Fundamentals of vehicle dynamics*. Society of Automotive Engineers (SAE), Inc.

Gross, F., Persaud, B., & Lyon, C. (2010, December). A guide to developing quality crash modification factors (Report No. FHWA-SA-10-032). Federal Highway Administration. https://www.cmfclearinghouse.org/collateral/cmf_guide.pdf

Hauer, E. (1997). *Observational before–after studies in road safety: Estimating the effect of highway and traffic engineering measures on road safety*. Elsevier Science Ltd.

Henry, J. J. (2000). *Evaluation of pavement friction characteristics* (NCHRP Synthesis 291). National Cooperative Highway Research Program (NCHRP), Transportation Research Board. https://onlinepubs.trb.org/onlinepubs/nchrp/nchrp_syn_291.pdf

ICJI. (2017). *State of Indiana FY 2017 traffic safety annual report*. Indiana Criminal Justice Institute. https://www.in.gov/cji/trafficsafety/files/Highway_Safety_Annual_Report_2017.pdf

Imprialou, M., & Quddus, M. (2019). Crash data quality for road safety research: Current state and future directions. *Accident Analysis & Prevention*, 130, 84–90. https://doi.org/10.1016/j.aap.2017.02.022

INDOT. (2019). *2018 Standard specifications*. Indiana Department of Transportation. https://www.in.gov/dot/div/contracts/standards/book/sep17/sep.htm

Islam, M. R., & Tarefder, R. A. (2014). Determining thermal properties of asphalt concrete using field data and laboratory testing. *Construction and Building Materials*, *679* (Part B), 297–306. https://doi.org/10.1016/j.conbuildmat.2014.03.040

Jurewicz, C., & Pyta, V. (2010). Effect of clear zone widths on run-off-road crash outcomes. In J. Motha (Ed.), *Proceedings of the 2010 Australasian Road Safety Research, Policing and Education Conference* (pp. 1–12.).

Kemphues, R. F. (1972, April). *Coefficient of linear thermal expansion of epoxy resin mortars* (Technical Report M-14). Construction Engineering Research Laboratory.

Kleppner, D., & Kolenkow, R. (1973). *An introduction to mechanics*. McGraw-Hill, Inc.

Lee, J., & Mannering, F. (2002, March). Impact of roadside features on the frequency and severity of run-off-roadway accidents: An empirical analysis. *Accident Analysis & Prevention*, *34*(2), 149–161. https://doi.org/10.1016/s0001-4575(01)00009-4.

Li, S., Cong, P., Yu, D., Xiong, R., & Jiang, Y. (2019). Laboratory and field evaluation of single layer and double layer high friction surface treatments. *Transportation Research Record*, *2673*(2), 552–561. https://doi.org/10.1177/0361198119826078

Li, S., Harris, D., & Wells, T. (2016, October). Surface texture and friction characteristics of diamond-ground concrete and asphalt pavements. *Journal of Traffic and Transportation Engineering* (English Edition), *3*(5), 475–482.

Li, S., Noureldin, S., & Zhu, K. (2007). Realistic approach for enhancing reliability of pavement surface friction testing. In B. Choubane (Ed.), *Pavement Surface Condition/Performance Assessment*: *Reliability and Relevancy of Procedures and Technologies* (pp. 73–80). ASTM International. https://doi.org/10.1520/STP45252S

Li, S., Xiong, R., Yu, D., Zhao, G., Cong, P., & Jiang, Y. (2017). *Friction surface treatment selection: Aggregate properties, surface characteristics, alternative treatments, and safety effects* (Joint Transportation Research Program Publication No. FHWA/IN/JTRP-2017/09). West Lafayette, IN: Purdue University. https://doi.org/10.5703/1288284316509

Li, S., Zhu, K., Noureldin, S., & Harris, D. (2005). Identifying friction variations with the standard smooth tire for network pavement inventory friction testing. *Transportation Research Record*, *1905*(1), 157–165. https://doi.org/10.1177/0361198105190500117

Lord, D., Washington, S. P., & Ivan, J. N. (2005). Poisson, Poisson-gamma and zero-inflated regression models of motor vehicle crashes: Balancing statistical fit and theory. *Accident Analysis & Prevention*, *37*(1), 35–46. https://doi.org/10.1016/j.aap.2004.02.004

Lord, D., Washington, S., & Ivan, J. N. (2007). Further notes on the application of zero-inflated models in highway safety. *Accident Analysis & Prevention*, *39*(1), 53–57. https://doi.org/10.1016/j.aap.2006.06.004

Lyon, C., Persaud, B., Merritt, D., & Cheung, J. (2020). Empirical Bayes before-after study to develop crash modification factors and functions for high friction surface treatments on curves and ramps. *Transportation Research Record*. https://doi.org/10.1177/0361198120957327

Merritt, D. K., Lyon, C. A., & Persaud, B. N. (2015, February). *Evaluation of pavement safety performance* (Publication No. FHWA-HRT-14-065). The Transtec Group, Inc. https://www.fhwa.dot.gov/publications/research/safety/14065/14065.pdf

Miaou, S. P. (1993, July). *The relationship between truck accidents and geometric design of road sections: Poisson versus negative binomial regressions* (Report No. CONF-940128-2). Oak Ridge National Laboratory.

Permanent International Association of Road Congress. (1987). *Optimization of pavement surface characteristics* [Paper presentation]. XVIII World Road Congress, Brussels, Belgium.

Persaud, B., Retting, R. A., & Lyon, C. (2000). Guidelines for identification of hazardous highway curves. *Transportation Research Record*, *1717*(1), 14–18. https://doi.org/10.3141/1717-03

Srinivasan, R., Carter, D., & Bauer, K. (2013, September). *Safety performance function decision guide: SPF calibration versus SPF development* (Report No. FHWA-SA-14-004). Federal Highway Administration. https://safety.fhwa.dot.gov/rsdp/downloads/spf_decision_guide_final.pdf

Tozzo, C., D'Andrea, A., Cozzani, D., & Meo, A. (2014). Fatigue investigation of the interface shear performance in asphalt pavement. Modern Applied Science, 8(2), 1–11.

TxDOT. (2008). *Test procedure for overlay test* (TxDOT Designation Tex-248-F). Texas Department of Transportation. https://ftp.dot.state.tx.us/pub/txdot-info/cst/TMS/200-F_series/archives/248-0307.pdf

Vuong, Q. H. (1989, March). Likelihood ratio tests for model selection and non-nested hypotheses. *Econometrica: Journal of the Econometric Society*, *57*(2) 307–333.

Waters, J. (2011). High friction surfacing failure mechanisms [Conference presentation]. *3rd International Surface Friction Conference, Safer Road Surfaces-Saving Lives*. Gold Coast, Australia. https://saferroadsconference.com/wp-content/uploads/2016/05/Waters-High-Friction-Surfacing-Failure-Mechanisms.pdf

Wei, F., Xing, M., Li, S., Shan, J., & Guan, B. (2020). Physical and mechanical properties of epoxy–bauxite mortar of high-friction surface treatment. *Journal of Materials in Civil Engineering*, *32*(6), 04020146.

Wilson, B. T., & Mukhopadhyay, A. (2016). *Alternative aggregates and materials for high friction surface treatments* (Report No. BDR74-977-05). Texas A&M Transportation Institute.

Yu, D., Xiong, R., Li, S., Cong, P., Shah, A., & Jiang, Y. (2019). Laboratory evaluation of critical properties and attributes of calcined bauxite and steel slag aggregates for pavement friction surfacing. *Journal of Materials in Civil Engineering*, *31*(8), 04019155. https://doi.org/10.1061/(ASCE)MT.1943-5533.0002806

Zhao, G., Li, S., Jiang, Y., & Lee, J. (2018). *Quality assurance procedures for chip seal operations using macrotexture metrics* (Joint Transportation Research Program Publication No. FHWA/IN/JTRP-2018/12). West Lafayette, IN: Purdue University. https://doi.org/10.5703/1288284316779

APPENDICES

Appendix A. Enhanced Texture Measurements Using Image Processing

Appendix B. Mean Profile Depth Measurements at All HFST Sites

APPENDIX A. ENHANCED TEXTURE MEASUREMENTS USING IMAGE PROCESSING

A.1 Equipment and Data Collection

A.1.1 Equipment

Both a laser texture scanner (LTS) (AMES Engineering, 2019) and a smartphone were used for data collection. Presented in Figure A.1 are the photos of an LTS 9400 and an iPhone 8 plus used in texture testing. The LTS was last calibrated in 2018. It can calculate the texture profile's mean profile depth (MPD), texture profile index (TPI), estimated texture depth (ETD), and root mean square (RMS) of height deviation. During testing, the LTS was configurated to scan ten 100 mm (4″) long profiles evenly spaced over a scan area of 107.95 mm × 72.01 mm (4.25″ × 2.835″). The average point spacing within each profile was 0.014286 mm. The MPD for each profile was calculated and the arithmetic mean of the ten MPDs was considered as the MPD over the scan area. In this study, the LTS was mainly used for measuring the MPD for a pavement surface and utilized as a reference method compared to the proposed image-based method.

(a) (b) (c)

Figure A.1 Texture test equipment: (a) LTS 9400, (b) iPhone 8 plus, and (c) control frame.

The pavement images were collected with a commonly used smartphone, the iPhone 8 Plus (see Figure A.1(b)) which has two 12 MP rear cameras: (1) a wide-angle camera with an f/1.8 aperture; and (2) a telephoto camera with an f/2.8 aperture. The telephoto camera is designed to create a depth-of-field effect, which composes a photo that keeps the subject sharp with a blurred background. In this study, only the first camera (i.e., wide-angle camera) was deployed. The dimension of each image was 4,032 pixels × 3,024 pixels. After the images were collected, a three-dimensional (3D) point cloud of the pavement surface was reconstructed using Agisoft Metashape (Agisoft, 2019), a stand-alone software program that performs photogrammetric processing of digital images and generates 3D spatial data in multiple applications.

To provide control and reference for measurement, a control frame (see Figure A.1(c)) was placed in the scene when collecting images. The control frame was used as a reference for 3D reconstruction when collecting the pavement surface images and analyzing MPD at the Indiana Department of Transportation (INDOT) friction test track and HFST sites as shown in Figure A.2. The control frame template is made of plastically laminated hard paper with an central rectangular area of 152 mm × 90 mm (6″ × 3.54″). There are many marking points on the surface of the template, which are used as references. Moreover, four targets denoted as A1, A2, A3, and A4 with different heights are glued on the template, which are used as the height ruler. The heights of these four targets and the distances between them are measured by a vernier caliper to a precision of 0.01 mm. The dimensions of the rectangular area enclosed by these four targets are the same as

the scan area of the LTS to assure that the observation area is consistent for both the LTS and the smartphone.

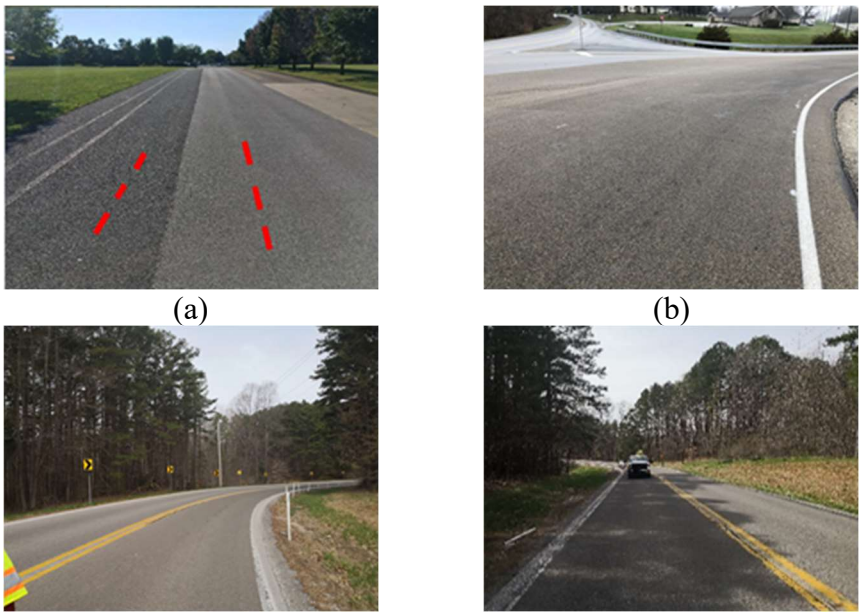

(a) (b) (c) (d)

Figure A.2 Test sites: (a) INDOT friction track, (b) SR-32, (c) SR-446, and (d) SR-205.

A.1.2 Data Collection

The data collection procedure for MPD analysis of the proposed method includes following steps:

1. Choose a spot randomly and mark the position at the pavement surface.
2. Apply the control frame to the spot along the road direction and apply the LTS on top of control frame, making sure that the laser scans are along the road direction, while scanning the spot and calculating the MPD.
3. Remove the LTS leaving the control frame on road, take between 20~32 images for the spot using a smartphone following a circle trace, which is about 400 mm high to the area center and the diameter is about 600 mm.
4. Move to the next spot and repeat steps (1) to (3) until all spots completed.

A.2 Test Sites

A.2.1 INDOT Friction Test Track

The INDOT friction test track is located at the INDOT Research Division, West Lafayette, Indiana (see in Figure A.2). There are three different types of pavements, including a 3-year old HMA pavement, a 10-year old HMA pavement with surface raveling, and a concrete pavement with smooth surface. In addition, a 3.28′ × 3.28′ (1 m × 1 m) of double-layer HFST was installed over the 10-year old HMA pavement. The measurements were made on the 3-year old HMA, 10-year old HMA, and HFST surfaces, respectively, on December 3, 2018. Both the 3- and 10-year old HMA surfaces were constructed with 9.5 mm HMA mixes of the same mxi design. For each surface, two test spots were selected for making the MPD measurements with both the LTS and image test methods. Table A.1 summarizes the test spots and the corresponding test runs at the INDOT friction test track.

Table A.1 Summary of data collected at the INDOT friction test track

		LTS	Image Method	
Type of Pavement	**Test Date**	**No. of Spots**	**No. of Spots**	**No. Images for Each Spot**
3-year old HMA	12/3/2018	2	2	22, 29
10-year old HMA	12/3/2018	2	2	27
HFST	12/3/2018	2	2	24, 25

A.2.2 Actual HFST Sites

Both texture and image measurements were further made over three actual HFSTs on SR-32, SR-446, and SR-205 (see Figure A.2), respectively, using the LTS and the iPhone 8 plus. The HFST on SR-32 was completed on August 13, 2018. Before installing the HFST, MPDs were made over the newly placed 1.5″ 9.5 mm HMA mill and fill. About 8 months after construction on April 5, 2019, MPDs were made over the HFST and a total of 64 images were collected at 3 spots. The HFST on SR-446 was placed on October 19, 2018. The existing pavement surface was single-layer chip seal. MPDs were made over the HFST right after construction with the LTS. About six months after construction on April 11, 2019, MPDs were measured at seven spots and a total of 290 images were collected at ten spots, including the same seven spots for the LTS tests and another three spots to collected images alone.

The HFST construction at SR-205 was finished on October 23, 2018. The existing pavement surface was also single-layer chip seal. On the day of construction, MPDs were measured over the HFST before opening to traffic. Six months after treatment on April 16, 2019, both MPDs and a total of 306 images were collected at 12 spots. Summarized in Table A.2 is the information on the LTS tests and image collections at all these three sites.

Table A.2 Summary of data collected at HFTS sites on actual roads

	Day of Construction		After Construction			
	LTS		LTS	Image Method		
HFST Site	No. of Spots	Date	No. of Spots	No. of Spots	No. of Images for Each Spot	Date
SR-32	11	8/13/2018	3	3	20–22	4/5/2019
R-446	10	10/17/2018	7	10	20–32	4/11/2019
SR-205	11	10/22/2018	12	12	22–29	4/16/2019

A.3 Methodology

A.3.1 Structure from Motion

Although the implementation steps of Structure from Motion (SfM) vary depending on the software packages used, from image acquisition to georeferenced dense point cloud, the method commonly consists of the following three major steps.

The first step in SfM implementation is to detect, describe, and match the corresponding keypoints between different image-frames. For this purpose, the Scale-Invariant Feature Transform (SIFT) algorithm (Lowe, 1999, 2004) was used. All the algorithms above consist of two parts, i.e., keypoint detection and keypoint description. The detector is used to detect the keypoints on the images. The descriptor is utilized for describing the keypoints and matching these

keypoints by calculating the distance between two points on different images. Figure A.3(a) illustrates the keypoint matching for two images.

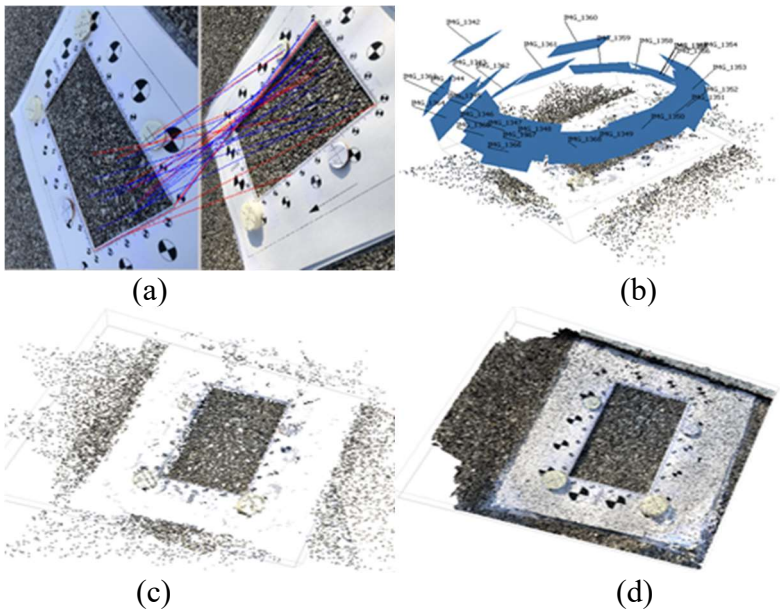

(a) (b)

(c) (d)

Figure A.3 Results from SfM: (a) keypoint matching between two images, (b) output of bundle adjustment, (c) sparse point cloud, and (d) dense point cloud.

In the second step, the SfM method takes advantage of the redundancy provided by the large number of images and keypoints to estimate the exterior orientation, interior orientation, and distortion parameters, as shown in Figure A.3(b).

In the last step, the point density is increased by implementing multi-view photogrammetry algorithms. Figures A.3(c) and A.3(d) illustrate the dense point cloud generated from the sparse point cloud. The purpose of the algorithms is to reconstruct the 3D point cloud of an object using overlapped images collected from different viewpoints and known camera positions (Seitz et al., 2006).

A.3.2 Mean Profile Depth

According to ASTM E1845-15 (ASTM, 2015), MPD is the average of all the mean segment depths (MSDs) for all the segments of a measured texture profile. Each profile shall be divided into segments of $100 \pm 2\ mm$ for analysis in the subsequent steps and each segment shall be further divided into two equal lengths of $50\ mm$ and the maximum value is determined for each subsegments. Then these two values are averaged arithmetically to obtain the MSD. The MSD is the average value of peak level (1st) and peak level (2nd) having a given baseline (segment), as shown in Figure A.4 and Equation A.1.

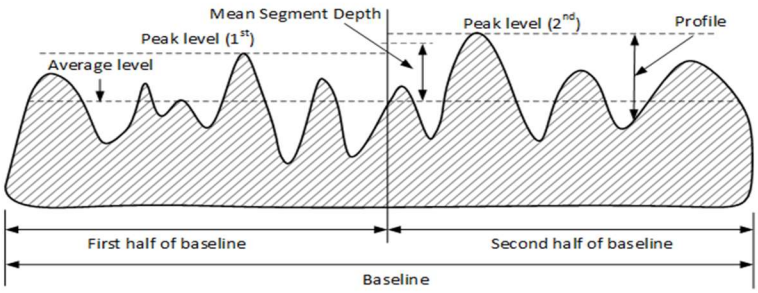

Figure A.4 Procedure of MSD computation (ASTM, 2015).

$$MSD = \frac{1}{2}[Peak\ level\ (1^{st}) + Peak\ level\ (2^{nd})] \quad \text{(Eq. A.1)}$$

A.4 Results and Evaluation

A.4.1 MPD Results for INDOT Friction Test Track

The MPD results over the INDOT friction test track are listed in Table A.3. Accordingly, the MPD of HFST is improved by 200% compared to the 3-year old pavement and by 50% with respect to the 10-year old pavement. Therefore, applying HFST on the existing old road is an effective to increase the pavement friction. It is shown that in Table A.3, the MPDs measured by LTS range from 0.515 mm to 2.073 mm, and the MPDs by images range from 0.559 mm to 2.030 mm. The difference between the average MPDs for the two methods is less than 6%, depending on the type of pavement. It can be seen that the proposed image-based method has the capability of acquiring comparable MPD results as the LTS.

Table A.3 MPD from LTS and images for the INDOT friction test track

Type of Pavement		**3-Year Old HMA**			**10-Year Old HMA**			**HFST**		
Spot ID		**1**	**2**		**3**	**4**		**5**	**6**	
	No. of Images	**27**	**27**	**Ave.**	**22**	**29**	**Ave.**	**25**	**24**	**Ave.**
Image	MPD (mm)	0.559	0.639	0.599	1.244	1.388	1.316	2.030	1.864	1.947
LTS	MPD (mm)	0.515	0.733	0.624	1.275	1.323	1.299	1.749	2.073	1.911
Difference of MPD (%)		8.6	-12.9	-2.15	-2.40	4.9	1.250	16.0	-10.1	2.95

A.4.2 MPD Results for Actual HFST Sites

Summarized in Table A.4 are the MPD measurements by both the LTS and image methods, respectively, at the three actual HFST sites mentioned previously. A total of 11 MPDs were measured using the LTS on SR-32 right after construction and the average MPD was 2.075 mm. After about 7.7 months, three MPDs were measured using the LTS and the average MPD was 1.315 mm, indicating a 36.63% reduction since construction. Meanwhile, a total of 64 images were taken as well at the same three spots for the LTS tests. The average MPD calculated by the proposed image-based method was 1.393 mm, approximately 5.9% (i.e., 0.078 mm) larger than the average MPD by LTS.

Table A.4 Summary of MPD measurements at three actual HFST sites

	Day of Construction			After Construction				
	LTS			LTS		Image		
FHST Site	No. of Spots	MPD (mm)	Months After	No. of Spots	MPD (mm)	No. of Spots	MPD (mm)	Difference of MPD (%)
SR-32	11	2.075	7.7	3	1.315	3	1.393	5.9
SR-446	10	1.590	5.8	7	1.259	10	1.302	3.4
SR-205	11	1.860	5.8	12	1.243	12	1.235	-0.4

As for the HFST site on SR-446, ten MPD measurements were made by LTS on the day of construction and the average MPD was 1.590 mm. After 5.8 months of installing the HFST, seven MPD measurements were made by LTS at 7 locations. The average MPD was 1.259 mm, indicating a 20.82% reduction since construction. Meanwhile a total of 290 images were shot at 10 locations including these seven locations for the LTS tests. The average MPD calculated by our proposed image-based method was 1.302 mm which was only 3.4%, 0.043 mm, larger than average MPD with the LTS. For the HFST site on SR-205, eleven MPD measurements were made using the LTS on the day of construction and the average MPD was 1.860 mm. After 5.8 months, twelve MPD measurements were made using the LTS at 12 spots. The average MPD was 1.243 mm, representing a 33.17% reduction. In addition, a total of 306 images were taken at these 12 spots and the average MPD calculated from the proposed image-based method was 1.235 mm, which was only 0.4%, 0.008 mm, less than average MPD by LTS.

Evidently, the proposed image-based method shows good performance in determining MPD at both the INDOT friction test track and the HFST sites on actual roads. The differences of the average MPDs between the proposed image-based and the LTS methods are less than 6%. Moreover, the differences of the average MPD between the two methods decreased from 5.9% to -0.4% as the number of spots increased from 3 to 12. It can be inferred that as the number of spots increases, the difference of average MPDs between two methods decreases and the MPD results from the proposed image-based method would be more consistent with the MPD from the LTS test method.

A.5 Conclusions

A novel approach for MPD measurements using multi-view images collected by smartphones at a typical resolution of 12 MP is presented. In comparison to reported camera systems for pavement macrotexture measurement, it is simple to operate and is cost-effective and productive.

The proposed approach was conducted and verified by comparing the MPD results calculated from the proposed method and those measured using LTS. Thirty-one 3D point clouds were reconstructed from 790 images collected in situ at 31 different spots (152 mm × 90 mm) and utilized to calculate MPDs. Smartphone images with a home-made control frame are sufficient for the reconstruction of a high-resolution 3D point cloud. According to the comparisons between the MPD measurements made by LTS and calculated based on the high-resolution 3D point clouds, their average difference is 2.9% and the maximum difference is less than 6%.

Field experiments conducted with the proposed method supported that smartphone images, whose resolution are much coarser than images captured by a professional camera, can be used satisfactorily to measure pavement macrotexture. The results are consistent with measurements made using LTS. The reliability of the proposed method can be assured by choosing no less than

7 spots and taking at least 30 images for each spot. This newly development shows the potentials to be further enhanced and adopted by the pavement community.

The 3D reconstruction and MPD calculation were processed on computer and it took hours to accomplish the fine-resolution point cloud reconstruction. The major problem for a smartphone is its incapability of 3D pavement surface reconstruction. More work is needed to investigate a faster 3D pavement surface reconstruction method so that it can be achieved to accomplish the entire MPD measurement procedure on the smartphone. In this way, the efficiency of pavement texture measurement can be further improved to meet the needs of routine operation.

References for Appendix A

Agisoft. (2019). *Metashape user manual: Standard edition, version 1.5*. Agisoft LLC. https://www.agisoft.com/pdf/metashape_1_5_en.pdf

AMES Engineering. (2019). *Laser texture scanner 9400/9400HD* [Webpage]. AMES Engineering.

ASTM. (2015). *Standard practice for calculating pavement macrotexture mean profile depth* (ASTM E1845-09). ASTM International.

Lowe, D. G. (1999). Object recognition from local scale-invariant features. *Proceedings of the Seventh IEEE International Conference on Computer Vision*. IEEE. https://doi.org/10.1109/iccv.1999.790410

Lowe, D. G. (2004). Distinctive image features from scale-invariant keypoints. *International Journal of Computer Vision*, *60*(2), 91–110. https://doi.org/10.1023/b:visi.0000029664.99615.94

Seitz, S. M., Curless, B., Diebel, J., Scharstein, D., & Szeliski, R. (2006). A comparison and evaluation of multi-view stereo reconstruction algorithms. *2006 IEEE Computer Society Conference on Computer Vision and Pattern Recognition–Volume 1 (CVPR06)*. https://doi.org/10.1109/cvpr.2006.19

APPENDIX B. MEAN PROFILE DEPTH MEASUREMENTS AT ALL HFST SITES

Table B.1 Mean profile depth (MPD) measurements (mm) within 3 months

	New			1-2 Weeks					1-3 Months				
		LWT[1]/RWT[2]			LWT		RWT			LWT		RWT	
Road	**Age**	**Mean**	**SD[3]**	**Age**	**Mean**	**SD**	**Mean**	**SD**	**Age**	**Mean**	**SD**	**Mean**	**SD**
SR-32	0	2.044	0.101	–	–	–	–	–	30	1.516	0.275	1.441	0.269
	–	–	–	–	–	–	–	–	100	1.341	0.367	1.315	0.233
SR-25	–	–	–	14	1.278	0.237	1.321	0.254	–	–	–	–	–
	–	–	–	14	1.255	0.218	1.339	0.247	–	–	–	–	–
SR-205a	0	1.841	0.076	15	1.182	0.238	1.255	0.231	–	–	–	–	–
	–	–	–	15	1.252	0.241	1.288	0.223	–	–	–	–	–
	–	–	–	15	1.237	0.262	1.358	0.256	–	–	–	–	–
US-35a	0	1.897	0.114	–	–	–	–	–	33	1.368	0.266	1.328	0.243
	–	–	–	–	–	–	–	–	33	1.454	0.256	1.445	0.254
	–	–	–	–	–	–	–	–	33	1.426	0.256	1.268	0.219
	–	–	–	–	–	–	–	–	33	1.451	0.252	1.356	0.239
US-35b	–	–	–	–	–	–	–	–	29	1.493	0.268	1.469	0.277
	–	–	–	–	–	–	–	–	29	1.524	0.273	1.498	0.273
	–	–	–	–	–	–	–	–	29	1.537	0.270	1.437	0.255
	–	–	–	–	–	–	–	–	29	1.529	0.260	1.446	0.256
US-24a	–	–	–	10	1.342	0.247	1.433	0.260	–	–	–	–	–
	–	–	–	10	1.269	0.221	1.370	0.231	–	–	–	–	–
US-24b	–	–	–	10	1.350	0.226	1.375	0.233	–	–	–	–	–
	–	–	–	10	1.189	0.222	1.303	0.236	–	–	–	–	–
SR-23	–	–	–	13	1.111	0.201	1.087	0.190	–	–	–	–	–
	–	–	–	13	1.149	0.206	1.194	0.221	–	–	–	–	–
SR-14	0	1.928	0.117	7	1.173	0.202	1.192	0.223	–	–	–	–	–
	–	–	–	7	1.310	0.215	1.289	0.226	–	–	–	–	–
SR-43	–	–	–	–	–	–	–	–	55	1.199	0.235	1.250	0.248
	–	–	–	–	–	–	–	–	55	1.343	0.247	1.362	0.329
SR-446	0	1.732	0.129	–	–	–	–	–	54	1.162	0.262	1.257	0.231
	–	–	–	–	–	–	–	–	54	1.137	0.254	1.260	0.264
SR-450	0	1.989	0.143	–	–	–	–	–	56	1.244	0.243	1.248	0.315
	–	–	–	–	–	–	–	–	56	1.248	0.250	1.195	0.334

[1] LWT = left wheel track
[2] RWT = right wheel track
[3] SD = standard deviation

Table B.2 Mean profile depth (MPD) measurements (mm) in 6, 12, and 18 months

	6 Months					12 Months					18 Months				
		LWT[1]		RWT[2]			LWT		RWT			LWT		RWT	
Road	Age	Mean	SD[3]	Mean	SD	Age	Mean	SD	Mean	SD	Age	Mean	SD	Mean	SD
SR-32	245	1.139	0.209	1.163	0.226	388	1.152	0.208	–	–	618	1.074	0.204	1.115	0.231
SR-25	208	1.058	0.183	1.091	0.191	364	1.078	0.190	1.087	0.196	567	1.012	0.189	1.015	0.196
	208	1.053	0.185	1.180	0.216	364	1.087	0.188	1.136	0.206	567	1.053	0.186	1.105	0.239
SR-205a	209	1.060	0.190	1.078	0.283	365	1.111	0.204	1.111	0.217	568	1.029	0.209	1.075	0.252
	209	1.063	0.200	1.108	0.217	365	1.094	0.191	1.121	0.183	–	–	–	–	–
SR-205b	209	1.105	0.204	1.122	0.208	365	1.094	0.214	1.103	0.218	568	1.001	0.195	1.078	0.248
	209	1.168	0.225	1.171	0.220	–	–	–	–	–	568	1.027	0.234	1.060	0.204
US-35a	–	–	–	–	–	356	1.053	0.168	–	–	620	1.125	0.192	0.954	0.163
	–	–	–	–	–	–	–	–	–	–	620	1.184	0.205	1.046	0.201
US-35b	–	–	–	–	–	352	1.203	0.206	–	–	616	1.260	0.251	1.117	0.214
	–	–	–	–	–	352	1.204	0.206	–	–	616	1.253	0.220	1.121	0.198
US-24a	175	1.139	0.202	1.164	0.225	359	1.136	0.211	1.120	0.196	560	1.061	0.194	1.065	0.215
	175	1.094	0.189	1.229	0.227	359	–	–	–	–	560	1.035	0.178	1.111	0.203
US-24b	175	1.208	0.199	1.216	0.217	359	1.198	0.205	1.207	0.210	560	1.136	0.222	1.120	0.199
	175	1.132	0.193	1.180	0.211	359	1.137	0.190	1.169	0.201	560	1.086	0.192	1.127	0.196
SR-23	181	1.046	0.230	1.037	0.197	362	1.137	0.249	1.038	0.216	563	1.021	0.256	1.008	0.250
	181	1.027	0.197	1.107	0.217	362	1.040	0.196	1.105	0.203	563	0.974	0.187	1.046	0.209
SR-14	182	1.045	0.183	1.139	0.229	364	1.029	0.189	1.132	0.240	565	0.991	0.179	1.089	0.236
	182	1.141	0.201	1.180	0.216	364	1.177	0.193	1.193	0.212	565	1.143	0.192	1.131	0.204
SR-43	194	1.116	0.205	1.138	0.235	371	1.106	0.305	1.152	0.216	567	1.070	0.180	1.085	0.191
	194	1.196	0.238	1.254	0.228	371	1.251	0.264	1.235	0.338	567	1.201	0.204	1.231	0.205
SR-446	193	1.156	0.215	1.187	0.206	370	1.154	0.202	1.193	0.202	566	1.108	0.192	1.177	0.207
	193	1.129	0.185	1.200	0.221	–	–	–	–	–	566	1.099	0.190	1.147	0.207
SR-65	218	1.344	0.232	1.411	0.401	360	1.367	0.229	–	–	568	1.313	0.252	1.327	0.227
	218	1.254	0.210	1.270	0.209	360	1.224	0.207	–	–	568	1.226	0.215	1.211	0.205
SR-450	195	1.188	0.226	1.231	0.221	350	1.158	0.452	–	–	559	1.146	0.212	1.212	0.239
	195	1.232	0.255	1.193	0.260	350	1.100	0.361	–	–	559	1.176	0.240	1.216	0.241
SR-56	217	1.430	0.243	1.412	0.309	359	1.158	0.452	–	–	566	1.359	0.244	1.391	0.255
	–	–	–	–	–	359	1.100	0.361	–	–	566	1.386	0.276	1.385	0.264
SR-257	213	1.224	0.211	1.293	0.224	355	1.255	0.211	–	–	562	1.201	0.214	1.240	0.216
	213	1.250	0.235	1.284	0.251	355	1.285	0.248	–	–	562	1.229	0.234	1.268	0.224
SR-237	262	1.322	0.257	1.343	0.285	355	1.248	0.411	–	–	564	1.335	0.229	1.362	0.237
	262	1.333	0.256	1.371	0.271	355	1.223	0.350	–	–	564	1.340	0.226	1.374	0.238
SR-62a	224	1.217	0.221	1.324	0.243	365	1.203	0.215	1.319	0.245	574	1.194	0.230	1.294	0.240
	224	1.400	0.252	1.389	0.233	365	1.416	0.251	1.338	0.228	574	1.393	0.261	1.347	0.227
SR-62b	223	1.309	0.226	1.307	0.420	364	1.271	0.232	1.292	0.245	573	1.315	0.265	1.290	0.238
	223	1.307	0.246	1.415	0.266	364	1.231	0.226	1.343	0.288	573	1.221	0.238	1.318	0.242
SR-62c	219	1.278	0.226	1.410	0.255	360	1.352	0.233	1.321	0.228	569	1.317	0.253	1.308	0.240
	219	1.413	0.245	1.437	0.245	360	1.212	0.226	1.345	0.239	569	1.253	0.230	1.286	0.226
SR-62d	220	1.421	0.369	1.390	0.236	361	1.237	0.218	1.369	0.243	570	1.228	0.251	1.362	0.256
	220	1.235	0.202	1.315	0.225	361	1.352	0.274	1.364	0.247	570	1.331	0.267	1.335	0.229

[1] LWT = left wheel track
[2] RWT = right wheel track
[3] SD = standard deviation

About the Joint Transportation Research Program (JTRP)

On March 11, 1937, the Indiana Legislature passed an act which authorized the Indiana State Highway Commission to cooperate with and assist Purdue University in developing the best methods of improving and maintaining the highways of the state and the respective counties thereof. That collaborative effort was called the Joint Highway Research Project (JHRP). In 1997 the collaborative venture was renamed as the Joint Transportation Research Program (JTRP) to reflect the state and national efforts to integrate the management and operation of various transportation modes.

The first studies of JHRP were concerned with Test Road No. 1—evaluation of the weathering characteristics of stabilized materials. After World War II, the JHRP program grew substantially and was regularly producing technical reports. Over 1,600 technical reports are now available, published as part of the JHRP and subsequently JTRP collaborative venture between Purdue University and what is now the Indiana Department of Transportation.

Free online access to all reports is provided through a unique collaboration between JTRP and Purdue Libraries. These are available at http://docs.lib.purdue.edu/jtrp.

Further information about JTRP and its current research program is available at http://www.purdue.edu/jtrp.

About This Report

An open access version of this publication is available online. See the URL in the citation below.

Wei, F., Wang, C., Tian, X., Li, S., & Shan, J. (2021). *Investigation of durability and performance of high friction surface treatment* (Joint Transportation Research Program Publication No. FHWA/IN/JTRP-2021/02). West Lafayette, IN: Purdue University. https://doi.org/10.5703/1288284317281